Molecular and Biophysiological Differences in Neuronal Innexin Gap Junctions Likely Underlie Unique Circuit Behaviors in *Hydra vulgaris*

Joshua J. Swore

A dissertation

submitted in partial fulfillment of the

requirements for the degree of

Doctor of Philosophy

University of Washington

2022

Reading Committee:

Martha Bosma, Chair

Adrienne Fairhall

David Perkel

Program Authorized to Offer Degree:

Biology

University of Washington

Abstract

Molecular and Biophysiological Differences in Neuronal Innexin Gap Junctions Likely Underlie Unique Circuit Behaviors in *Hydra vulgaris*

Joshua J. Swore

Chair of the Supervisory Committee:

Martha Bosma

Department of Biology

Connexins, in vertebrates, and Innexins, in invertebrates, are non-homologous gene families that are both known to form functionally similar channels. Connexins have been well characterized both functionally and molecularly but there is still a large gap of characterization within the innexin gene family. The genome of the freshwater cnidarian *Hydra vulgaris* contains 15 predicted innexins, of which, 5 are expressed exclusively in the nervous system. It is presumed that these innexins are expressed in the different circuits of the hydra nervous system. There are 3 well described circuits which regulate 3 different behaviors in hydra; The contractile burst (CB) circuit which coordinates contractions, rhythmic potential 1 (RP1) which coordinates elongations, and rhythmic potential 2 (RP2) which coordinates radial contractions/egestion. Here I present data to show that hydra

innexins are capable of forming gap junctions. The electrophysiology associated with hydra innexins is similar to that of connexins which undergo voltage dependent inactivation. There is clear delineation of properties between INX2, which is expressed in the CB circuit, and the innexins expressed in other neuronal circuits. The CB circuit is known to undergo regular activations which correlates with the contractile behavior of hydra. By removing the hypostome I reveal the presence of CB pacemakers within the hypostome and present a way to facilitate further investigation into regeneration of CB and RP circuits. Lastly, in collaboration with the Fairhall lab, I present imaging and analysis techniques that facilitate the construction of a biomechanical model to simulate the behaviors of hydra.

Table of Contents

Chapter 1: Introduction to Hydra and Gap Junctions **10**
Hydra Phylogeny and Anatomy 10
Hydra Nervous System and Behavior 12
Connexins, Innexins, Pannexins 14
Figures 17
References 19

Chapter 2: Biophysical Characterization of Innexins Expressed in the Hydra Nervous System. **24**
Introduction 24
Methods 27
Results 29
DISCUSSION 42
Figures 45
REFERENCES 55

CHAPTER 3: A BIOMECHANICAL MODEL OF HYDRA MOVEMENT **61**
Manuscript Contribution 61
Introduction 62
Materials and Methods 65
Results 70
Discussion 81
Figures 87

CHAPTER 4: Molecular Properties and Phylogenetics of Hydra Innexins **110**
Introduction 110
Methods 113
Results 114
Discussion 119
Figures 122

References 130

Chapter 5: Regenerating circuits in Hydra vulgaris 138

Introduction 138
Methods 140
Results 142
Discussion 146
Figures 148
References 153

Conclusions and Future Directions 155

Summary of Findings 155
Future Directions 156
References 157

List of Figures

Figure 1.1: Phylogeny and Anatomy 17
Figure 1.2: Connexins, Innexins, and the Electrical Synapse 18
Figure 2.1: Background and Expression 45
Figure 2.2: Homomeric coupling of *Hydra* innexins 46
Figure 2.3: Innexin 2 forms homomeric gap junctions in N2a cells 47
Figure 2.4: Voltage Dependent Inactivation of EC3 Hydra Innexins 48
Figure 2.5: Unitary Conductance of INX2 Homomeric Gap Junctions 49
Figure 2.6: Unitary Conductance of Homomeric Gap Junctions composed of EC3 Cluster Innexins 50
Figure 2.7: Single Channel IV and Dwell Times of *Hydra* Innexins 51
Figure 2.7: Heterotypic Coupling of *Hydra* Innexins 52
Table 2.1: Boltzmann fitting parameters for the voltage inactivation of hydra innexins 53
Table 2.2: Inactivation Time Constants for Hydra Innexins 53
Table 2.3: Dwell Time Statistics for Hydra Innexins 54
Figure 3.1: Simplified Hydra anatomy 87
Figure 3.2: Project Framework 88
Figure 3.3: Single cell dynamics 89
Figure 3.4: Muscle sheet dynamics 90
Figure 3.5: Fluorescent/Length Correlation 91
Figure 3.6: Body column settings and dynamics 92
Figure 3.7: Model Geometry 93
Figure 3.8: Simulated Behaviors 94
Figure 3.9: Pipeline of the simulation from neural activity to behaviors 95
Figure 3.10: Calcium Model 96
Figure 3.11: Analysis Pipeline 96
Figure 4.1: Cnidarian innexin phylogeny 122
Figure 4.2: Hydra Innexin Membrane Topology and Sequence Structure 123
Figure 4.3: Group 1 cnidarian innexins 124

Figure 4.4: Group 2 cnidarian innexins 125
Figure 4.5: Group 3 cnidarian innexins 126
Figure 4.6: Group 4 cnidarian innexins 127
Figure 4.7: Cnidarian innexin-like sequences 128
Table 4.1: Phosphorylation and N-Glycosylation of Groups 2 and 4 Hydra Innexins 129
Figure 5.1: Imaging Pipeline 148
Figure 5.2: Integrated fluorescence and behavior during regeneration 149
Figure 5.3: Circuit activity in regenerating hydra halves 150
Figure 5.4: RP circuit activity in regenerating hydra 151
Figure 5.5: Contraction frequencies in Bisected Hydra 152

Acknowledgments

Most graduate students find many hurdles and roadblocks along their journey through graduate school. I was no exception. I've worked on projects including ctenophores, mice, and hydra. Everytime I figured "that was the project" and I could be out in "just three more years". That turned into three "three more years". But I've finally found my way through not due only to my own work, but to many people along the way.

I'd like to thank my Ph.D. advisor, Martha Bosma, for allowing me to join her lab (after the first "three more years") and allowing me to work on any project I wanted which turned into me bringing a brand new species to her lab. Most of all though thank you for being human and acknowledging life that occurs outside of the lab. Thank you for providing a place for Zach Miller to stay while here in Seattle. It was a blessing for both Karrah and me.

To my undergraduate advisor Dr. Winslow who pushed me to give research and graduate school a try even if I was unsure.

To all of my committee members, Adrienne Fairhall, Tom Daniel, and David Perkel, thank you for advising me and sticking with me through my many years of graduate school. Thank you for your support and helping me make the science better!

To the many members of labs that I've been a part of, thank you for your patience with me as I learned, even if it was slow.

To my friends across the country and in Seattle, thank you for distracting me and enjoying life with me outside the lab.

Finally and most importantly to my wife, Karrah, THANK YOU for your patience, your empathy, your strength and your encouragement. I love you.

Dedication

To my friends and family who have supported me through this journey.

To my wife, Karrah, who has put on hold many of her own ambitions during this time

To my younger self who never dreamed that I could ever achieve this degree

To my God who gives me perseverance Psalm 105:4; Ecclesiastes 3:11

.

Chapter 1: Introduction to Hydra and Gap Junctions

Hydra Phylogeny and Anatomy

While jellyfish and anemones are the most identifiable Cnidarians, the phylum *Cnidaria* is much more diverse than this and unique among all other phyla. *Cnidaria* are characterized by their radial symmetry, unique developmental processes and simplified nervous system. Sister to all bilaterians, only *Ctenophora*, *Porifera* and *Placazoa* are considered to have diverged earlier than *Cnidaria* among the metazoans(Zapata et al., 2015). Cnidarians subphyla are the *Medusozoa* and *Anthozoa*. Medusazoa consists of jellyfish, box-jellies and hydra. Anthozoa consists of corals and anemones (Fig. 1A). Hydrozoans are unique within *Medusozoa* in that they contain numerous freshwater species. *Hydra vulgaris* are a perfect example of a freshwater hydrozoan within the phylum *Cnidaria.*

Hydra is composed of a simple stalk, sensory/predatory tentacles, with a basal foot region, peduncle, used for anchoring (Fig. 1B). The tubular stalk is made up of two layers of transparent epitheliomuscular cells, the outer ectoderm and inner endoderm, enabling high quality imaging of both cell layers(Technau and Steele, 2011). The ectoderm produces a cuticle that protects the animal from pathogens and helps retain the integrity of the hydroskeleton. The endoderm is involved in digestion, food uptake and osmoregulation(Lilly, n.d.; Sher et al., 2008). Endodermal epitheliomuscular cells contain circularly organized myosin filaments that control the diameter of the animal, while in the ectoderm, filaments are longitudinally arranged and control the extension of the animal (Leclère and Röttinger, 2017). Epitheliomuscular cells within each layer are connected by

septate junctions mediating cell adhesion, as well as gap junctions positioned to coordinate electrical signaling between cells (Hand and Gobel, 1972). These two layers both rest on a basal acellular partitioning layer, the mesoglea. Interspersed through both the ectodermal layer and endodermal layer is the nerve net (Fig. 1C). Hydra do not possess a brain to coordinate behavior and therefore rely on a diffuse network of neurons to sense their environment and coordinate behavior.

Large numbers of interstitial stem cells exist in the body column between the endodermal and ectodermal layers of the animal. These totipotent cells allow for remarkable regenerative capabilities (Vogg et al., 2019). Regeneration within hydra has been well documented. The animal can regenerate a completely new hypostome and/or peduncle within four days post bisection. Furthermore the animal can undergo dissociation and completely regenerate, synchronizing its nervous system and re-coordinating its behaviors (Lovas and Yuste, 2021).

Hydra Nervous System and Behavior

Hydra have a well recorded repertoire of behaviors that include contraction, extension, tentacle movements, somersaulting, feeding, and bending (Han et al., 2018). Early extracellular recordings identified several distinct electrical events that coordinate these behaviors in *Hydra*: contraction bursts (CB), rhythmic potentials (RP) and pre locomotion bursts (Passano and Mccullough, 1963; Yamamoto and Yuste, 2020). Genetic advances have supported the creation of hydra that express the calcium indicator GCaMP6 specifically within the interstitial cell line, which develop into the neurons of the animal (Heimfeld and Bode, 1985). Using this line combined with hydras translucency allows for

relatively high resolution full body imaging of the nervous system leading to further characterization of these electrical events. Observations by Dupre and Yuste (2017) show that neurons are organized into specific non overlapping circuits: the contraction burst (CB), rhythmic potential 1 (RP1), and rhythmic potential 2 (RP2)(Dupre and Yuste, 2017).

Synchrony of a neural circuit is likely vital for coordinated behavior in *Hydra*. One key to synchronization is the electrical synapse (Fig. 2A) which is typically composed of a plaque of gap junctions between neurons, or other cells. Hydra neurons are connected via both electrical and chemical synapses (Hand and Gobel, 1972; Westfall et al., 1971). Many studies have pursued the physiological properties of these transmission methods in invertebrates with the chemical synapse having been thoroughly studied in *Aplysia californica* (Camardo et al., 1983; Rubakhin et al., 1999). Chemical synapses allow for cells to remain isolated, but electrical synapses allow direct communication between the cytoplasm of two (or more) cells.

Though the nerve network of hydra clearly coordinates and regulates behaviors, suggesting an important role for gap junctional coupling, such coupling (Josephson) also exists within the epithelial musculature through which excitation propagates (Josephson and Macklin, 1969) even when *Hydra*'s nerve cells have been removed (Lepault et al., 1980). Several studies have suggested that contraction pulses can be conducted by the epithelium in *Hydra* (Josephson, n.d.; Josephson and Macklin, 1969). By imaging calcium signals in the endo- and ectodermal epithelial layers, (Szymanski and Yuste, 2019) reported two distinct forms of muscle layer activation: a rapid global activation that drives whole-body contraction (contraction pulse), and slow waves of local activation that can

initiate anywhere in the body column (body column wave) or at a region of the peduncle and correlate with bending (bending wave). This suggests that the dynamics of the muscle layer itself form an important and nontrivial component of the transformation from nerve firing to behavior.

Connexins, Innexins, Pannexins

Gap junctions clearly play an important role in synchronization and propagation of signals within hydra and other animals. What genes encode gap junctions? Three different protein families are known to encode gap junctions or gap junction-like proteins: innexins, connexins, and pannexins(Sahu et al., 2015; Skerrett and Williams, 2017). Connexins are found exclusively in vertebrates whereas innexins are found exclusively in invertebrates (Bao et al., 2007). Pannexins do share some sequence homology with the other families and are found in both vertebrates and invertebrates. Pannexins have been hypothesized to be the evolutionary link between the connexin and innexin gene families (Beyer and Berthoud, 2018)(Evans and Martin, 2002; Landesman, n.d.; Moreno et al., 1995). Despite little sequence homology they have surprisingly similar physical structure: four transmembrane domains and two extracellular loops (Fig. 2B&C). Functionally, innexins and connexins create very similar gap junction channels despite very little DNA/Amino acid sequence homology (Evans and Martin, 2002; Landesman, n.d.; Moreno et al., 1995)) While connexin/innexin hemichannels dock to form gap junctions, pannexins primarily form hemichannels that do not dock, and instead create intracellular hemichannels (Baranova et al., 2004; Sahu et al., 2015).

Gap junctions form between two cells each expressing connexin/innexin hemichannels. When the two docking hemichannels each express identical connexin/innexin genes it is known as a homomeric/typic gap junction (Fig. 2D) Cells expressing hemichannels composed of different innexins (while not chimeric) are known as heterotypic gap junctions (Fig. 2 E). If an individual hemichannel is composed of multiple innexin genes the resulting gap junction would be in the heterotypic conformation (Fig. 2 F). While these conformations have been established in the connexin gene family it is presumed that these rules apply to innexins as well.

Channel structure between these convergent genes, connexins and innexins has observed differences due to low sequence homology. Connexins have been shown to assemble with six connexon subunits creating a hexamer hemichannel (Lee et al., 2020; Unwin and Zampighi, 1980). Pannexin channels, thought to be the evolutionary link between innexins and connexins assemble with seven subunits (Michalski et al., 2020), and innexin forms octomer hemichannels (Oshima, 2017). Cells coupled with connexins exhibit smaller spacing in the electrical synapse (20–30 Å) and the spacing between channels is also smaller (75-95 Å) when compared to innexins (30-40 Å and 90-120 Å respectively)(Skerrett and Williams, 2017). These differences likely lead to different biophysical properties as well.

Both the Hydra genome and single cell transcriptome have revealed fifteen proposed innexin genes and their variants (Chapman et al., 2010; Siebert et al., 2019). In situ hybridizations localized hydra innexin 2 (INX2) to the CB circuit of the neural net of hydra antibody blocking has further revealed that innexin-2 may play a role in synchronizing the

contractile behavior of the animal (Takaku et al., 2014). The hydra single cell transcriptome has established cell type specific expression of hydra innexins localizing a number of hydra innexins to be expressed exclusively in the nerve net of the animal.

This thesis sets out to better characterize gap junctions expressed in the hydra nervous system, both functionally and molecularly. Furthermore, in collaboration with Hengji Wang (Fairhall lab) we explore a model for behavior and seek to better understand how circuits regenerate. Functional innexin studies are few and the molecular characterization of Cnidarian, specifically hydrozoan, innexins is muddled. Combining phylogenetic, electrophysiological, calcium imaging and collaborative computational techniques, we begin to expand our understanding of the hydra nervous system and its relationship with behavior.

Figures

Figure 1. Phylogeny and Anatomy

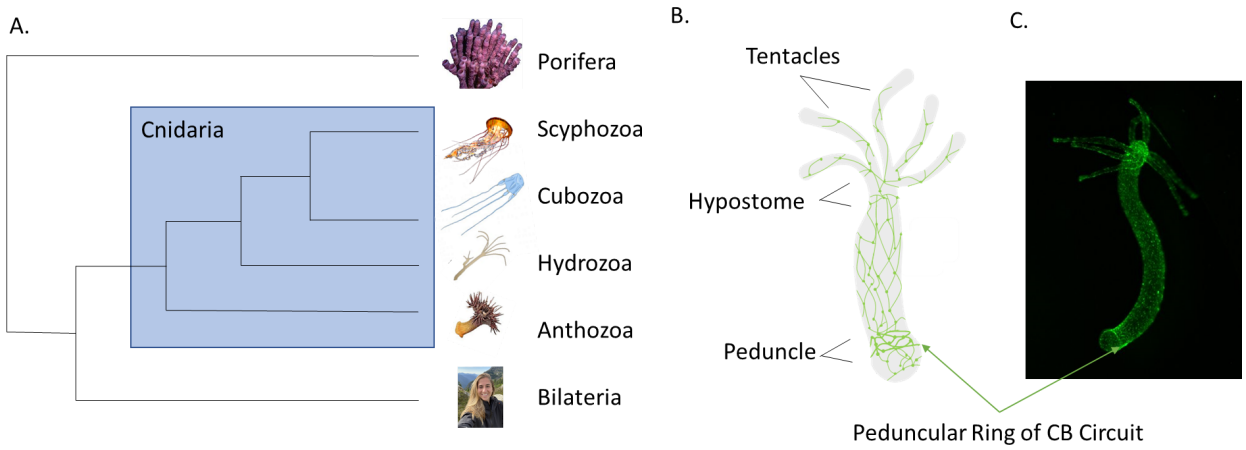

Figure 1. Phylogeny and Anatomy

A) Phylogeny of Cnidarians. Sister to all bilaterians. B) Cartoon anatomy displaying tentacles, hypostome and peduncle. Nerve net is visible in green. C) Photograph of hydra nerve net which is expressing GFP

Figure 2. Connexins, Innexins And the Electrical Synapse

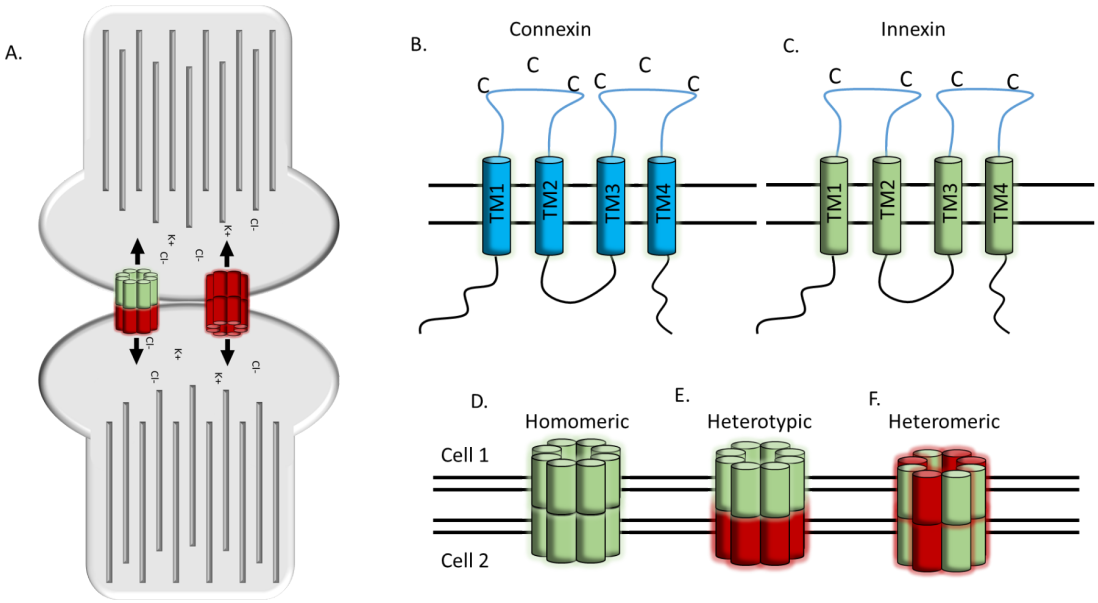

Figure 2. Connexins, Innexins, and the Electrical Synapse.

A) Schematic displaying gap junctions (homomeric and heterotypic) between two neurons B) Connexin membrane topology with characteristic 6 conserved cysteine residues. C) Innexin membrane topology with characteristic four conserved cysteine residues. D)-F) Possible gap junction formations based on connexins/innexins expressed in each cell, Homomeric, Heterotypic, Heteromeric.

References

Bao L, Samuels S, Locovei S, Macagno ER, Muller KJ, Dahl G. 2007. Innexins form two types of channels. *FEBS Lett* **581**:5703–5708. doi:10.1016/j.febslet.2007.11.030

Baranova A, Ivanov D, Petrash N, Pestova A, Skoblov M, Kelmanson I, Shagin D, Nazarenko S, Geraymovych E, Litvin O, Tiunova A, Born TL, Usman N, Staroverov D, Lukyanov S, Panchin Y. 2004. The mammalian pannexin family is homologous to the invertebrate innexin gap junction proteins. *Genomics* **83**:706–716. doi:10.1016/j.ygeno.2003.09.025

Beyer EC, Berthoud VM. 2018. Gap junction gene and protein families: Connexins, innexins, and pannexins. *Biochim Biophys Acta BBA - Biomembr* **1860**:5–8. doi:10.1016/j.bbamem.2017.05.016

Camardo J, Proshansky E, Schacher S. 1983. Identified Aplysia neurons form specific chemical synapses in culture. *J Neurosci* **3**:2614–2620. doi:10.1523/JNEUROSCI.03-12-02614.1983

Chapman JA, Kirkness EF, Simakov O, Hampson SE, Mitros T, Weinmaier T, Rattei T, Balasubramanian PG, Borman J, Busam D, Disbennett K, Pfannkoch C, Sumin N, Sutton GG, Viswanathan LD, Walenz B, Goodstein DM, Hellsten U, Kawashima T, Prochnik SE, Putnam NH, Shu S, Blumberg B, Dana CE, Gee L, Kibler DF, Law L, Lindgens D, Martinez DE, Peng J, Wigge PA, Bertulat B, Guder C, Nakamura Y, Ozbek S, Watanabe H, Khalturin K, Hemmrich G, Franke A, Augustin R, Fraune S, Hayakawa E, Hayakawa S, Hirose M, Hwang JS, Ikeo K, Nishimiya-Fujisawa C, Ogura A,

Takahashi T, Steinmetz PRH, Zhang X, Aufschnaiter R, Eder M-K, Gorny A-K, Salvenmoser W, Heimberg AM, Wheeler BM, Peterson KJ, Böttger A, Tischler P, Wolf A, Gojobori T, Remington KA, Strausberg RL, Venter JC, Technau U, Hobmayer B, Bosch TCG, Holstein TW, Fujisawa T, Bode HR, David CN, Rokhsar DS, Steele RE. 2010. The dynamic genome of Hydra. *Nature* **464**:592–596. doi:10.1038/nature08830

Dupre C, Yuste R. 2017. Non-overlapping Neural Networks in Hydra vulgaris. *Curr Biol* **27**:1085–1097. doi:10.1016/j.cub.2017.02.049

Evans WH, Martin PEM. 2002. Gap junctions: structure and function (Review). *Mol Membr Biol* **19**:121–136. doi:10.1080/09687680210139839

Han S, Taralova E, Dupre C, Yuste R. 2018. Comprehensive machine learning analysis of Hydra behavior reveals a stable basal behavioral repertoire. *eLife* **7**:e32605. doi:10.7554/eLife.32605

Hand AR, Gobel S. 1972. THE STRUCTURAL ORGANIZATION OF THE SEPTATE AND GAP JUNCTIONS OF HYDRA. *J Cell Biol* **52**:397–408. doi:10.1083/jcb.52.2.397

Heimfeld S, Bode HR. 1985. Growth regulation of the interstitial cell population in hydra: I. Evidence for global control by nerve cells in the head. *Dev Biol* **110**:297–307. doi:10.1016/0012-1606(85)90089-2

Josephson RK. n.d. CONDUCTION AND CONTRACTION IN THE COLUMN OF HYDRA 12.

Josephson RK, Macklin M. 1969. Electrical Properties of the Body Wall of Hydra. *J Gen Physiol* **53**:638–665. doi:10.1085/jgp.53.5.638

Landesman Y. n.d. Innexin-3 forms connexin-like intercellular channels 6.

Leclère L, Röttinger E. 2017. Diversity of Cnidarian Muscles: Function, Anatomy, Development and Regeneration. *Front Cell Dev Biol* **4**. doi:10.3389/fcell.2016.00157

Lee H-J, Jeong H, Hyun J, Ryu B, Park K, Lim H-H, Yoo J, Woo J-S. 2020. Cryo-EM structure of human Cx31.3/GJC3 connexin hemichannel. *Sci Adv* **6**:eaba4996. doi:10.1126/sciadv.aba4996

Lilly SJ. n.d. OSMOREGULATION AND IONIC REGULATION IN HYDRA 17.

Lovas JR, Yuste R. 2021. Ensemble synchronization in the reassembly of Hydra's nervous system. *Curr Biol* **31**:3784-3796.e3. doi:10.1016/j.cub.2021.06.047

Michalski K, Syrjanen JL, Henze E, Kumpf J, Furukawa H, Kawate T. 2020. The Cryo-EM structure of pannexin 1 reveals unique motifs for ion selection and inhibition. *eLife* **9**:e54670. doi:10.7554/eLife.54670

Moreno AP, Laing JG, Beyer EC, Spray DC. 1995. Properties of gap junction channels formed of connexin 45 endogenously expressed in human hepatoma (SKHep1) cells. *Am J Physiol-Cell Physiol* **268**:C356–C365. doi:10.1152/ajpcell.1995.268.2.C356

Oshima A. 2017. Structure of an innexin gap junction channel and cryo-EM sample preparation. *Microscopy* **66**:371–379. doi:10.1093/jmicro/dfx035

Passano LM, Mccullough CB. 1963. Pacemaker Hierarchies Controlling the Behaviour of Hydras. *Nature* **199**:1174–1175. doi:10.1038/1991174a0

Rubakhin SS, Li L, Moroz TP, Sweedler JV. 1999. Characterization of the *Aplysia californica*

Cerebral Ganglion F Cluster. *J Neurophysiol* **81**:1251–1260. doi:10.1152/jn.1999.81.3.1251

Sahu G, Sukumaran S, Bera AK. 2015. Pannexins form gap junctions with electrophysiological and pharmacological properties distinct from connexins. *Sci Rep* **4**:4955. doi:10.1038/srep04955

Sher D, Fishman Y, Melamed-Book N, Zhang M, Zlotkin E. 2008. Osmotically driven prey disintegration in the gastrovascular cavity of the green hydra by a pore-forming protein. *FASEB J* **22**:207–214. doi:10.1096/fj.07-9133com

Siebert S, Farrell JA, Cazet JF, Abeykoon Y, Primack AS, Schnitzler CE, Juliano CE. 2019. Stem cell differentiation trajectories in *Hydra* resolved at single-cell resolution. *Science* **365**:eaav9314. doi:10.1126/science.aav9314

Skerrett IM, Williams JB. 2017. A structural and functional comparison of gap junction channels composed of connexins and innexins: Structural and Functional Comparison of Gap Junction Channels. *Dev Neurobiol* **77**:522–547. doi:10.1002/dneu.22447

Szymanski JR, Yuste R. 2019. Mapping the Whole-Body Muscle Activity of Hydra vulgaris. *Curr Biol* **29**:1807-1817.e3. doi:10.1016/j.cub.2019.05.012

Takaku Y, Hwang JS, Wolf A, Böttger A, Shimizu H, David CN, Gojobori T. 2014. Innexin gap junctions in nerve cells coordinate spontaneous contractile behavior in Hydra polyps. *Sci Rep* **4**:3573. doi:10.1038/srep03573

Technau U, Steele RE. 2011. Evolutionary crossroads in developmental biology: Cnidaria.

Development **138**:1447–1458. doi:10.1242/dev.048959

Unwin PNT, Zampighi G. 1980. Structure of the junction between communicating cells. *Nature* **283**:545–549. doi:10.1038/283545a0

Vogg MC, Galliot B, Tsiairis CD. 2019. Model systems for regeneration: *Hydra*. *Development* **146**:dev177212. doi:10.1242/dev.177212

Westfall JA, Yamataka S, Enos PD. 1971. ULTRASTRUCTURAL EVIDENCE OF POLARIZED SYNAPSES IN THE NERVE NET OF HYDRA. *J Cell Biol* **51**:318–323. doi:10.1083/jcb.51.1.318

Yamamoto W, Yuste R. 2020. Whole-Body Imaging of Neural and Muscle Activity during Behavior in *Hydra vulgaris* : Effect of Osmolarity on Contraction Bursts. *eneuro* **7**:ENEURO.0539-19.2020. doi:10.1523/ENEURO.0539-19.2020

Zapata F, Goetz FE, Smith SA, Howison M, Siebert S, Church SH, Sanders SM, Ames CL, McFadden CS, France SC, Daly M, Collins AG, Haddock SHD, Dunn CW, Cartwright P. 2015. Phylogenomic Analyses Support Traditional Relationships within Cnidaria. *PLOS ONE* **10**:e0139068. doi:10.1371/journal.pone.0139068

Chapter 2: Biophysical Characterization of Innexins Expressed in the Hydra Nervous System.

Introduction

Cell to cell communication is an essential component of biology and vital for a functional nervous system. Neurons use two primary mechanisms for communication, chemical and electrical synapses. These modes of transmission are well documented in both vertebrate and invertebrate systems. Within invertebrates, many studies have pursued the mechanics of these transmission methods in invertebrates with both chemical synapse and electrical synapses having been thoroughly studied in *Aplysia californica* and *D. melanogaster* (Camardo et al., 1983; Rubakhin et al., 1999, Chou et al., 2020; Li et al., 1997; Pereda, 2014; Rybak et al., 2016; Stark et al., 1989). Chemical synapses allow for cells to remain isolated, but electrical synapses allow direct communication between the cytoplasm of two (or more) cells. Electrical synapses are composed of plaques of gap junction channels which are coded for by the connexin gene family in vertebrate animals.

Invertebrate animals have an analogous gene family, innexins, that have been suggested to form connexin-like gap junction channels analogous to their vertebrate counterparts.

In *Drosophila*, innexins have been demonstrated, via knockdown/out experiments, to carry out a wide variety of functions. A single dual-patch clamp study on shaker-B tested the functional role of the innexin gene family by injecting oocytes with shaker-B RNA and found that these genes are capable of making gap junction-like channels. (Phelan et al., 1998). Similarly, exogenous expression of *C. elegans* innexin-3 RNA CDS in Xenopus oocytes demonstrated that the product formed gap junction channels when two oocytes were brought into contact in a dual whole cell conformation(Landesman, n.d.). These are the two known examples demonstrating that innexins form connexin-like channels.

Gap junctions are made when two hexameric (connexins)or octomeric (innexins)(Evans and Martin, 2002) hemichannels expressed in the plasma membrane of adjacent cells dock together. When two hemichannels expressing identical innexin genes dock it is known as a homomeric/typic gap junction(Fig. 1A). Cells expressing hemichannels composed of different innexins that are able to dock (while not chimeric) are known as heterotypic gap junctions (Fig. 1A). If an individual hemichannel is composed of multiple innexin gene products within one cell, the resulting gap junction is said to be in the heteromeric conformation (not shown). While these conformations have been established in the connexin gene family it is unknown whether these same conformations can occur in innexin based gap junctions as well.

The freshwater hydrozoan, *Hydra vulgaris*, does not possess a centralized nervous system like bilaterians but instead uses a nerve net to sense their environment and control

their behaviors. *Hydra* have a well studied repertoire of behaviors that include contraction, extension, tentacle movements, somersaulting, feeding, and bending. Genetic advances have supported the creation of *Hydra* that express the calcium indicator GCaMP6 specifically within the interstitial cell line. Imaging from *Hydra* expressing GCaMP6 within the nerve net has allowed the direct observation of a number of previously identified firing patterns, the contraction burst (CB), rhythmic potential 1 (RP1), and rhythmic potential 2 (RP2), associated with circuits within the nerve net of the animal that regulate and control some of these behaviors (Passano and Mccullough, Dupre et al., 2017). Dupre and Yuste (2017) showed that these three circuits appear to consist of nonoverlaping sets of neurons and that the firing of neurons within each circuit is synchronous.

Synchronicity of firing neurons is known to be coordinated by gap junctions in mammalian systems (Bennett and Zukin, 2004). Gap junctions in vertebrate systems are coded for by the connexin gene family (Evans and Martin, 2002; Phelan and Starich, 2001; Ramanan and Brink, 1993). However, no connexin genes have been identified in invertebrate systems and instead gap junctions are coded for by the innexin gene family in invertebrate animals (Adams et al., 2000; Chapman et al., 2010; Hillier et al., 2008; Leclère et al., 2019; Welzel and Schuster, 2022). *Hydra* is no exception, with fifteen proposed innexin genes identified by whole genome sequencing. *In situ* hybridizations localized *Hydra* innexin 2 (INX2) to the CB circuit of the neural net of *Hydra* and antibody blocking has revealed that innexin-2 may play a role in synchronizing the contractile behavior (CB) of the animal (Takaku et al., 2014). A recently derived *Hydra* single cell transcriptome has established cell type specific expression of *Hydra* innexins (Siebert et al., 2019). Using this

data we identified five *Hydra* innexins that are expressed in the neural cluster with diverse expression across the nerve net Fig. 1 B).

Despite these advances the functional characterization of any *Hydra* innexin has yet to be established. We show for the first time that these innexins are capable of forming gap junctions similar to those formed by connexins and we characterize their electrical properties. Here we present evidence that innexins are capable of creating both homomeric and heterotypic gap junctions. This is the first study to characterize invertebrate innexins in over twenty years and the first to explore the properties of all innexins expressed in a nervous system.

Methods

Plasmid Design

Hydra innexin sequences were identified using the drop seq paper. We used gene wiz to synthesize the gene. We acquired the pNeuroD-ires-GFP as pNeuroD-ires-GFP was a gift from Franck Polleux (Addgene plasmid # 61403 ; http://n2t.net/addgene:61403 ; RRID:Addgene_61403). The UW Biofab was used to subclone the hydra innexin into the pneuroD-ires-GFP vector.

Cell Culture and Transfection

N2a cells were acquired from American Type Culture Collection (ATCC), Manassas, VA, USA. initial cells were cultured through 3 passages and then stocks were aliquoted and frozen for future use. Cells were incubated in DMEM with 10% FBS and 1% penstrep, kept at 37C in 5% CO2. We then used transfectamin 5000 to exogenously express hydra innexins in N2a

cells. During transformation N2a cells were incubated in Opti-MEM at 37C in 5%CO2 for a period up to 24hours. Expression was confirmed via visual GFP expression under an Olympus inverted microscope.

Dual Patch Electrical Recordings

Gap junctional current recordings were acquired using dual whole cell patch clamp techniques. Borosilicate pipettes with access resistance for whole cell patch electrodes were initially measured between 3.5 and 5 mOhm and filled with an internal solution composed of 130mM CsCl, 10mM EGTA, .5mM CaCl2, 3mMMgATP, 10mMHEPES, and 18mM phosphocreatine. Neuro2a blastoma cells were plated onto a cover slip 1.5-2 hours prior to experiments and bathed in a solution of 140mM NaCl, 2mM CsCl, 2mM CaCl, 5.5mM Glucose, 1mM mgCl, 10mM HEPES, 5mM KCl. Coupled cells were identified by the expression of GFP under an Olympus inverted microscope. Electrodes were brought to the membrane of each cell and the gigaOhm seal was acquired before breaking into the cell. Both cells were clamped at 0mv prior to voltage steps. The command cell was then stepped from -70mV to +70mV in 10mV or 20mV steps while the recording cell was held at 0mV. In some cases one of the pair was held at -70mV or -30mV for 90 seconds to observe single channel events. Changes in current due to the voltage differential were recorded in both the command and recording cells.

Dual patch clamp was achieved via Axopatch 700A and B amplifiers (Molecular Devices, Sunnyvale, CA) with a low-pass filter (cut-off frequency 1 kHz) and digitized at a 10 kHz sampling rate using an AD/DA converter (Digidata 1550, Molecular Devices, Sunnyvale, CA).

Single Channel Analysis

To calculate the single channel current event histograms were produced and distance between peaks or regular intervals was determined to be the single channel conductance of the channel. The number of channels was calculated by dividing the macroscopic current by the single channel current allowing us to further calculate the open probability of a given gap junction

Voltage Dependent Inactivation analysis

Files from each experiment were averaged to remove noise and individual gap junction channels opening and closing using both custom python scripts and Clampfit software. Next, the steady-state conductance during a voltage pulse was normalized to the peak of the same pulse and then plotted as a function of voltage. A Boltzmann equation was used to fit these plots. Averaged files were also used to plot steady state current as a function of voltage and peak current as a function of voltage.

Results

Exogenous Expression of Hydra Innexins in N2a Cells

Hydra Innexins were originally identified through the Hydra genome project and later through the hydra single cell transcriptome (Chapman et al., 2010; Siebert et al., 2019). Using the hydra single cell transcriptome and in collaboration with those authors, we identified five hydra innexins predominantly expressed in the nervous system of hydra. These innexins, Innexin 2(*INX2*), Innexin 6 (*INX6*), Innexin 7 (*INX7*), Innexin 10 (*INX10*), and Innexin 14 (*INX14*) have differential expression within the clusters of the single cell

transcriptome. *INX2* is expressed in the EC1A, EC1B, and EC5 clusters, all of which are in the ectoderm of the animal(Fig. 1B). Antibody blocking of INX2 gap junctions has suggested that INX2 coordinates and synchronizes the CB network. Since INX2 is expressed in the EC1/5 clusters, these clusters likely contain neurons of the CB network (Siebert et al., 2019; Takaku et al., 2014). In the endoderm of the animal *INX2* is expressed in the EN3 cluster; we do not discuss endodermal expression further. INX6, INX7, INX10, INX14 are all expressed in the EC3B and EC3C clusters of the single cell transcriptome, all of which are located in the ectoderm of the animal but separate from the expression of INX2 (Fig. 1B); these are hypothesized to be associated with the RP1 and RP2 circuits. Also of note is that any given cell within the neural clusters will only express one *Hydra* innexin gene, preventing the formation of heteromeric gap junctions (multiple innexin genes expressed within one cell), but allowing for the formation of both homomeric and heterotypic gap junctions between cells (data not shown)(Siebert et al., 2019).

In order to study the plausible channel formation of hydra innexin genes, we synthesized innexin genes (genewiz) and cloned them into a modified pNeuroD-ires-GFP plasmid (Guerrier et al., 2009)(Fig. 1C). This modified plasmid uses the Mammalian EF1-alpha promoter to drive expression of genes of interest, in this case a specific hydra innexin, as well as a fluorophore (either GFP or TdTomato). Plasmids were then independently transformed into mouse N2a cells via Polysciences, Inc. Transporter 5 Transfection Reagent from Fisher Scientific and verified via reporter expression under UV or Green light state wavelength. Expression of hydra Innexins in N2a cells via reporter fluorescence can be seen in Figure 1D.

N2a cells were chosen for use in this study because they do not contain detectable levels of endogenous connexin expression (Elenes et al., 2001). In order to further verify lack of gap junction expression, we experimentally tested wild-type N2a with dual whole cell voltage clamp and dye transfer experiments (Fig. 1E, F) to demonstrate that WT N2a cells do NOT couple making them an ideal cell line in which to study invertebrate innexins.

Homomeric coupling of Hydra Innexins

We used the dual whole-cell voltage clamp technique to test the ability of hydra innexins to form functional gap junction channels. To do so, N2a cells transfected with Hydra *INX2*, *INX6*, *INX7*, *INX10*, or *INX14* were plated onto coverslips >48hours after transfections and 2-24 hours prior to experiments. Cells expressing the respective reporter gene (ie. GFP) were identified and adjacent cells were presumed to form plaques of homomeric gap junction channels. During formation of dual patch clamp recordings, membrane potential was initially clamped to 0mV in both cells. Once whole cell access was achieved one of the two cells was stepped from -80mV to +80mv in 10 or 20mV steps with current amplitude being measured in both cells (Fig. 2 A,B). Current measured in the cell clamped at 0mV for the duration of the experiment indicated successfully coupled cells via gap junctions composed of *Hydra* innexins. All innexins tested in this study successfully created gap junctions with varying coupling rates (Fig. 2 C). We observed a coupling rate of 83% in INX2, 71% in INX6, 55% in INX7, 50% in INX10 and 86% in INX14 homomeric gap junctions (Fig. 2 C). The current amplitude recorded in cells ranged widely, presumably due to the number of gap junction channels present between cells. Whether at the macroscopic

current level, or at the level of single channel recording, the biophysical properties of inactivation were consistently observed in homomeric gap junctions.

Voltage Dependent Inactivation of Innexin 2 Gap Junctions

Voltage dependent inactivation is a canonical kinetic observed in connexin-based gap junctions (Elenes et al., 2001; Moreno et al., 1994; Santos-Miranda et al., 2019; Yue et al., 2021) and previously described in innexin (*Drosophila, C. elegans*) gap junctions (Landesman, n.d.; Phelan et al., 1998). We show here that voltage dependent inactivation is consistent with *Hydra* neural innexins forming homomeric gap junctions. Adjacent cells with potential gap junctions were identified and stepped from ±80 mV in 10 or 20mV steps (Fig. 3A). We then calculated the current/voltage (I/V) relationship for both the instantaneous current (Ip) (defined as the average current within the first 100ms of a voltage pulse) and the steady state (*Iss*) current (defined as the current during the final 0.5s of a voltage pulse). While instantaneous INX2 current displayed a linear relationship across the range of voltage steps, *Iss* deviated from linearity at larger potential differences, due to channel inactivation (Fig. 3B). INX2 Iss begins to deviate from linearity at ±20mv (Fig. 3B) which indicates that INX2 channels begin to inactivate at this potential. We next normalized Iss to the instantaneous current at all voltages to obtain normalized conductance relative to voltage (Gss-Vj). Gss-Vj plots were then fitted with separate Boltzmann equations for both positive and negative voltages allowing us to observe the amount of inactivation INX2 channels undergo. The steady state conductance (GJss) for Innexin 2 homomeric channels inactivated to a maximum of 0.49 ±.03 GJss of instantaneous current when a ±80mV potential is applied (Fig. 3C). Boltzmann fit parameters are shown in Table 1.

We next calculated the rate of inactivation for INX2 channels. We first averaged traces corresponding to the voltage pulse across an experiment. We then fit the averaged traces from voltage pulses of ±70mV and ±50mV of each of the eight experiments to a two term exponential equation, yielding a fast (τ_1) and slow (τ_2) component of inactivation. Most traces were best fit with a two term exponential equation (with time constants τ_1 and τ_2), however in some cases traces held at +-50mV were adequately fit with a single exponential (time constant τ).

The average fast inactivation component , τ_1, for INX2 channels was calculated to be 8.6 ms at ±70mV and 109.3mS at ±50mV (Fig. 3D). The τ_2 increased for both voltages reaching 144.5 ms at ±70 and 799.9 ms at ±50mV (Fig. 3D (inset)). Thus, larger voltage pulses caused greater inactivation; this relationship was fairly steep, since at voltages between ±40mV inactivation time constants were inconsistent and extremely long indicating that the true Iss was not reached during a 5 second voltage pulse and in some cases that inactivation simply did not occur.

All innexin-mediated currents showed two time constants of inactivation at +70 mV; those recorded at +50 mV showed slower inactivation, although most channels still had two time constants of inactivation.

Voltage Dependent Inactivation Among EC3 Hydra Innexins

N2a cells transformed with pNeuroD-ires-GFP plasmids containing the EC3 cluster innexins were used for dual whole cell voltage clamp experiments. Homomeric gap junctions created by innexins expressed in the EC3 cluster all exhibited similar biophysical properties which were distinct from those in INX2 homomeric gap junctions. For example INX14 homomeric current records displayed strong voltage-dependent inactivation (Fig.

4A). I/V curves for both Ip and Iss were non-linear indicating that some inactivation or other non-ohmic restriction could be occurring during Ip (Fig. 4E). Gss-Vj plots revealed substantial inactivation, far more than INX2 homomeric gap junctions (Fig. 4I, Table1). GJss of INX14 homomeric gap junctions inactivated to 80% of the instantaneous conductance (Fig. 4I). INX14 also inactivated slightly faster than INX2. Current records for voltage pulses of ±70mV were best fit with a two term exponential fit and averaged a τ1 of 7.4ms and τ2 of 163.6 mS both faster than those of INX2(Fig. 4M, Table 2). Similarly, time constants in response to voltage pulses of ±50mV revealed faster inactivation than that of INX2 (Fig. 4M, Table 2.)

All innexins of the EC3 cluster exhibited these same characteristics when compared to INX2 (Fig. 4B-D). Iss IV relationships for INX6, 7, 10 all displayed non-linearity (Fig. 4F-H). Ip INX6 appears to be linear whereas INX7 and INX10 both display a deviation from linearity at the largest potentials(Fig4F-H). GJss-Vj plots for these innexins all demonstrate greater inactivation than that seen in INX2 (Fig. 4J-L, Table 1). Inactivation time constants were the only parameters not to correlate with expression and biophysical properties. INX6 and INX10 both exhibited longer τ1 and τ2 than INX2 (Fig. 4N,P), while time constants for INX7 were both faster than INX2 (Fig. 4O).

Single Channel Conductance of Innexin 2 gap junctions

We next investigated the unitary conductance of hydra innexins to better understand channel characteristics at the macroscopic and microscopic levels. This provides further insight into how INX2 differs from the *Hydra* innexins expressed in the EC3 Circuit. To observe and quantify unitary values of INX currents, we chose cell pairs in which low values of current were expressed, allowing visualization of current jumps

consistent with opening or closing of single channels. A single cell of a pair was held at either ±30mV or ±70mv for 90 seconds while channel transitions were recorded in the second cell which was held at 0mV. We then measured current amplitude changes by computing histograms of all sampled current values ("all points"), and the current after a discrete change (signifying channel opening or closing "event"). Amplitude and conductance histograms were fit with a Gaussian to evaluate the means and variance of state values.

INX2

±30mV

INX2 homomeric gap junctions exhibited unique unitary conductance characteristics compared to other hydra innexins. A large main state unitary conductance of 162.7pS can be observed in the all points histogram to the right of the channel trace at ±30mV potential Fig. 5A), with a second "main state" of 346pS also recorded, likely the result of a second channel opening. In addition, a short switch event to a subconductance level of 217 pS is seen (red arrow) and is observed at very low probability in the "all points" histogram. When measuring the time spent in the conductance levels defined by thresholded transitions in all three recordings the event histogram reveals four equally distributed peaks separated by 81.8pS. Peaks fit at 81.8 and 246.6 pS in the event peaks are rare across all experiments. These events are short, under 250ms, occurring in only 3 recordings across 8 experiments. Due to this low probability we suggest that these events are part of sub conductive states and the main open state for the INX2 channels is the 165 pS conductance level, with brief transitions to the 50% subconductance level of ~80 pS. (Fig. 5B). At +/- 30

mV, the channels have a high probability of staying open, thus the all points histogram does not demonstrate the unitary conductance of ~80 pS.

±70mV

Given that analysis of the macroscopic currents demonstrated substantial inactivation at larger applied voltages, we might expect that single channel conductance at larger potentials might reveal a higher probability for channels to close at those more positive potentials. With application of ±70mV potential, the channel opened only infrequently to the full conductance level of ~165 pS, and showed substantial dwell times in subconductance levels in INX2 gap junction current. The all points histogram demonstrates a high probability open state conductance level of 35pS in the recording, suggesting that at large potentials, the channels tend to enter lower conductance levels . Three additional subconductance states are observed at 86pS, 134pS and 221pS Fig. 5C). The event histogram for ±70mV reveals five peaks separated by ~35pS each, indicating that although the main open level of 165 pS level recorded at +/- 30 mV is attained, channels prefer the lower sub-conductance levels at larger voltage steps (Fig. 5D).

Single Channel Conductance of EC3 Innexins

As delineated below, all innexin channels of the EC3 cluster displayed lower unitary conductance than INX2 during voltage pulses of ±30mV; however, similarly to INX2, and as expected from the macroscopic kinetics, all EC3 cluster innexins also spent more time in subconductance levels at larger voltages of ±70mV.

INX7

±30mV

The representative current recording clearly shows many open/close transitions and the all points histogram displays peaks of 40.4pS, 75.9pS, 111.9pS and 148.8pS (Fig. 6A). This indicates at least four channels in the recording. Peaks greater than 40.4pS are a summation of current from multiple open channels. Upon close inspection of the representative current recording it is apparent that INX7 based gap junctions can undergo infrequent tenures in a subconductance state indicated by the red arrow (~70pS) in Fig.6A. The event analysis histogram for INX7 displays three conductance states between 0 and 140pS(Fig. 6E) Peaks were fit at 38.2ps, 75.4pS and 114.3pS and separated by ~38pS indicating a single channel conductance of 38pS during voltage pulses ±30mV, substantially lower than that for INX2.

±70mV

Innexin 7 also displays significant tenure within the closed state of the channel, and at subconductance states at ±70mV potential. Current traces display four states which are fitted at 23.4pS, 44.7pS, 70.8pS, 93.7pS (Fig. 6I). Event analysis reveals seven peaks between 0 and 140pS. Peaks of 12.5pS, 24.8pS, 39.1pS, 52.8pS, 77.4pS, 104.8pS and 133.5pS are well fitted by a Gaussian distribution. With multiple channels and substates, summation of multichannel main and substate currents will result in values that may not be well represented in an event analysis from multiple recordings.

INX10

±30mV

Innexin 10 homomeric gap junctions exhibit a main state of 34.0pS which is displayed by the first peak in the event analysis in (Fig. 6B). There are also three additional peaks at 66.2pS, 97.1 pS, and 129.9pS. These peaks are all separated by about 32pS indicating a unitary conductance of ~32pS in INX10 homomeric gap junctions. The representative current trace displays two states at 36.8pS, 69.8pS which are both matched with an associated Gaussian curve of the event analysis (Fig. 6F).

±70mV

Sub-conductive states can also be seen in INX10 homomeric gap junctions as the main state is reduced from 34ps at ±30mV to 21.8pS at ±70mV (Fig. 6J). Additionally, there are five well fitted Gaussian peaks at 21.8pS, 47.8pS, 76.3pS, 105.4pS, and 134.2pS between 0 and 140mV with a ±70mV potential in the event histogram (Fig. 6N). The presence of an additional peak at ±70mV indicates a change in the conductive properties of INX10 at a higher voltage which can be explained by the presence of subconductance states. Additionally the representative current trace displays four states at 21.8pS, 42.5pS, 60.4pS, 76.0pS. The 60.4pS state in this trace represents 14.4pS state change from 76.0pS which is significantly less than the observed transitions of 21+pS. This state also lies between two peaks in the event analysis which supports the hypothesis that this transition is an example of INX10 channels exhibiting a sub-conductive state.

INX14

±30mV

At ±30mV INX14 homomeric gap junctions conduct about 30pS (Fig. 6C). This can be observed in the all points histogram with peaks at 29pS, 63pS and 98pS in the example

trace , suggesting a gap junctional plaque containing at least 4 channels. Inspection of the current traces suggests that the channels have a relatively high probability of being closed, as there is roughly 30% inactivation of INX14 current at ±30 mV. The event histogram has four well fitted peaks between 0 and 150pS separated by 32.75pS ± 2.25pS (Fig. 6G).

±70mV

From the macroscopic analysis of INX14, the current is 80% inactivated at ±70mV. In the recording shown, there are few channel openings, with the all points histogram showing that the channels are mostly closed (Fig. 6K). The event histogram reveals five well fitted peaks between 0 and 150pS at 28pS, 53pS, 82pS, 112pS, and 139pS (Fig. 6O). These peaks are separated by 27.8pS ±2.75pS. Indicating a subconductance of 27.8pS per channel at ±70mV.

INX6

±30mV

The current recording seen in Figure 6A reveals the presence of multiple channels in the system. Multiple opening and closing transitions are apparent and an all points histogram reveals four peaks at 34pS, 93pS, 148pS, and 189.5pS (Fig. 6D). These peaks represent the summation of current through open channels. With this in mind we can deduce a total of 5 channels present in the recording(peak current/single channel conductance). Event analysis reveals three peaks between 0 and 140ps. These peaks are separated by ~39pS indicating single channel conductance of 39.0pS in INX6 based gap junctions (Fig. 6H).

±70mV

There are two states visible in the representative current recording associated with a voltage pulse of ±70mV (Fig. 6L). Peaks of 42pS and 76pS are well fit in the all points histogram and indicate two channels present in the system. Similar peaks can be seen in current recording from voltage pulses of ±30mV. This indicates that channels are not inactivating more at ±70mV than they are during voltage pulses of ±30mV. It should be noted though that only one experiment was able to resolve an open/close transition at the single channel level. This is also likely limiting our ability to resolve inactivation and single channel conductance at the single channel level for INX6 homomeric gap junctions. Event analysis histograms of voltage pulses at *±70mV* (Fig. 6P) revealed three peaks between 0 and 140pS of 38.9pS, 83.4pS, and 115.5pS. These peaks closely matched the peaks visible during voltage pulses of *±30mV* indicating that channels might already be operating at closed states thereby restricting current during a pulse of *±30mV*.

Hydra Innexin Dwell Times

Analyzing single channel events allows us to calculate amplitudes of open channels and the duration of those open channel events. We note that the INX channels do not have a linear i/V relationship, suggesting that at large voltage steps, channels are in a subconductance state(Fig. 7A-E). Calculating the duration, or dwell time, of channels in open states allows us to better understand how channels are inactivating in response to a voltage pulse.

Dwell times varied between innexins but a stark difference is apparent between Innexin 2 of the EC1/5 cluster and Innexins 6,7,10,14 of the EC3 cluster. INX2 exhibited an average open dwell time of 1319.9 mS in response to a ±30mV step and 522mS in response

to a ±70mV step (Fig. 7F). The 95% confidence interval was calculated due to outliers that skewed the standard deviation. This indicates that channels stay open longer during voltage pulses of ±30mV and more readily close during greater voltage pulses which is to be expected in voltage dependent channels.

Similarly all EC3 innexins have greater open dwell times at lower potentials than higher potentials(Fig. 7F, Table 3). However INX2 gap junctions exhibit >2X open dwell times than EC3 which reflects the larger inactivation that occurs in these channels compared to INX2(Fig. 7F, Table 3). Again, gap junction currents mediating the CB1 circuit via INX2 channels would tend to pass more current to a neighboring cell for any given stimulus or depolarization.

Heterotypic Coupling of Hydra Innexins

Lastly we asked whether Heterotypic gap junctions form in Hydra innexins. To do so, we transformed cells with PneuroD-INX-IRES-GFP or PneuroD-INX-IRES-TdTomato. After 48 hour cells were mixed and plated onto glass coverslips 2 hours before experiments. Rather than identifying adjacent cells that both expressed the same reporter we searched for adjacent cells that expressed different reporters, GFP and TdTomato. These conditions allow for the formation of heterotypic gap junctions. Experiments were then conducted using the dual whole cell voltage clamp technique while one of the cells was stepped from -80 to +80 mV in 20mV steps.

We conducted these experiments for all possible combinations of Innexins (Fig. 8A) with limited results. Heterotypic gap junctions did not readily form between N2a cells expressing hydra innexins except for one combination (INX10-INX7)(Fig. 8A). We were only able to record current from a single experiment out of 5 attempts adding to the evidence

that *Hydra* innexins do not easily form heteromeric gap junctions in n2a cells. Despite this we were able to observe characteristic voltage dependent inactivation on both sides of the channel (Fig. 8 B, C) as evidenced by the lower Iss than Ip. Notably INX10-INX7 heterotypic channels initially did not appear to exhibit rectification, a property of some connexin heterotypic channels, which would manifest as a lack of inactivation on a single side of the channel (Elenes et al., 2001; He et al., 1999; Lin et al., 2014) (Fig8 B,C).

We then proceeded to analyze voltage dependent inactivation by normalizing Iss to Ip to produce Gss-Vj plots. GJss-Vj plots with Boltzmann fits indicated that INX10-INX7 heterotypic channels did display minor rectification. Heterotypic channels inactivated to 0.39 GJss when a negative pulse was applied and displayed more inactivation during positive pulses by inactivating to 0.21 GJss; each of these is significantly greater than that for INX2 currents (Fig. 8D).

Inactivation of heteromeric channels is 0.2 GJss greater than that of homomeric INX10 channels during negative voltage pulses and 0.06Gjss smaller during positive pulses (Fig. 8F, Table 1). Heterotypic INX10-INX7channels inactivation kinetics more closely resembled those of INX7 as inactivation during negative pulses was 0.06GJss higher in heterotypic channels and nearly matched INX7 homomeric channels during positive pulses Fig. 8E, Table 1). Boltzmann fit parameters can be found in Table 1.

DISCUSSION

In this study we used the dual whole cell voltage clamp technique to characterize the electrical properties of homomeric gap junctions composed of hydra innexins expressed in the nervous system of *Hydra vulgaris.* All of the genes were previously predicted proteins

that are now confirmed to form homomeric gap junctions in mouse neuro2a blastoma cells. All INXs also exhibited characteristics similar to those of well studied connexin based gap junctions(Evans and Martin, 2002; Lin et al., 2014; Moreno, 2004; Yue et al., 2021). Though *Hydra* innexins were capable of forming gap junctions in N2a cells, we recognize that N2a cells, which do not contain innexin genes(Phelan and Starich, 2001), may not be able to properly mimic the channel properties that pertain in hydra neurons. It may be that accessory proteins or posttranslational modifications not present in N2a cells are required for normal channel activity(Axelsen et al., 2013). Glycosylation and phosphorylation are known to modulate activity of gap junctions (Moreno et al., 1994) and may be required in *Hydra* innexins to exhibit accurate conductance and inactivation. Thus while we have taken an important first step in characterizing *Hydra* innexins further studies should consider their biophysical properties within the context of *Hydra* neurons.

Inactivation of Hydra Gap Junctions

There is a notable difference between inactivation parameters of INX2 (CB1 circuit) and the innexins expressed in the EC3 cluster of the hydra single cell transcriptome(Siebert et al., 2019). The clear correlation between expression and biophysical properties leads us to hypothesize that the relatively limited inactivation seen in INX2 currents is important in CB activity. As previously proposed (Takaku et al., 2014) INX2 may coordinate and synchronize the activity of the CB circuit (Dupre and Yuste, 2017). When the CB circuit of *Hydra* is activated it does so very rapidly and fires several action potentials in quick succession. Limited inactivation ofINX2 may help to support this rapid firing in the CB circuit. If INX2 were to restrict more current across the channel due to increased

inactivation, less trans-neuronal depolarization would occur, potentially preventing action potentials in coupled cells, inhibiting synchronization and coordination of the CB circuit.

It is hypothesized that the EC3 cluster correlates with neurons of the RP1 and RP2 circuit. RP circuits are activated less frequently than the CB circuit. The greater inactivation seen within EC3 innexins and thus increased restriction of current across the channel may contribute to preventing the rapid activation of the RP circuit.

Unitary Conductance

At first glance it would appear that the single channel conductances of all *Hydra* innexins at ±30mV are greater than those at ±70mV. However our results show that this is due to channel inactivation. During larger voltage steps, channels inactivate and enter subconductance states reducing current across the channel, resulting in an increased number of events seen in the event histogram (Fig. 5,6). Furthermore, the open dwell time analysis reveals that channels spend less time in an open state at voltage steps of ±70mv than ±30mv thereby restricting current and therefore conductance. This increases the likelihood that a current record would display an open channel at a subconductance state rather than a fully open channel. Single channel amplitude noise can also affect conductance as the structure of the channel may allow for different amplitudes or the channel may enter into subconductance states that differ only slightly from the main state.

This is the first study to characterize the electrophysiological properties of hydra innexins. Innexins play an essential role in the synchronization of circuits and coordination of behaviors. The characterization of biophysical characteristics of *Hydra* innexin channels can be incorporated into modeling of Hydra circuits to evaluate their specific functional roles.

Figures

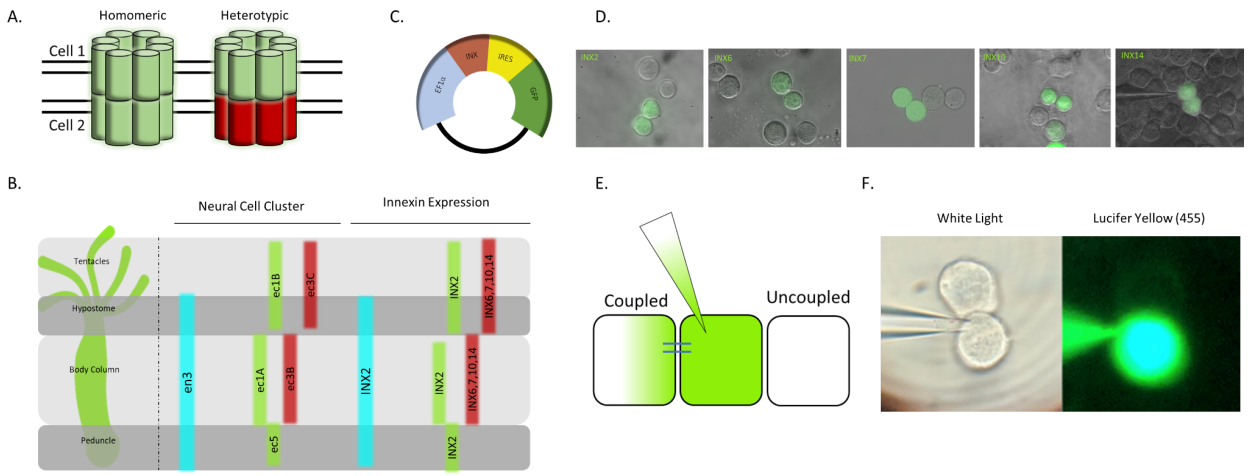

Figure 1. Background and Expression A) Homomeric and heterotypic gap junction combinations are possible between hydra cells. B) Hydra innexins exhibit diverse expression in the nervous system of hydra. The single cells transcriptome allowed us to identify the expression of innexins in neural cell types which correlated with the different circuits of the animal. INX 6,7,10,14 are expressed in the EC3B anc EC3C clusters. INX2 is expressed in EC1A, EC1B, EC5 and EN3 clusters. C) modified pneuroD plasmid is used to drive expression of innexins and a reporter gene. D) Neuro2a cells expressing hydra innexins and GFP. From left to right: INX2, INX6, INX7, INX10, INX14. E) Cartoon describing lucifer yellow injection experiment. F) When lucifer yellow is injected into wild-type n2a cells, the dye does is not transferred to adjacent cells indicating they are not intrinsically coupled.

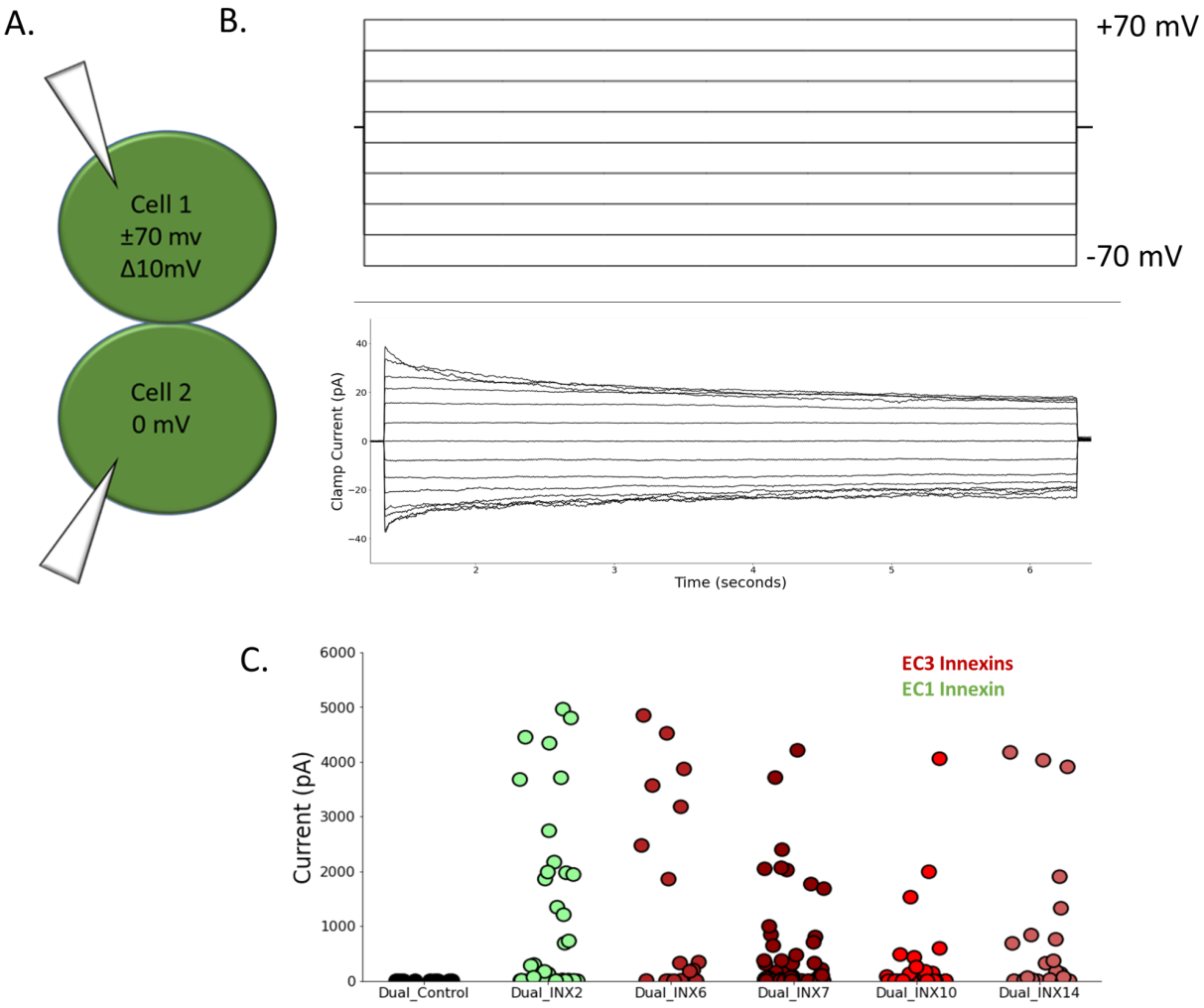

Figure 2. Homomeric coupling of hydra innexins. A) Cartoon schematic representing INX/GFP expressing cells and dual whole cell voltage clamp. B) Cells are initially clamped at 0mV and one of the cells is stepped from -70 to +70mV in 10mV steps. Current is measured in both cells with current changes in cell 2 indicating coupling between cells via innexin gap junctions. B) All hydra innexins expressed in the nervous system were successfully able to form homomeric gap junctions. Each point on the graph represents the average current measured across the voltage pulse for that experiment. Note that not all every experiment elicited a current response possibly due to low expression of hydra innexin in n2a cells.

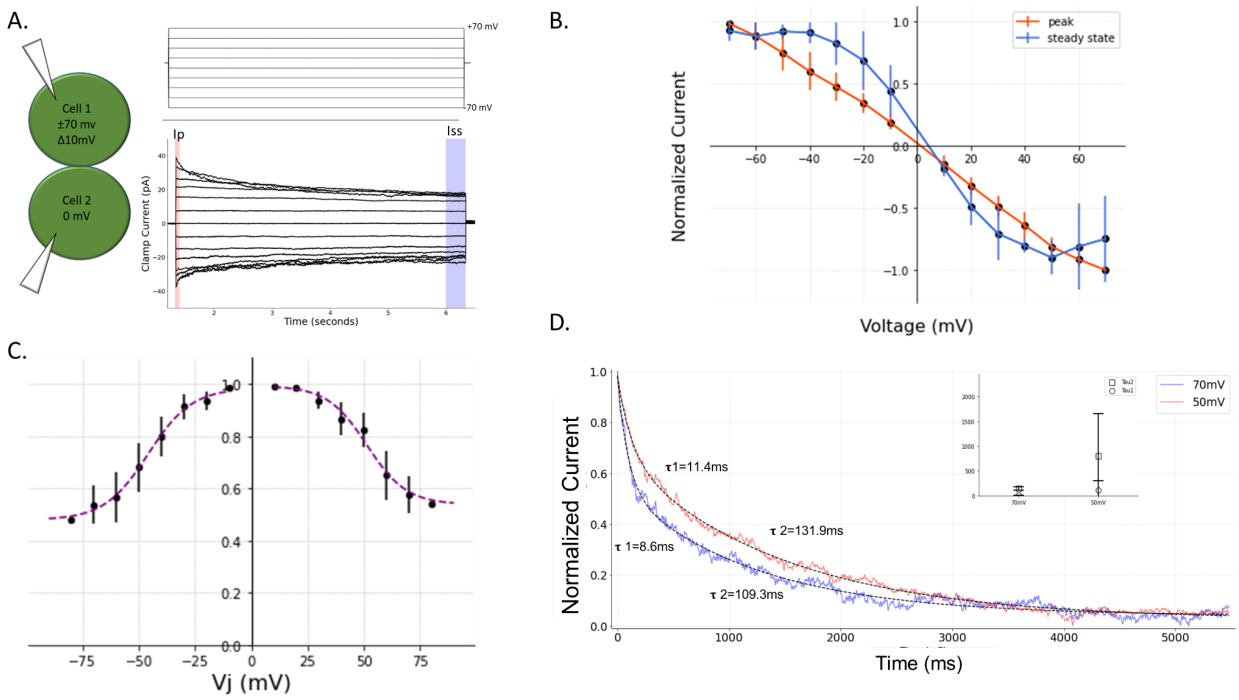

Figure 3. Innexin 2 forms homomeric gap junctions in N2a cells. A)Voltage step protocol elicits current response in cell two. Red bar indicates Instantaneous current (Ip), blue bars represent steady state current (Iss). Inactivation from the Ip to the Iss can be seen at larger voltages potentials in INX2 homomeric gap junctions. B) Differing Current Voltage (I/V) relationships are visible in the Ip and Iss components of current recordings. Iss I/V is non-linear compared in Ip. C) normalized steady state conductance (nGJss) is plotted over voltage and fit to a Boltzmann equation. Iss of INX2 homomeric gap junction inactivates to 50%% of the Ip at greater voltages. D) Current recordings from voltages of ±70mV and ±50mV are fit to a two term exponential equation to calculate the time constants (**τ**1, **τ**2) of INX2 homomeric gap junctions. Current inactivation contains a fast and slow component.

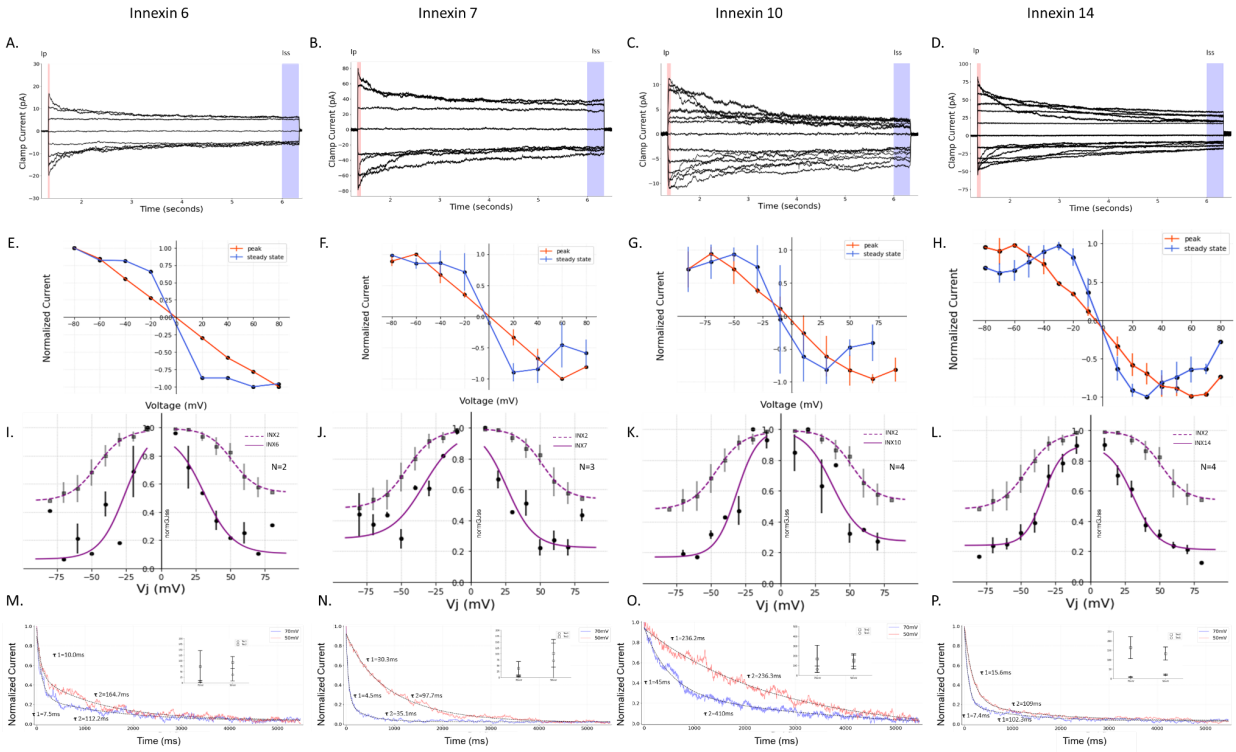

Figure 4. Voltage Dependent Inactivation of EC3 Hydra Innexins. A)-D). Current Recordings from INX6,7,10,14. All homomeric gap junctions undergo voltage dependent inactivation visible by decrease from Ip (red bar) to Iss(blue bar). E)-H) I/V relationships of hydra innexins. Ip maintains some linearity in the amount of current recorded in response to voltage response. However Iss is clearly non-linear suggesting voltage dependent inactivation. I)-L) normGJss plotted over voltage. All EC3 innexins inactivate to a greater degree than INX2. M)-P) Time constants associated with inactivation in hydra innexins. Current records from ±70mV and ±50mV voltage pulses are fit to a two-term exponential equation to identify slow and fast components of inactivation.

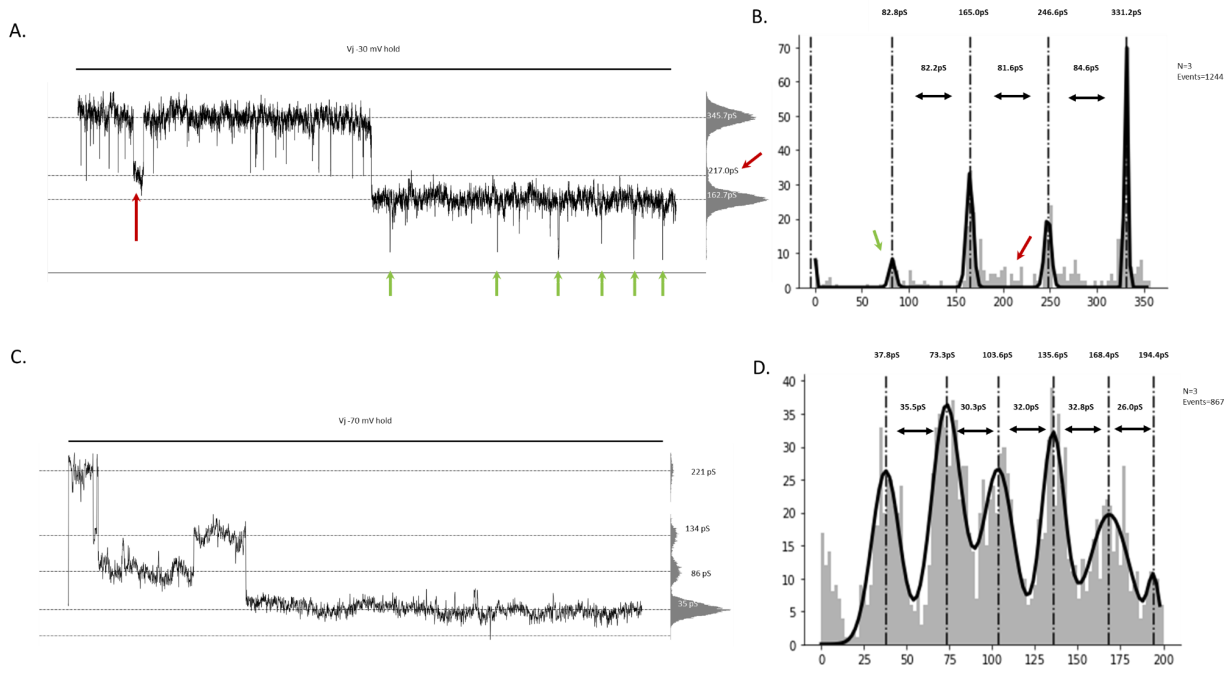

Figure 5. Unitary Conductance of INX2 Homomeric Gap Junctions. A) Current recording during a -30mV voltage pulse. All points histogram fit with Gaussian equation fits to conductance values of 345pS, 217pS, and 162.7pS. Red arrow indicates a subconductance transition of 217pS. Green arrows indicate transitions to subconductance state of 82pS. B) Event histogram representing events from three experiments including 1244 events. Event histogram is fit with Gaussian equation which reveals four peaks. Sub conductance states are represented by smaller peaks of 82.8 and 246.6pS. Full openings are represented by 165 and 331.2pS. Green and red arrows correspond to events from current record in A. C) Current recording during a -70mV voltage pulse. Four peaks are visible in the allpoints histogram to the right of the recording with peaks of 35pS, 86pS, 134pS and 221pS. Increased number of transitions reflects inactivation seen at the macroscopic level. D) Event histogram representing events from three experiments including 867 events. Six peaks are visible between 0 and 200pS.

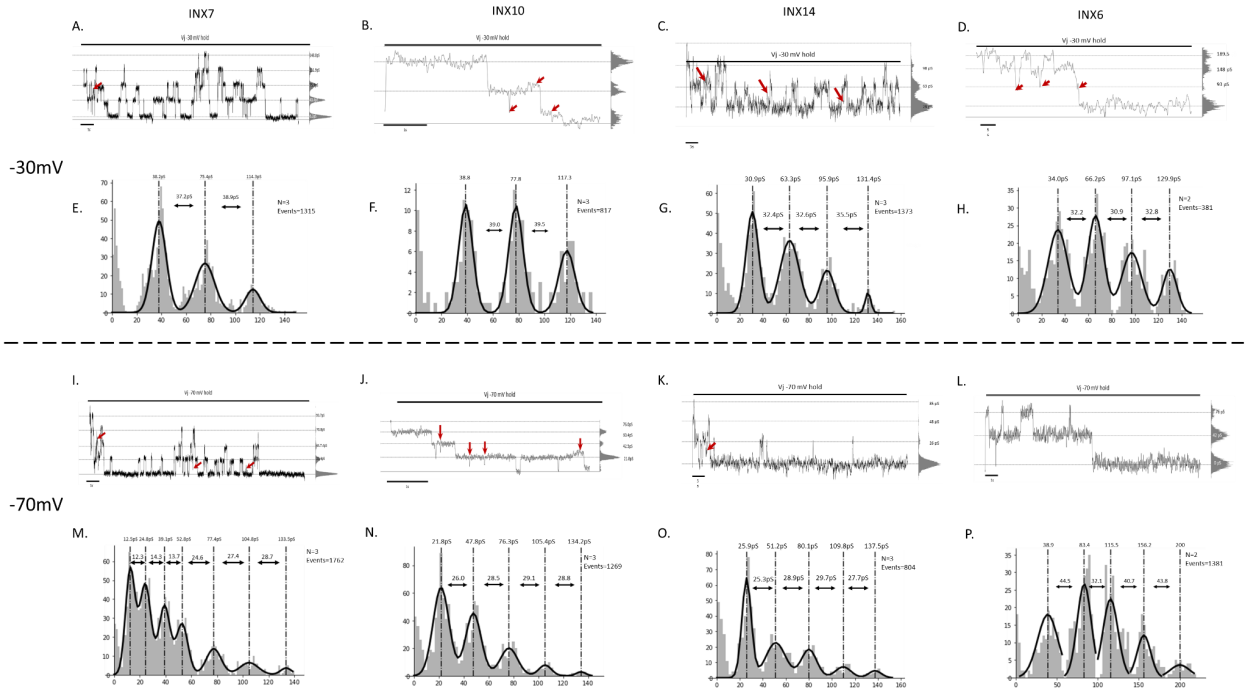

Figure 6. Unitary Conductance of Homomeric Gap Junctions composed of EC3 Cluster Innexins. A)-D)) Current recording during a -30mV voltage pulse. States are well fit in the all-point histogram seen to the right of each recording. Red arrows indicate subconductance states (current does not sum to full open channels) E)-F) Event histograms compiled from current records during voltage pulse of -30mV. Each histogram includes multiple experiments (N) and extensive events (Events). I)-L) Representative current records during a -70mV voltage pulse for each of the EC3 Innexins. States are well fit in the all-point histogram seen to the right of each recording. Red arrows indicate short subconductance events present within the current record. Greater number of states are visible during -70mV pulses further indicating current inactivation at the macroscopic and single channel level. M)-P). Event histograms compiled from current records during voltage pulse of -70mV for each of the EC3 Innexins.

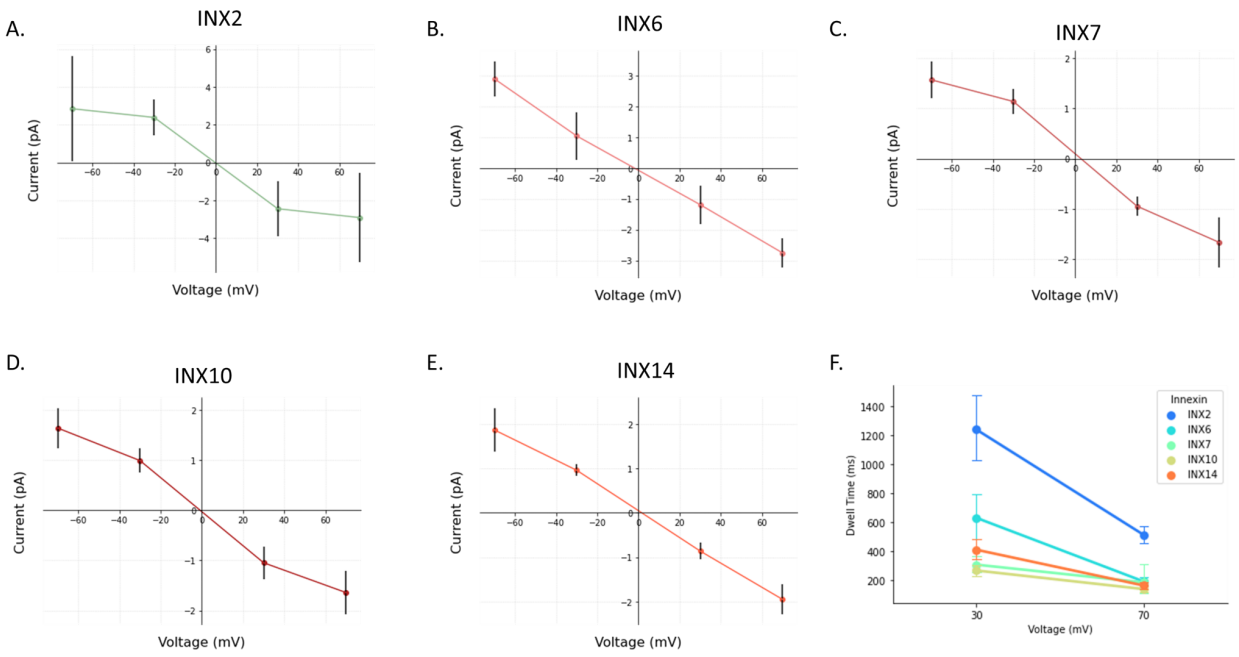

Figure 7. Single Channel IV and Dwell Times of Hydra Innexins. A)-E) I/V relationship is non-linear at the single channel level for all hydra innexins further suggesting channels inactivate as a response to greater voltage potentials. F) Open state dwell times for all Hydra Innexins. Open state dwell times are consistently longer at ±30mV than ±70mV indicating that greater voltages induce closing events in hydra innexins.

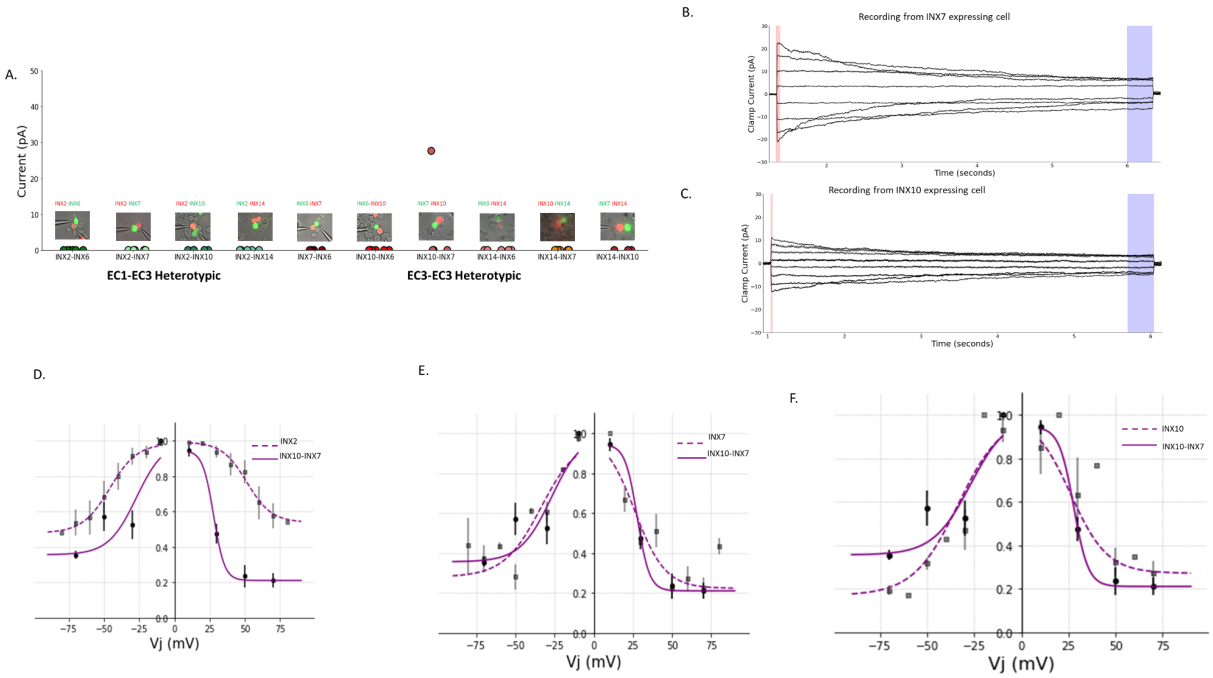

Figure 8. Heterotypic coupling of hydra innexins. A) Point plot indicating average current across a voltage pulse for heterotypic gap junctions. Pictures demonstrate different hydra innexins expressed in N2a cells, GFP or RFP. Only INX10 in combination with INX7 successfully created heterotypic gap junctions in a single dual whole cell voltage clamp experiment. B) Current recording from the N2a cell expressing INX7 C) Current recording from cell expressing INX10 D) normalized steady state conductance (nGJss) is plotted over voltage and fit to a Boltzmann equation. Heterotypic INX10-INX7 inactivates to a greater extent than INX2. E) Heterotypic INX10-INX7 inactivation relative to homomeric INX7. F) Heterotypic INX10-INX7 inactivation relative to homomeric INX10

Table 1

Boltzmann fitting parameters for the voltage inactivation of hydra innexins

Innexin	Gmin (-V)	Gmin (+V)	Vhalf (-V)	Vhalf (+V)	A (-V)	A (+V)
INX2	0.51	0.46	-45.8	51.4	-0.1	0.11
INX6	0.07	0.1	-25.7	31.2	-0.1	0.1
INX7	0.33	0.23	-33.1	25.9	-0.1	0.1
INX10	0.19	0.27	-32	40.1	-0.13	0.1
INX14	0.17	0.13	-36.3	34.7	-0.11	0.09
INX10-INX7	0.39	0.21	-24.8	28.9	-0.22	0.21

Table 2

Inactivation Time Constants for Hydra Innexins

Innexin	70mV τ1 (mS)	70mV τ2 (mS)	70mV τ1 std	70mV τ2 std	50mV τ1 (mS)	50mV τ2 (mS)	50mV τ1 std	50mV τ2 std
INX2	**9.1**	**144.5**	**2.5**	**29.1**	**105.3**	**799.9**	**199.2**	**859.0**
INX6	**18.5**	**76.3**	**16.8**	**55.7**	**53.5**	**173.5**	**65.9**	**196.7**
INX7	**3.4**	**38.9**	**1.5**	**28.5**	**71.0**	**102.3**	**73.9**	**58.6**
INX10	**61.2**	**168.1**	**33.2**	**139.5**	**136.5**	**156.3**	**70.9**	**64.9**
INX14	**7.4**	**163.6**	**2.3**	**57.8**	**19.2**	**132.6**	**3.0**	**34.8**

Table 3

Dwell Time Statistics for Hydra Innexins

Innexin	30mV Dwell TIme (ms)	95% CI LL	95% CI UL	70mV Dwell TIme (ms)	95% CI LL2	95% CI UL3
INX2	1319.9	1101.6	1558.4	522.6	476.5	571.3
INX6	652.7	534.2	782.6	209.5	188.6	235.7
INX7	283.8	260.6	308.5	195.5	162.2	236.6
INX10	367.9	324.9	412.1	188.2	168	208.7
INX14	392.8	354.6	432.2	188.4	164.9	213.1

REFERENCES

Adams MD, Celniker SE, Holt RA, Evans CA, Gocayne JD, Amanatides PG, Scherer SE, Li PW, Hoskins RA, Galle RF, George RA, Lewis SE, Richards S, Ashburner M, Henderson SN, Sutton GG, Wortman JR, Yandell MD, Zhang Q, Chen LX, Brandon RC, Rogers Y-HC, Blazej RG, Champe M, Pfeiffer BD, Wan KH, Doyle C, Baxter EG, Helt G, Nelson CR, Gabor GL, Miklos, Abril JF, Agbayani A, An H-J, Andrews-Pfannkoch C, Baldwin D, Ballew RM, Basu A, Baxendale J, Bayraktaroglu L, Beasley EM, Beeson KY, Benos PV, Berman BP, Bhandari D, Bolshakov S, Borkova D, Botchan MR, Bouck J, Brokstein P, Brottier P, Burtis KC, Busam DA, Butler H, Cadieu E, Center A, Chandra I, Cherry JM, Cawley S, Dahlke C, Davenport LB, Davies P, Pablos B de, Delcher A, Deng Z, Mays AD, Dew I, Dietz SM, Dodson K, Doup LE, Downes M, Dugan-Rocha S, Dunkov BC, Dunn P, Durbin KJ, Evangelista CC, Ferraz C, Ferriera S, Fleischmann W, Fosler C, Gabrielian AE, Garg NS, Gelbart WM, Glasser K, Glodek A, Gong F, Gorrell JH, Gu Z, Guan P, Harris M, Harris NL, Harvey D, Heiman TJ, Hernandez JR, Houck J, Hostin D, Houston KA, Howland TJ, Wei M-H, Ibegwam C, Jalali M, Kalush F, Karpen GH, Ke Z, Kennison JA, Ketchum KA, Kimmel BE, Kodira CD, Kraft C, Kravitz S, Kulp D, Lai Z, Lasko P, Lei Y, Levitsky AA, Li J, Li Z, Liang Y, Lin X, Liu X, Mattei B, McIntosh TC, McLeod MP, McPherson D, Merkulov G, Milshina NV, Mobarry C, Morris J, Moshrefi A, Mount SM, Moy M, Murphy B, Murphy L, Muzny DM, Nelson DL, Nelson DR, Nelson KA, Nixon K, Nusskern DR, Pacleb JM, Palazzolo M, Pittman GS, Pan S, Pollard J, Puri V, Reese MG, Reinert K, Remington K, Saunders RDC, Scheeler F, Shen H, Shue BC, Sidén-Kiamos I, Simpson M, Skupski MP, Smith T, Spier E, Spradling AC, Stapleton M, Strong R, Sun E,

Svirskas R, Tector C, Turner R, Venter E, Wang AH, Wang X, Wang Z-Y, Wassarman DA, Weinstock GM, Weissenbach J, Williams SM, Woodage T, Worley KC, Wu D, Yang S, Yao QA, Ye J, Yeh R-F, Zaveri JS, Zhan M, Zhang G, Zhao Q, Zheng L, Zheng XH, Zhong FN, Zhong W, Zhou X, Zhu S, Zhu X, Smith HO, Gibbs RA, Myers EW, Rubin GM, Venter JC. 2000. The Genome Sequence of *Drosophila melanogaster*. *Science* **287**:2185–2195. doi:10.1126/science.287.5461.2185

Axelsen LN, Calloe K, Holstein-Rathlou N-H, Nielsen MS. 2013. Managing the complexity of communication: regulation of gap junctions by post-translational modification. *Front Pharmacol* **4**. doi:10.3389/fphar.2013.00130

Bennett MVL, Zukin RS. 2004. Electrical Coupling and Neuronal Synchronization in the Mammalian Brain. *Neuron* **41**:495–511. doi:10.1016/S0896-6273(04)00043-1

Chapman JA, Kirkness EF, Simakov O, Hampson SE, Mitros T, Weinmaier T, Rattei T, Balasubramanian PG, Borman J, Busam D, Disbennett K, Pfannkoch C, Sumin N, Sutton GG, Viswanathan LD, Walenz B, Goodstein DM, Hellsten U, Kawashima T, Prochnik SE, Putnam NH, Shu S, Blumberg B, Dana CE, Gee L, Kibler DF, Law L, Lindgens D, Martinez DE, Peng J, Wigge PA, Bertulat B, Guder C, Nakamura Y, Ozbek S, Watanabe H, Khalturin K, Hemmrich G, Franke A, Augustin R, Fraune S, Hayakawa E, Hayakawa S, Hirose M, Hwang JS, Ikeo K, Nishimiya-Fujisawa C, Ogura A, Takahashi T, Steinmetz PRH, Zhang X, Aufschnaiter R, Eder M-K, Gorny A-K, Salvenmoser W, Heimberg AM, Wheeler BM, Peterson KJ, Böttger A, Tischler P, Wolf A, Gojobori T, Remington KA, Strausberg RL, Venter JC, Technau U, Hobmayer B, Bosch TCG, Holstein TW, Fujisawa T, Bode HR, David CN, Rokhsar DS, Steele RE.

2010. The dynamic genome of Hydra. *Nature* **464**:592–596. doi:10.1038/nature08830

Chou VT, Johnson SA, Van Vactor D. 2020. Synapse development and maturation at the drosophila neuromuscular junction. *Neural Develop* **15**:11. doi:10.1186/s13064-020-00147-5

Dupre C, Yuste R. 2017. Non-overlapping Neural Networks in Hydra vulgaris. *Curr Biol* **27**:1085–1097. doi:10.1016/j.cub.2017.02.049

Elenes S, Martinez AD, Delmar M, Beyer EC, Moreno AP. 2001. Heterotypic Docking of Cx43 and Cx45 Connexons Blocks Fast Voltage Gating of Cx43. *Biophys J* **81**:1406–1418. doi:10.1016/S0006-3495(01)75796-7

Evans WH, Martin PEM. 2002. Gap junctions: structure and function (Review). *Mol Membr Biol* **19**:121–136. doi:10.1080/09687680210139839

Guerrier S, Coutinho-Budd J, Sassa T, Gresset A, Jordan NV, Chen K, Jin W-L, Frost A, Polleux F. 2009. The F-BAR Domain of srGAP2 Induces Membrane Protrusions Required for Neuronal Migration and Morphogenesis. *Cell* **138**:990–1004. doi:10.1016/j.cell.2009.06.047

He DS, Jiang JX, Taffet SM, Burt JM. 1999. Formation of heteromeric gap junction channels by connexins 40 and 43 in vascular smooth muscle cells. *Proc Natl Acad Sci* **96**:6495–6500. doi:10.1073/pnas.96.11.6495

Hillier LW, Marth GT, Quinlan AR, Dooling D, Fewell G, Barnett D, Fox P, Glasscock JI, Hickenbotham M, Huang W, Magrini VJ, Richt RJ, Sander SN, Stewart DA, Stromberg

M, Tsung EF, Wylie T, Schedl T, Wilson RK, Mardis ER. 2008. Whole-genome sequencing and variant discovery in C. elegans. *Nat Methods* **5**:183–188. doi:10.1038/nmeth.1179

Landesman Y. n.d. Innexin-3 forms connexin-like intercellular channels 6.

Leclère L, Horin C, Chevalier S, Lapébie P, Dru P, Peron S, Jager M, Condamine T, Pottin K, Romano S, Steger J, Sinigaglia C, Barreau C, Quiroga Artigas G, Ruggiero A, Fourrage C, Kraus JEM, Poulain J, Aury J-M, Wincker P, Quéinnec E, Technau U, Manuel M, Momose T, Houliston E, Copley RR. 2019. The genome of the jellyfish Clytia hemisphaerica and the evolution of the cnidarian life-cycle. *Nat Ecol Evol* **3**:801–810. doi:10.1038/s41559-019-0833-2

Li H, Avery L, Denk W, Hess GP. 1997. Identification of chemical synapses in the pharynx of Caenorhabditis elegans. *Proc Natl Acad Sci* **94**:5912–5916. doi:10.1073/pnas.94.11.5912

Lin X, Xu Q, Veenstra RD. 2014. Functional formation of heterotypic gap junction channels by connexins-40 and -43. *Channels* **8**:433–443. doi:10.4161/19336950.2014.949188

Moreno A. 2004. Biophysical properties of homomeric and heteromultimeric channels formed by cardiac connexins. *Cardiovasc Res* **62**:276–286. doi:10.1016/j.cardiores.2004.03.003

Moreno AP, Sáez JC, Fishman GI, Spray DC. 1994. Human connexin43 gap junction channels. Regulation of unitary conductances by phosphorylation. *Circ Res* **74**:1050–1057.

doi:10.1161/01.RES.74.6.1050

Pereda AE. 2014. Electrical synapses and their functional interactions with chemical synapses. *Nat Rev Neurosci* **15**:250–263. doi:10.1038/nrn3708

Phelan P, Starich TA. 2001. Innexins get into the gap. *BioEssays* **23**:388–396. doi:10.1002/bies.1057

Phelan P, Stebbings LA, Baines RA, Bacon JP, Davies JA, Ford C. 1998. Drosophila Shaking-B protein forms gap junctions in paired Xenopus oocytes. *Nature* **391**:181–184. doi:10.1038/34426

Ramanan SV, Brink PR. 1993. Multichannel recordings from membranes which contain gap junctions. II. Substates and conductance shifts. *Biophys J* **65**:1387–1395. doi:10.1016/S0006-3495(93)81193-7

Rybak J, Talarico G, Ruiz S, Arnold C, Cantera R, Hansson BS. 2016. Synaptic circuitry of identified neurons in the antennal lobe of *Drosophila melanogaster*: Synaptic Circuits of *Drosophila* Antennal Lobe. *J Comp Neurol* **524**:1920–1956. doi:10.1002/cne.23966

Santos-Miranda A, Noureldin M, Bai D. 2019. Effects of temperature on transjunctional voltage-dependent gating kinetics in Cx45 and Cx40 gap junction channels. *J Mol Cell Cardiol* **127**:185–193. doi:10.1016/j.yjmcc.2018.12.014

Siebert S, Farrell JA, Cazet JF, Abeykoon Y, Primack AS, Schnitzler CE, Juliano CE. 2019. Stem cell differentiation trajectories in *Hydra* resolved at single-cell resolution. *Science* **365**:eaav9314. doi:10.1126/science.aav9314

Stark WS, Sapp R, Carlson SD. 1989. Ultrastructure of the Ocellar Visual System in Normal and Mutant *Drosophila Melanogaster*. *J Neurogenet* **5**:127–153. doi:10.3109/01677068909066203

Takaku Y, Hwang JS, Wolf A, Böttger A, Shimizu H, David CN, Gojobori T. 2014. Innexin gap junctions in nerve cells coordinate spontaneous contractile behavior in Hydra polyps. *Sci Rep* **4**:3573. doi:10.1038/srep03573

Welzel G, Schuster S. 2022. Connexins evolved after early chordates lost innexin diversity. *eLife* **11**:e74422. doi:10.7554/eLife.74422

Yue B, Haddad BG, Khan U, Chen H, Atalla M, Zhang Z, Zuckerman DM, Reichow SL, Bai D. 2021. Connexin 46 and connexin 50 gap junction channel properties are shaped by structural and dynamic features of their N-terminal domains. *J Physiol* **599**:3313–3335. doi:10.1113/JP281339

CHAPTER 3: A BIOMECHANICAL MODEL OF HYDRA MOVEMENT

Manuscript Contribution

A Biomechanical Model of Hydra Movement was a collaboration between the Bosma and Fairhall labs conducted primarily by the graduate students Hengji Wang of the Fairhall lab, and Josh Swore of the Bosma lab.

Joshua Swore was in charge of animal husbandry during the study which included feeding, cleaning, and preparation of animals for experiments. More than 100 videos were recorded for experiments that included extensive imaging of 30 minutes to 2 hours using the zeiss axioscope provided by the Rasmussen Lab. Videos then required processing which was conducted by Joshua Swore and Analysis, which was split between Joshua and Hengji. While Hengji provided extensive python scripts for analysis Joshua used the Icy imaging software to extract animal contours for all videos. Josh Swore and Hengji worked together to track the following four body points on the animal: Hypostome, Armpit 1(Intersection between right side bottom most tentacle and bodycollumn), Armpit 2 (Intersection between right side bottom most tentacle and bodycollumn), and the peduncle. The coordinates from the tracked points and contours were used to calculate the midline of the animal; this work was also split between Hengji Wang and Josh Swore.

Through the empirical study, conducted by Joshua Swore and computational modeling skills of Hengji Wang the following manuscript was prepared.

Introduction

Anatomy and behaviors of *Hydra*.

Hydra has a relatively simple anatomy. Its fluid-filled body column consists of two body layers, the ectodermal and endodermal epithelia, separated and supported by an acellular gelatinous layer, the mesoglea, Fig. 1. The epithelial layers consist of a sheet of epitheliomuscular cells, innervated by separate nerve nets. The ectodermal and endodermal epitheliomuscular cells respectively produce longitudinal and circumferentially oriented contractions (11). These layers, together with the enclosed fluid, form a hydrostatic skeleton in which the force of muscle contraction is transmitted throughout the body column by internal pressure
(12).

Movement in *Hydra* is controlled by a diffuse nerve net. *Hydra* has one of the earliest and simplest nervous system (13, while its uncoupled ectodermal and endodermal nerve nets (15) lack a centralized “brain” or ganglia, their firing activity underlies a rich repertoire of behaviors. These include contraction bursts, active elongation, nodding, bending and two forms of locomotion (9, 16–20). However, how neural activity drives behavior is not understood. Early extracellular recordings identified several distinct electrical events in *Hydra*: contraction bursts (CB), rhythmic potentials (RP) and prelocomotion bursts (PLB)

(18, 19, 21, 22). Recent work has clearly identified three separate functional nerve subnetworks responsible for these electrical events (8). However, only one of these, the contraction burst (CB) network, is directly correlated with a motor output, namely whole-body contraction (8). What causes the CB nerve net to fire is still not known, although it is influenced by environmental conditions including osmolarity (23) and temperature, (24) as well as microbes (25). Aside from the CB, the precise association of neural activity with behavior has not yet been mapped out.

Neural control of behavior in *Hydra*.

At what length scale and with what precision does the firing of nerve cells influence movement? These factors depend on how activation is conveyed through muscles, and how the resulting network of muscular contractions interacts with the biomechanics of the body. Due to gap junctional coupling (26), the epitheliomuscular network is able to propagate excitation (27–29) even when *Hydra*'s nerve cells have been removed (30, 31). Several studies have suggested that contraction pulses can be conducted by the epithelium in *Hydra* (27, 28, 32–34); conduction in nerve-free epithelia has also been demonstrated in other hydrozoans such as Siphonophores, *Sarsia* and *Euphysa* (35, 36). By imaging calcium signals in the endo- and ectodermal epithelial layers, (9) reported two distinct forms of muscle layer activation: a rapid global activation that drives whole-body contraction (contraction pulse), and slow waves of local activation that initiate anywhere at the body column (body column wave) or initiate at a region of the peduncle and correlate with bending (bending wave). This suggests that the dynamics of the muscle layer itself form an important and nontrivial component of the transformation from nerve firing to behavior. Here, we construct a model of *Hydra* that includes sufficient biophysical and biomechanical

detail to simulate the complete transformation from neural activity to muscle activity to behavior. We aimed to address the following specific questions: (i) What are the mechanisms that support the observed dual timescales of muscle activation, and how does *Hydra* use these different dynamics in behavior? (ii) During contraction bursts, although only neurons in the ectodermal nerve net fire (8), both muscle layers are activated (9), and thus work against one another. What explains this dual-layer activation and how can body contraction be achieved with opposing muscle drive? (iii) Can we quantitatively reproduce basic behaviors (20), including contraction, elongation and bending?

To answer these questions, we implemented a multi-layered model (Fig. 2), transforming neural activity to movement. Our models are constrained both by observations from calcium imaging and by the use of physiologically plausible mechanisms consistent with the recently developed RNAseq database (37). To model calcium dynamics in the epitheliomuscular cell network, we postulate the coexistence of a fast cellular electrically mediated pathway and a slow IP_3-driven pathway. We assume that these activation signals are transmitted through the epithelial layers by gap junctions (38–40). These two mechanisms permit the coexistence of the fast electrically driven contractions as well as slow waves responsible for bending; the model predicts that these dynamics are triggered by distinct signals. We show that an intermediate level of gap junctional coupling between the ecto- and the endodermal epithelium can share contraction activation between the two muscle layers, but isolate slow wave activity to the ectoderm, consistent with observation. We next convert calcium dynamics to force generation. In order to account for *Hydra*'s movement dynamics, it was necessary to hypothesize that the relationship between calcium and force has more persistent dynamics in the endoderm than in the ectoderm,

essentially suggesting slower relaxation times for endodermal muscles. Finally, we convert the simulated epithelial calcium dynamics to strain, which provides an active force input into a biomechanical model of the fluid-filled hydrostat. To our knowledge, such an actuated biological hydrostat has not been previously modeled. We use this model to show that the simulated muscle activation, when driven by neural activity inferred from calcium imaging, can account quantitatively for the measured behaviors of contraction, elongation and bending.

Materials and Methods

We build our biophysical model (dynamics of calcium and stress) with Python 3. Differential equations in our model are solved using the Euler stepping method. The biomechanical model is constructed on COMSOL Multiphysics® 5.3a. All code and relevant data are available at https://github.com/hengjiwang/hydramuscle.

Single cell model. The differential equations that describe the calcium dynamics in a single cell are shown in Eq. 1 where C is the cytosolic Ca2+ concentration; S is the ER Ca2+ concentration; P is the cytosolic IP3 concentration; V is the membrane potential. Detailed expressions of terms and equilibrium conditions are included in the Supplementary Information text; the corresponding parameters can be found in Table S1. Multicellular model. To simulate calcium signaling in the whole-body muscle sheets, we construct ectodermal and endodermal networks of Hydra epitheliomuscular cells. The number of muscle cells of Hydra varies considerably with body size (24). For a representative Hydra of length of 1.38 mm, we counted 62 cells longitudinally and 30 (15×2)-34 (17×2) cells circumferentially, depending on the longitudinal location. We approximate the body

column as a cylinder composed of 30x60 square cells, of which the side length is 30 μm; the lateral sheet edges are connected and the topmost and bottommost cell rows are taken to be isolated from the environment. Cells within a layer are connected to their neighbors via gap junctions. Each cell is treated as a compartment. To model the role of gap junctions in propagating electrical signals and diffusing IP3, neighboring cells within a layer and the cells at the same location in the endoderm and ectoderm are connected by coupling terms (Eq. 1). While all neighboring cells within a layer are coupled, cells with the same indices in the two layers are connected probabilistically, with a defined connection density as the ratio. The sensitivity analysis showing how parameters affect the wave propagation is included in the Supplementary Information text and figures: Fig. S3 shows the effects of stimulation strength, Fig. S4 shows the effects of coupling coefficients, Fig. S5 shows the effects of some intracellular parameters.

Force generation.

We applied Hai-Murphy model (78) in transforming calcium concentration to force, described by Eq. 2. where M, M p, AM p and AM represent the ratios of four possible states of the myoneme, correspondingly are unattached and unphosphorylated (M), unattached and phosphorylated (M p), attached and phosphorylated (AM p), unattached and phosphorylated (AM). The final active stress Fa = KF (AM p + AM). The difference between ectoderm and endoderm are reflected by different parameters of the Hai-Murphy model, primarily represented by the difference of k7, which is the detachment rate of the "latch-bridge" state of myoneme: its value for endoderm (tonic muscle) is much larger than that for ectoderm (phasic muscle), therefore the endoderm can maintain the contraction for a longer time than the ectoderm; also, k1 of the endoderm is more sensitive to calcium

concentration than that of the ectoderm, so endoderm is easily to be activated. Values of these parameters can be found in Supplementary Information Table S2. The matching between the length change of the model and real Hydra body in Fig. 9F is primarily achieved by tuning these Hai-Murphy model parameters

Biomechanics.

We build our biomechanical model on COMSOL Multiphysics® 5.3a, based on finite-element method. To define the passive properties of Hydra body, we define the body shell of our model as an incompressible hyperelastic material which follows a Neo-Hookean model (85). Hyperelastic materials exhibit a nonlinear stress-strain behavior and can respond elastically under very large strains (86). Muscle tissues are often well-described (87–89) and modeled (90–92) using hyperelastic properties. The passive biomechanical properties were mostly modeled based on Hill's three element model (93). Since biological soft tissues have hyperplasticity or viscoelasticity (94), we use hyperelastic material parameters to model the Hydra muscle shell and further incorporated viscoelasticity by including a Kelvin-Voigt model into the body shell material. For the enclosed fluid, we use the COMSOL simulation environment's preset material "Water", with a moving mesh. The elastic modulus and viscosity are set based on previous experimental measurements (105). The interaction between the body shell and enclosed fluid is simulated by the Fluid-Structure Interaction (FSI) module of COMSOL. To join the biophysical model and COMSOL-based biomechanical model, we use the LiveLinkTM for MATLAB® extension of COMSOL: we save the Python simulation results of stress into .csv files, then on MATLAB we load them and call API of the LiveLink to apply the stress on the biomechanical model built on COMSOL, then on COMSOL we run biomechanical simulation.

Parameters used to setup COMSOL model is shown in the Supplementary Information Table S3; configurations for the COMSOL solver are shown in Table S4. Sensitivity analysis showing how some parameters affect the length change of the biomechanical model during the simulation is shown in Fig. S6.

Model constraints: gene-expression database.

To validate choices of biophysical mechanisms including channels, receptors and pumps, we queried gene expression information for proposed components. We identified candidate genes by FASTA using the NCBI protein database and then used BLAST (106) to search for these genes in the databases Hydra 2.0 genome, Augustus Gene Models and Juliano aepLRv2. The Broad Hydra Single-Cell Portal (37) further allowed us to identify body regions with corresponding gene expression. We limited ourselves to mechanisms that were consistent with these data bases.

Fluorescence encoding.

We adopt a modified SBM model from (107) to simulate fluorescence traces from [Ca2+]i, in which GCaMP6s has five different binding states depending on how many Ca2+ ions are binding, and the fluorescence can be produced by all binding states in different extents. Data for fluorescence encoding is independent of our neuromechanical modeling and single-cellular data is absent to accurate data to fit the model. Because of this, we roughly tuned the parameters to produce some qualitatively reasonable traces for comparison.

Hydra cultures and imaging.

All Hydra lines were maintained at 18℃ and fed newly hatched *Artemia nauplii* two to three times per week. Hydra expressing the calcium indicator GCaMP6 in the ectoderm

of the animal were used for imaging experiments. We used a modified imaging preparation from (8). All imaging took place under a ZEISS Axio Zoom.V16 equipped with Zeiss AxioCam 506 monochrome camera for fluorescent imaging, PlanNeoFluar Z 2.3X objective lens and a GFP fluorescent filter set. The imaging arena consisted of a microscope slide, 50 to 100 μm spacer and a cover slip. The use of the spacer allowed us to keep the animals in focus by preventing motion in the z direction while still allowing free motion in the x and y directions. Animals were recorded in the arena for 30-60 minutes at a sampling rate of 4 to 10 frames per second.

Video analysis.

Here we use image analysis to estimate integrated fluorescence in the neuronal and muscle GCAMP lines (in contrast to single neuron tracking (108)) as well as to accurately characterize Hydra's body configuration. Acquired movies were processed using a combination of ImageJ (109), the Icy Imaging software suite (110), DeepLabCut (111) and custom scripts, with a pipeline shown in Fig. 11. ImageJ was used to adjust the contrast from background noise which is essential to accurately extract contours of the Hydra. Noise was reduced using median filtering (despeckle plugin). Icy Imaging was then used to extract the contours of individual frames using the Active Contours plugin. We can then integrate fluorescence signals within the contour. We then used DeepLabCut to track 4 reasonably well-identified body locations: the center of the hypostome, the center of the peduncle, and the points of intersection of the left- and rightmost tentacles with the body column (the "armpits"). The tracked "armpits" from DeepLabCut were used to exclude the tentacles from the Icy contour. We then used the peduncle to bisect the contour, and proportionally segment the two contour halves. Connecting the midpoints of the

segmentation points allowed us to extract the curved midline of the Hydra body in each frame.

Model reduction attempt.

Though all of the parameters included in our model are based on previous work and tuned in physiological ranges, the model rooted in the biophysical level inevitably includes many parameters, of which the complexity may interfere with the major ideas we want to convey. Therefore, we attempt to reduce the dimensionality of our model using Green's function method, which can represent the general spatiotemporal pattern as an impulse response. Detailed work is shown in the Supplementary Information text, Fig. S7, Fig. S8 and Table S5.

Results

Single cell dynamics.

We first show how the muscle system can exhibit two activation patterns with distinct time scales. The mechanisms of muscle activation are rooted in the biophysics of the single muscle cells and their interactions; thus we begin by modeling the intracellular dynamics of a single *Hydra* muscle cell.

Hydra's epitheliomuscular cells (11) have no striation (44) and are similar in structure to smooth muscle (45). The ectodermal epitheliomuscular cells display longitudinally oriented processes called myonemes which effect body contraction (11). The myonemes of the endodermal epithelium are oriented circumferentially (Fig. 2), and their contraction in principle leads to elongation via conservation of volume of the interior fluid and corresponding hydrostatic pressure (the hydrostat mechanism).

Muscle contraction is controlled by calcium dynamics, and smooth muscle has two possible sources of calcium elevation: (i) IP_3-induced Ca^{2+} release from the endoplasmic reticulum/sarcoplasmic reticulum (ER/SR) calcium store, and (ii) Ca^{2+} influx from the extracellular space through L-type/T-type calcium channels (43, 46–48). We will refer to these two calcium signaling pathways as the "slow" and "fast" pathways respectively, based on their typical time scales. Both IP_3-related calcium release (44) and electrical excitability (49) are observed in epitheliomuscular cells.

Models of smooth muscle frequently treat only one of these pathways. Models of calcium signaling in non-excitable cells may consider only the slow pathway, ignoring membrane ion channels (50–53), while others consider only the fast pathway, neglecting the dynamics of the internal calcium stores; examples include models for uterine smooth muscle (54–58), gastric smooth muscle (59), urinary bladder smooth muscle (60) and pancreatic *β*-cells (61). While some models integrate both pathways by incorporating both influx through ion channels and Ca^{2+} release from stores (38, 62, 63), modeling the two pathways separately and simulating calcium dynamics at different time scales is rare (64, 65). However, since calcium imaging in *Hydra* clearly reveals dynamics with different time scales (short-lasting and fast-propagated calcium transients in CB; long-lasting, slow calcium waves in bending and nodding (9)), we incorporate the necessary components for both slow and fast pathways in our model for *Hydra* epitheliomuscular cells, hypothesizing that the activation of them can be separately triggered by various neuropeptides. based on previous identification of distinct *Hydra* peptide functions (13) (Fig. 3A).

The simulated slow and fast dynamics are shown in Fig. 3B and Fig. 3C, respectively, and show that the timescale of the calcium dynamics triggered in slow pathway is much larger

than that in the fast pathway, consistent with the observations from calcium imaging. Ca^{2+} fluxes and ion current traces are shown in the Supplementary Information Fig. S1.

Muscle sheet dynamics.

We then extend the single cell model to a multicellular model by incorporating intercellular communication. We construct a muscle sheet (Fig. 4A) composed of 60×30 30 $\mu m\times$ 30 μm cells, as measured from an example small *Hydra* (Supplementary Information Fig. S2), with each cell modeled as described in the last subsection. While cell size may vary during contraction, for modeling simplicity we do not take this deformation into consideration. Neighboring cells are assumed to be coupled by gap junctions. Gap junctions have been observed in EM studies (15) both between cells in the same layer, and also penetrating the mesoglea to connect the ectoderm and endoderm (15, 66, 67). Further, single-cell RNA sequence analysis in *Hydra* shows multiple innexin types in both epithelial cells and neurons (37). In most systems, nerve stimulation alone does not activate the majority of smooth muscle cells; rather, activation is propagated via intercellular communications between muscle cells (29, 68).

Gap junctions propagate signals by (i) allowing the diffusion of Ca^{2+} as well as second messengers like IP_3; (ii) conducting electrical signals (29, 68, 69). We hypothesize that the two different observed forms of wave propagation in *Hydra* (slow waves and fast calcium synchronization) both occur through different epithelial activation patterns. For slow waves, the propagation of IP_3, but not Ca^{2+} (of which the effect is trivial, as addressed in (38, 39, 70)), through gap junctions is believed to primarily trigger intercellular calcium waves (ICW) (71), which is supported by many previous models on smooth muscle (39, 72–75).

Calcium synchronization (the fast wave) has generally been modelled through the electrical conduction property of gap junctions (62, 76, 77).

Based on this setting, we simulate several different muscle activation patterns, by assuming the necessary neural stimulation for each pattern and applying it to trigger specific muscle cells directly:

Body-column wave.

We hypothesize that the initiation of bodycolumn waves arises from neuromuscular junctions at which neurons release a neuropeptide that triggers the slow pathway in the muscle cells which are randomly located in the body column. Therefore, to simulate these waves, we randomly select a 2×2 region of cells in the sheet and stimulate their slow pathways. The elevated IP_3 in the stimulated cells diffuses to the neighboring cells and triggers the slow dynamics there, resulting in slow calcium waves propagating through the corresponding local domains. Example results of the simulation are shown in Fig. 4B.

Bending wave.

A second type of slow wave initiates at the peduncular ectoderm and slowly propagates in the oral direction (9). This asymmetrical calcium activity in the ectoderm is believed to cause bending. To simulate the bending wave, we stimulate the slow pathway in a 4×4 cell-patch located in the peduncle of the ectoderm sheet of our model; propagation is due as above to gap junctional IP_3 diffusion (Fig. 4C). To obtain a wave as observed in data, the model assumes that gap junctional coupling is anisotropic, larger longitudinally than circumferentially (see Materials and Methods).

Fast wave (contraction pulse).

Hydra's contraction burst (CB) is driven by the firing of a unique subnetwork of the ectodermal nerve net (8) that is distributed across the body but particularly concentrated in a ring in the peduncle. Each contraction pulse causes a global calcium synchronization which activates all muscle cells in both ectoderm and endoderm. Measurements in (9) showed that the contraction pulses initiate in the peduncular epithelium and propagate to the rest of the body column. Here we assume these neurons to be the primary source of activation. We initiate the fast wave by simulating inputs from a ring of neurons in the peduncle onto the connected muscle cells: we stimulate the fast pathway dynamics in the bottom row (1×30) of the ectodermal sheet. Elevated membrane potentials propagate rapidly to the remainder of the cells via their electrical coupling, giving a global calcium synchronization, as shown in Fig. 4D.

Body column dynamics.

It seems that extending the muscle sheet model to a dual-layer body column model is very straightforward: coupling the leftmost cells and the rightmost ones to form a hollow cylinder, then duplicating it to represent the other layer, and regarding the two cylinders together as a dual-layer body column. However, calcium imaging shows that this bi-layer activation is not actually observed: during a contraction burst, neuronal activity is confined to the ectoderm, which indicates CB neurons are located in the only ectoderm (8), while both the ectoderm and the endoderm show an almost synchronous fast wave of epitheliomuscular calcium (Fig. 5); in contrast, body column waves and bending waves are only observed in the ectoderm (9).

We assume the synchronization of fast waves in the two layers is due to electrical coupling through the cross-layer gap junctions which penetrate mesoglea: when cells in the

ectoderm are electrically activated, the action potential can propagate through the gap junction and trigger activity in the endodermal epithelium, then we must also assume crosslayer gap junctions can allow a flow of IP_3. However, there is no evidence that slow waves in ectoderm propagate to the endoderm (9). How can we explain this contradiction?

We hypothesize that the cross-layer gap junctions are sparsely distributed between the two layers (Fig. 6A), and the ability of cross-layer gap junctions to transmit global fast waves but block local slow waves is due simply to their density. We test this by varying the connectivity ratio (density) of the cross-layer gap junctions in our model. We found when the connectivity ratio is high, both fast and slow waves can propagate between the two layers; when the ratio is low neither of the two waves propagate; and there is a intermediate range in which only the fast wave crosses the layer (Fig. 6B-D).

To probe the effect of the density of cross-layer gap junctions on the propagation of trans-mesoglea calcium waves, we quantitatively analyzed the relationship between the averaged calcium concentration of the endodermal muscle sheet and the connection density, after stimulating the ectodermal muscle cells' fast (Fig. 6E) and slow (Fig. 6F) pathway. As shown, for both slow wave and fast waves, a higher connection density of cross-layer gap junctions allows stronger calcium wave propagation from the stimulated ectoderm to the endoderm. When the connection density is very low or very high, the standard deviation is small. In intermediate ranges, there is considerable variability, indicating that the specific placement of cross-layer connections can also affect trans-mesoglea propagation. Thus, when the cross-layer gap junctions are distributed under a range of connection density in specific patterns, only the fast waves can cross layers and the slow waves are limited to the directly stimulated ectodermal layer.

To quantitatively compare the speed of the simulated waves with experimental data, we identified the wavefront of the bending wave in our model as shown in Fig. 6G, from which the average propagation speed can be calculated as around 0.9 cells/s. The length of our biomechanical model is in the range of 0.6mm (fully contracted) - 1.7mm (elongated), based on which the length of each cell can be calculated as 9.8 μm (contracted) - 28.8μm (elongated), so the propagation speed is in the range of 9 μm/s - 26.5 μm/s. In (9), the propagation speed of the bending wave was calibrated as 13 ± 0.7 μm/s, which falls in the range of the simulation. The speed of the fast wavefront is computed as shown in Fig. 6H, giving 0.7 cells/ms, or 6 mm/s when the model is in the contracted state. This is of the same order as the propagation speed measured from calcium imaging (4.6-5 mm/s) in (9).

Transform calcium dynamics to muscle contraction.

Now that we can simulate the various calcium dynamics and activation patterns of the whole-body muscle system, we then modeled how they generate contraction.

Calcium to force.

In smooth muscle, a rise of $[Ca^{2+}]_i$ (intracellular calcium concentration) leads to a rise of calmodulin, leading to increased activation of MLCK (myosin light-chain kinase), phosphorylation of myosin, and thus contraction (41). The Hai-Murphy model of smooth muscle (78) uses four forms of the crossbridge to simulate the force-production process, where Ca^{2+} plays a role in MLCK activation. The Hai-Murphy model includes the "latch-state" of the crossbridge, which allows the maintenance of steady-state stress of muscle even if the Ca^{2+} concentration has decreased. Depending on parameters, the model can provide either fast-acting phasic behavior as for "fast" myosin isoforms, or tonic contraction via the latch-bridge mechanism, as for "slow" isoforms. This mechanism is

energetically efficient but at the cost of a reduced rate of muscle shortening (79). (– moved to the following subsection: Difference between layers) Modified Hai-Murphy models have been used to simulate contractions in arteriole (80) and uterine (57, 81) smooth muscle. In our work, we applied a modified version of the Hai-Murphy model, following (57) and (81), to transform $[Ca^{2+}]_i$ into active stress.

Force to contraction.

To further convert the stress into movements of *Hydra*, as our final step, we need to construct a model that resembles the hydrostatic skeleton of *Hydra* and can simulate the biomechanics of the body, driven by the fluid is shown as purple. transformed stress. Models of hydrostatic skeletons are rare and have focused on muscular hydrostats (– warned by a reviewer), including leech (82, 83) and octopus tentacles (84). Related work has explored the neural control of swimming in jellyfish (6); in this case the animal is an open membrane and the model treats the hydrodynamic interaction with the surrounding fluid. (– move to Introduction to make the citation more visible?) We construct our model using the COMSOL Multiphysics® 5.3a. We approximate the anatomy of *Hydra* with a simplified biomechanical model that contains two domains: the body shell and the enclosed fluid. The body shell, which represents the combination of the ectoderm and endoderm layers and the mesoglea, is composed of a half spherical shell at the hypostome and a half spherical shell at the peduncle, connected by a uniform body column cylinder shell (Fig. 7). In order to manipulate the biomechanical model at high resolution, we divide the body shell into 10 (radial) by 20 (longitudinal) elements. The body shell and enclosed fluid together form a hydrostatic skeleton.

To define the passive properties of *Hydra* body, we define the body shell of our model as an incompressible hyperelastic material which follows a Neo-Hookean model (85). Hyperelastic materials exhibit a nonlinear stress-strain behavior and can respond elastically under very large strains (86). Muscle tissues are often well-described (87–89) and modeled (90–92) using hyperelastic properties. The passive biomechanical properties were mostly modeled based on Hill's three element model (93). Since biological soft tissues have hyperplasticity or viscoelasticity (94), we use hyperelastic material parameters to model the *Hydra* muscle shell and further incorporate viscoelasticity by including a Kelvin-Voigt model into the body shell material. For the enclosed fluid, we use the COMSOL simulation environment's preset material "Water", with a moving mesh.

While the COMSOL architecture as described handles the passive biomechanical properties, we apply time-varying active stresses generated by the output of the calcium signaling models; the ectodermal model drives longitudinal external stresses, while the endodermal output drives stress in the circular direction. We obtain the active stress from the calcium signaling model as described above, and average the stress of neighboring 9 cells, coarse-graining the original 30×60 matrix to fit the 10×20 dimensions of the biomechanical model. This stress pattern was applied to the corresponding elements of the biomechanical model using LiveLink™ for MATLAB.

Difference between layers.

A major question raised by experimental data is how the co-activation of the opposing ectodermal and endodermal contracting forces can give a total effect of longitudinal contraction of *Hydra*, instead of opposing each other; also, why neither layers

are activated between CB's, but *Hydra* still exhibits an elongation behavior (Fig. 5)? Actually, when we directly apply the transformed stress from calcium dynamics on the biomechanical model, we observed an opposing behavior (not shown) of the model instead of contraction like a real *Hydra*, which is consistent with our concern.

We found these can be interpreted by assuming ectoderm and endoderm have different types of muscle, which can be simulated by setting different parameters of Hai-Murphy model for them: depending on parameters, Hai-Murphy model can provide either fast-acting phasic behavior as for "fast" myosin isoforms, or tonic contraction via the latch-bridge mechanism, as for "slow" isoforms (79). Therefore, by assuming the ectoderm is phasic and endoderm is tonic, with the hypothesis that ectoderm can generate a larger maximum stress than that of endoderm (inspired by the observations that the myonemes in ectoderm are longer than those in endoderm (11)), we can successfully simulate the interplay of contraction and elongation – when CB neurons are firing and both layers are activated, ectoderm plays a dominating role, thus driving a longitudinal contraction; when CB firing ceases and $[Ca^{2+}]_i$ drops in both layers, the endoderm dominates and drives *Hydra* to elongate slowly, because of its tonic property that allows it to maintain the stress longer, requiring no direct neuronal stimulation.

Integrating together: from neural activity to behaviors.

With the above bottom-up pipeline, we are now capable of simulating the observed behaviors of *Hydra*, using different spatiotemporal neural firing patterns to drive muscle activation. Fig. 8 shows our simulation of several typical behaviors of *Hydra*. How we

simulate contraction and elongation has been introduced above. We simulate bending by stimulating the slow pathways of a small localized group of ectodermal cells at the peduncle, which triggers the bending wave as shown in Fig. 4, generating local contraction which causes *Hydra* to bend towards the stimulated side. This shows that activation of the slow and fast pathways can coexist without interfering with each other and that the contraction event in the fast pathway does not saturate the calcium dynamics. For nodding, a separate nerve net, called the sub-tentacular network (8), is found to be correlated with nodding behavior. Here we assume that this network simply stimulates the slow pathways of a small set of ectodermal cells in the sub-hypostomal region. This is similar to bending behavior but with an opposite location. Our model is thus able to generate a "bending" of the hypostome towards the stimulated side.

We then attempt simulating naturalistic behaviors of *Hydra* from videos where behaviors were recorded. Left undisturbed, *Hydra* undergoes repeated cycles of contraction and elongation, combined with bending. We extract the integrated GCaMP fluorescence trace from a neuronal imaging video and use it to infer the firing times of the CB neurons (Fig. 9A), with further adding sparse triggering times for the bending waves (Fig. 9B). We use this stimulation to drive fast calcium waves and slow bending waves in the epithelial sheets (Fig. 9C, D) , of which the fluorescence matches the observed curves in Fig. 5 (– do we even need to include fluorescence?). After encoding the calcium concentration into force (Fig. 9E, F)), we use it to drive the biomechanical model, successfully exhibiting a series of behaviors that mimic the real *Hydra* (Fig. 9H).

The simulated length changes show very good quantitative agreement with the dynamics of contraction and elongation of the animal (Fig. 9G). An animation of the whole pipeline of simulation is provided in the Supplementary Information (Movie S1).

Discussion

In this work, we have succeeded in implementing a model framework that predicts behaviors from neural firing patterns. Here we review the assumptions, required mechanisms and limitations of our model. We began with a biophysical model for single muscle cell dynamics that is grounded in known molecular mechanisms; we then linked muscle cells into a network via gap junctional coupling, which successfully simulated multiple timescale calcium activation dynamics observed in GCaMP imaging experiments in *Hydra*. Such multiple-timescale calcium signaling was also recorded in arterial smooth muscle cells (65). We then used this model to generate active stress to drive a passive biomechanical model of the body. This model successfully simulated *Hydra* behaviors including contraction bursts, bending and elongation. These two components together form a model that can exhibit different behaviors with given neuronal stimulation, and can thus serve as a testbed for reverse engineering neural activity needed for each behavior of *Hydra*.

In order to match observed activity and behavior, we raised and addressed a series of questions. We accounted for the two distinct time scales of calcium patterns in imaging experiments by assuming that there are two different calcium pathways (ionotropic and metabotropic) in each single muscle cell, then captured the different propagation speeds through the dual functions (electrical coupling and chemical diffusion) of gap junctions. By

assuming sparsely distributed cross-layer gap junctions between ectoderm and endoderm, we succeeded in producing synchronized fast waves in the two layers along with the isolation of slow waves to the ectoderm. To explain how *Hydra* can longitudinally contract although the two counteraligned muscle layers are simultaneously activated, we postulated that muscles of ectoderm and endoderm have different properties (phasic and tonic). This further explains how *Hydra* can elongate with no apparent endodermal calcium activation (Fig. 5). Putting these factors together, we successfully simulated cycles of contraction, elongation and bending.

Despite this success, there are many details and limitations that need to be explored further. For instance, how and which groups of neurons transmit these distinct stimuli to the muscle is still unclear. We have considered a simplified structure of *Hydra*, and neglected the effects of the surrounding water, whose viscosity and buoyancy may influence behavior (95–97). Furthermore, our model only assumes feedforward transformations from neural activity to behaviors, although it is likely important to understand how behavior influences neural firing through mechanosensation and other forms of sensory feedback.

Neuromuscular transmission in *Hydra*.

An open question is how and where neurons connect to and stimulate muscles. Electron microscopic observations showed clear evidence of neuromuscular synaptic junctions in *Hydra* tissue (26). Further studies have shown that the neuropeptides Hydra-RFamides and Hydra-KVamide (expressed in the peduncle region) may play roles in neuromuscular transmission (42, 98, 99). The neuropeptide Hym-176C can induce ectoderm contraction and is selectively expressed in ectodermal peduncle neurons

(37, 98, 100, 101). Non-selective cation channels HyNaCs were identified in epitheliomuscular cells, which are directly activated by Hydra-RFamides I and II and can depolarize the cellular membrane potential (42, 102). In our model, we propose that two different types of neuropeptides play the roles of triggering different pathways, enabling differential control of different timescales dynamics in the muscle layers, potentially by distinct neurons.

Electrical signaling in nerve net and muscle.

Our model treats the question of whether electrical activity during contraction bursts is transmitted through the nerve net or the muscle layer. We propose that hypostomal neurons play a role of integrating information from the environment: following a decision to fire, the signal is propagated through the sparsely distributed CB nerve subnet to the peduncle ring of motor neurons, which acts as the primary drive of contraction. This architecture is supported by the observed propagation of fast calcium activation from the peduncle towards the oral side (9); the expression of Hym-176C in the peduncle (98) and the previous observation of electrical conduction in the nerve-free *Hydra* epithelia (30).

However, we believe that during contraction, synchronous drive from the nerve net is supplemented by the electrical coupling property of muscle cells themselves. The CB neurons are sparsely distributed in the body column; it is unlikely that the CB neurons directly innervate all muscle cells, although it is possible that each neuron drives a small group of them. We simulated the dynamics that result from setting the electrical conductance between muscles to zero and stimulating random small groups of muscle cells; this leads to slowly growing nodes of excitation via the slow chemical diffusion of IP_3 (Fig. 10). Thus we believe that electrical coupling of muscle cells is needed to explain the

rapid synchronization of calcium activity in the epithelium (103). The distributed network of CB neurons are likely necessary to integrate and generate the contraction activity, and may contribute to the robustness of contraction.

Here we demonstrated that sparse electrical coupling between the muscle layers can account for the coactivation of longitudinal and circumferential contraction during contraction bursts. While it is counterintuitive that these muscles would activate together, this may have a functional role; as suggested in (9), the resulting stresses on the body may serve to squeeze absorbed water out of the body walls.

Hydra has two additional known synchronously firing networks, the "rhythmic potentials" RP1 and RP2. We have found no correlation of RP firing with instantaneous length changes; thus it is unlikely that the RP networks directly control muscle contraction. However, it has been suggested the "radial contraction" behavior is particularly related to RP2 (8). The ectodermal RP1 nerve net may inhibit CB neurons therefore suppressing contraction bursts, based on the fact that its frequency is inversely proportional to contraction bursts (8, 21, 104).

Feedback from behavior and the environment.

Our model simulates the transformation from neural stimulation to behaviors as a purely feedforward control pipeline, but there are several ways in which feedback may play a role. The rules that govern the generation of the neural activity are still an open question. Recent experiments have shown that temperature

(24) and osmolarity (23) can influence the CB firing rate in *Hydra*. Neural activity is likely to be influenced by the behavior or the state of the animal through mechanosensation and other sensory inputs. This may occur through direct sensory feedback or through alternate

mechanisms such as changing ionic concentrations in the intercellular medium, the external solution or the interon.

A further source of potential feedback that we neglect is that between the movement of the animal and the dynamics of diffusion. In the model, we assumed that the speed of IP_3 diffusion is faster in the longitudinal direction than in the circumferential direction, in order to account for the different propagation speeds of bending waves in longitudinal and circular directions, in units of cells per second. While it is possible that the density of longitudinally oriented gap junctions may be larger than that of circularly oriented ones, it is also possible that the propagation speeds in the two directions are the same, but since bending waves are usually initiated when *Hydra* is contracted and cells are squeezed longitudinally, the wave may travel through more cells longitudinally than circumferentially. In order to incorporate this, one would need to model the relationship between the coefficient of IP_3 diffusion and the local cell shape. Implementing such feedback between the biophysics of the muscle layer and the geometry of the biomechanical model would require considerable engineering effort. In general, however, accounting for any of these effects is possible by extending the framework of our model.

Body plan simplicity.

Our biomechanical model simplifies *Hydra* to a hollow cylinder with two spherical ends. However, *Hydra*'s body column deviates from cylindrical, slimming toward the peduncle. Furthermore, cells across the body are heterogenous in size and shape. Recent work indicates that there is variation in the Young's modulus of the body column, and suggests that this can affect somersaulting behavior (95). Future work could explore more precisely how the body wall mechanics transform neural signals and muscle forces into

behavior. Further, we do not attempt to model the tentacles, whose sensory input likely contributes significantly to *Hydra*'s movement, and whose adhesion to surfaces frequently affects body movement. Modeling such details will be necessary to obtain detailed quantitative agreement between the model and additional aspects of behavior. Our goal here was to capture the most significant factors of the biomechanics that underlie the behaviors of *Hydra* that have to date been recorded simultaneously with calcium imaging, excluding higher order complexities. We hope our model will serve as a starting point for further work to capture the full richness of *Hydra*'s natural behavior.

Figures

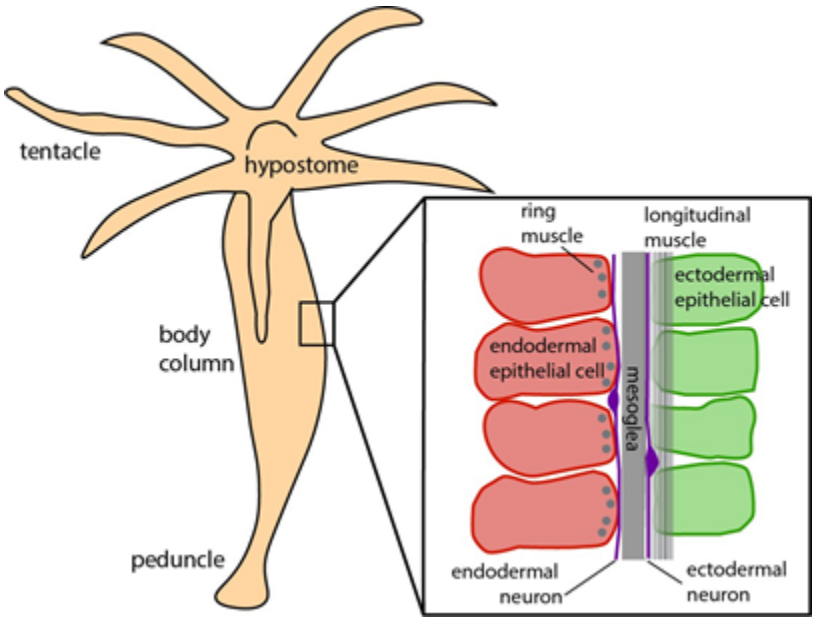

Fig. 1. Simplified *Hydra* anatomy, adapted from (10).

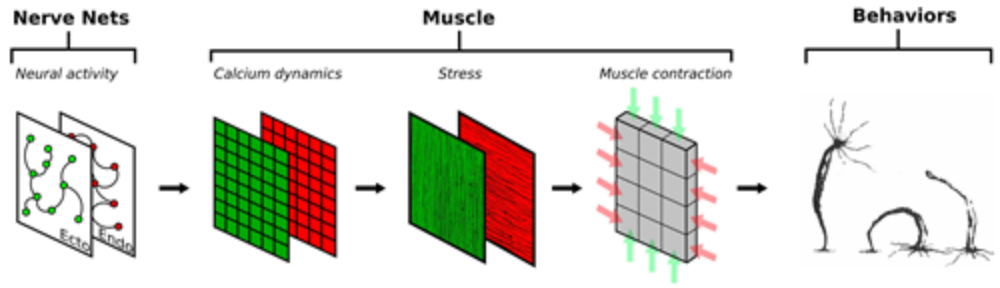

Fig. 2. Project Framework. Neural activity patterns trigger calcium dynamics in the muscle layers, which are transformed into contractile forces in the longitudinal (ectoderm; green) and circumferential (endoderm; red) directions, here indicated by the direction of fibres in the muscle layers. This provides the active force to drive a viscoelastic biomechanical model of the Hydra body column, simulating behaviors

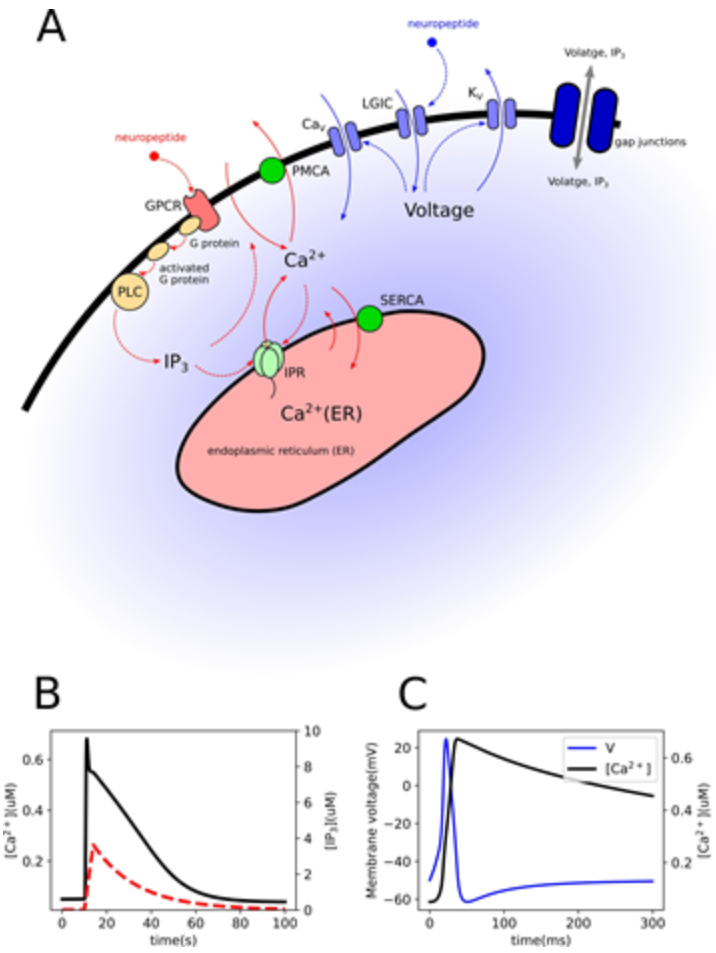

Fig. 3. Single cell dynamics. (*A*) Intracellular calcium signaling model including two pathways: (i) in the *slow pathway* (red), neuropeptides bind a G protein-coupled receptor (GPCR) and activate a G protein, which activates phospholipase C (PLC) and hydrolyzes phosphatidylinositol bisphosphate (PIP2) into inositol 1,4,5-trisphosphate (IP3), which plays a role of the second messenger for calcium signaling. IP3 can

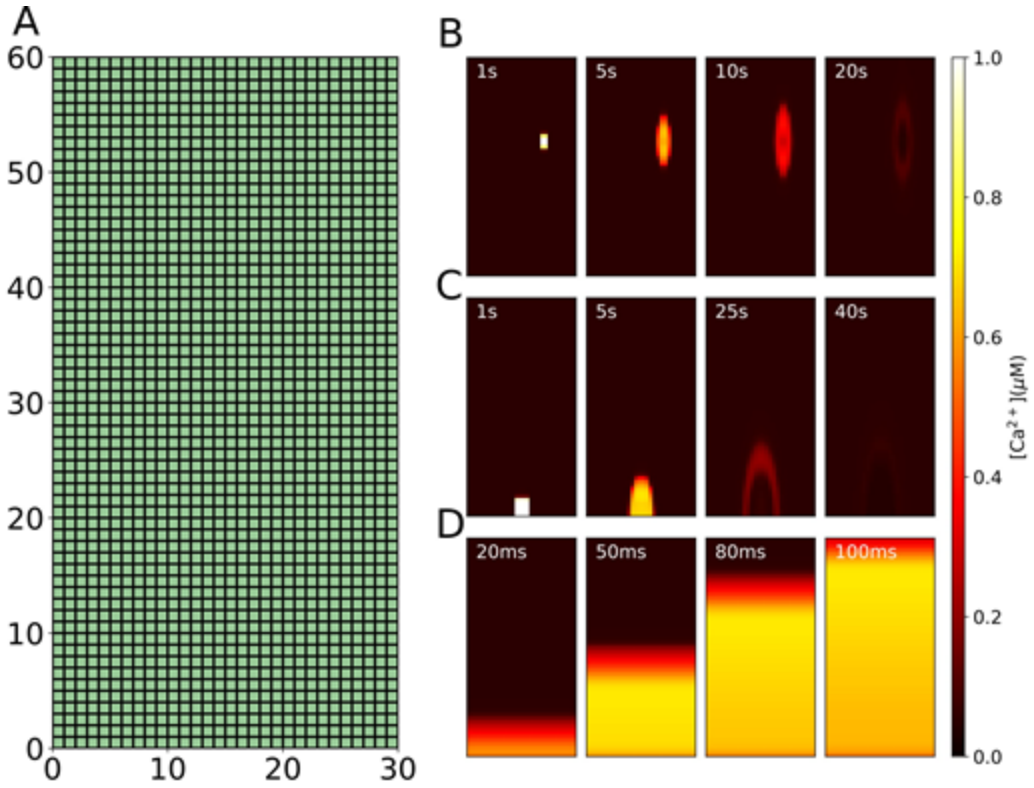

Fig. 4. Muscle sheet dynamics. (*A*) We simulate multicellular dynamics by coupling single cell models to their neighbors by gap junctions. (*B*) Simulation of the body column wave. (*C*) Simulation of the bending wave. (*D*) Simulation of the contraction pulse (fast wave).

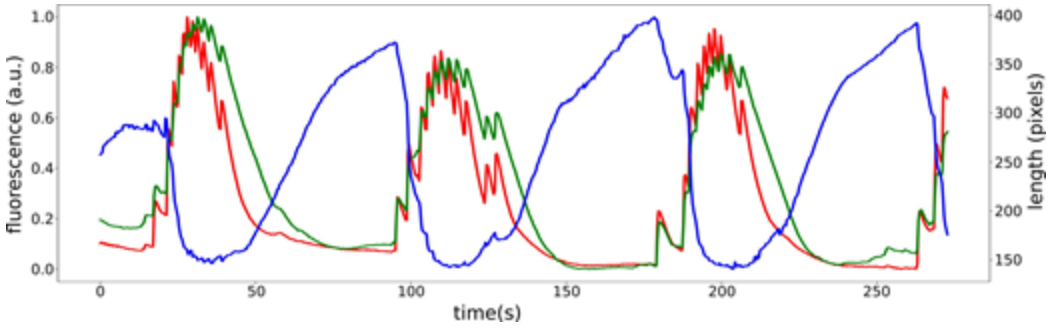

Fig. 5. Fluorescent/Length Correlation Recorded fluorescence from calcium imaging showing simultaneous activation of ectoderm (green) and endoderm (red) during contractions, shown by computing the corresponding time-varying length (blue) of Hydra.

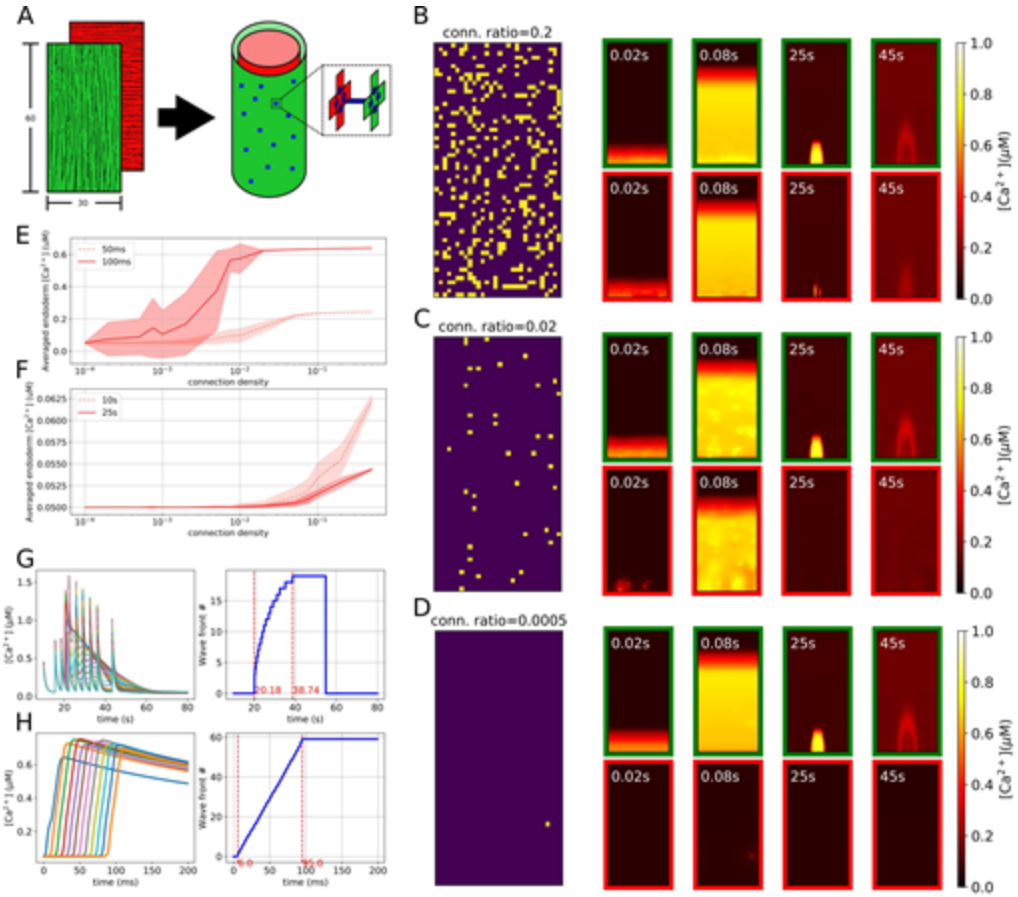

Fig. 6. Body column settings and dynamics. (*A*) The layout of the body column model. Green and red represent the ectodermal and endodermal layers respectively, in which the myonemes are respectively aligned in longitudinal and circumferential directions, as represented by the fibre directions. Blue dots represent cross-layer gap junctions. (*B-D*) Connectivity patterns and calcium patterns of ectoderm (green border) and endoderm (red border) in simulations with different connectivity ratios, where the ratios are separately 20% (*B*), 2% (*C*) and 0.05% (*D*). In connectivity patterns each bright spot represents a gap-junctional connection at that position. (*E-F*) Diagrams show cross-layer propagation for different connection densities of cross-layer gap junctions. We simulate 20 epochs for each density; we take snapshots at 50ms and 100ms after only triggering the fast pathway (*E*), and 10s and 25s after only triggering the slow pathway (*F*), then average the [Ca2+]*i* of the whole endoderm, plotting the mean and standard deviation of the 20 epochs for each density at these time points. (*G-H*) [Ca2+]*i* traces and wavefronts along the center longitudinal line (marked in the dashed rectangle), shown for the bending wave (*G*) and fast wave (*H*). The right sides show how the wave fronts evolve with time.

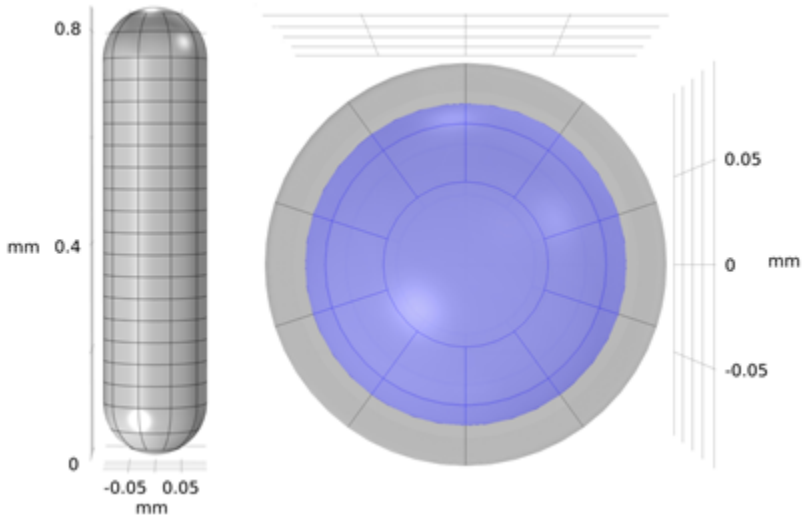

Fig. 7. Model Geometry. Geometry of the biomechanical model from a side view (left) and top view (right). Gray represents the muscle shell domain, while the enclosed fluid is shown as purple.

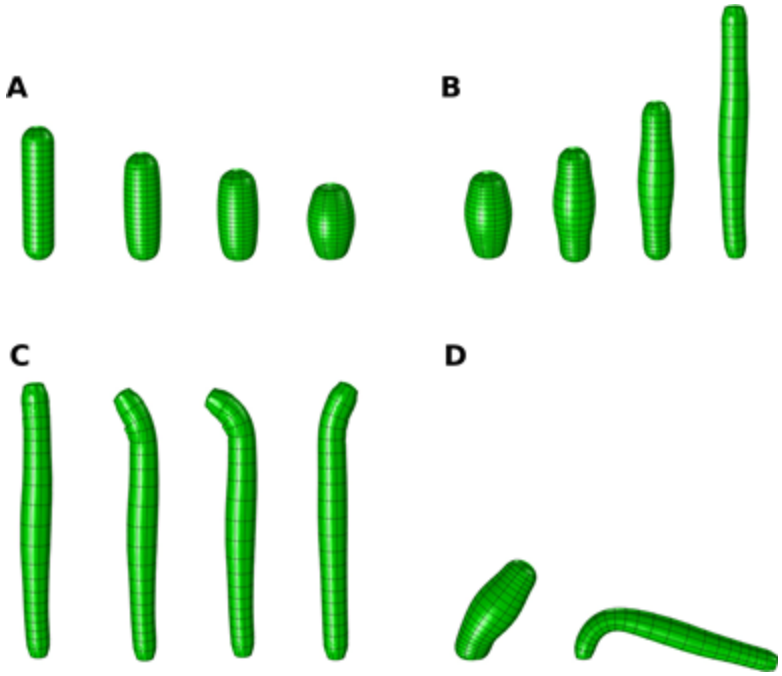

Fig. 8. Simulated Behaviors. (*A*) contraction (*B*) elongation (*C*) nodding (*D*) bending

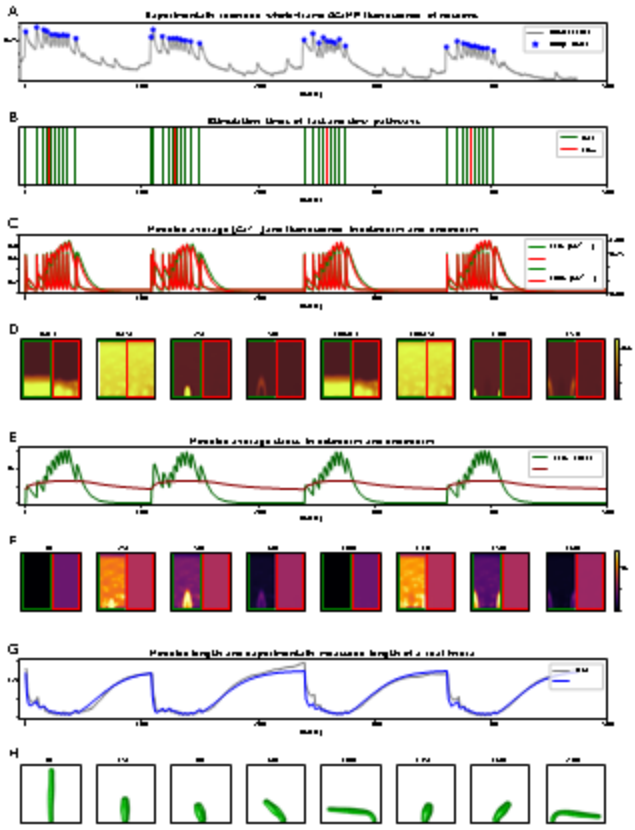

Fig. 9. Pipeline of the simulation from neural activity to behaviors. (*A-B*) NGCaMP fluorescence trace: stars mark estimated times of neural firing (*A*) and consequently, stimulation times for the model (*B*). (*C-D*) Averaged [Ca2+]*i* and fluorescence inten- sities in ectoderm and endoderm (*C*) and [Ca2+]*i* patterns of some moments (*D*). (*E-F*) Averaged active stress in ectoderm and endoderm (*E*) and stress patterns of some moments (*F*). (*G-H*) Comparison between length evolution of the model and from a *Hydra* (*G*) recording and some stills of the final simulated behaviors from the model (H)

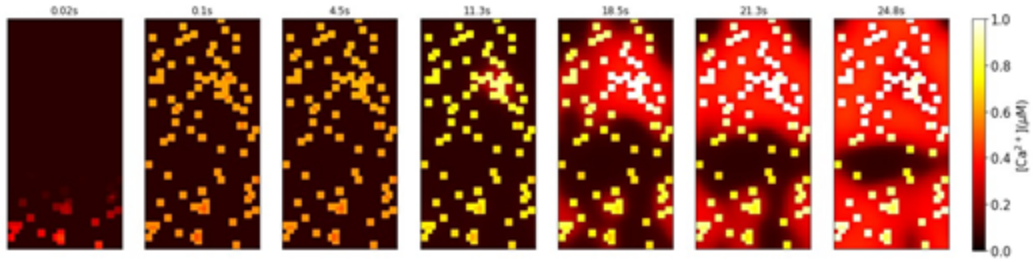

Fig. 10. Calcium Model. Modeled calcium activation pattern under sequential stimulation of the fast pathways of randomly chosen 2×2 groups of muscle cells in the body column with no gap junctional electrical conductance

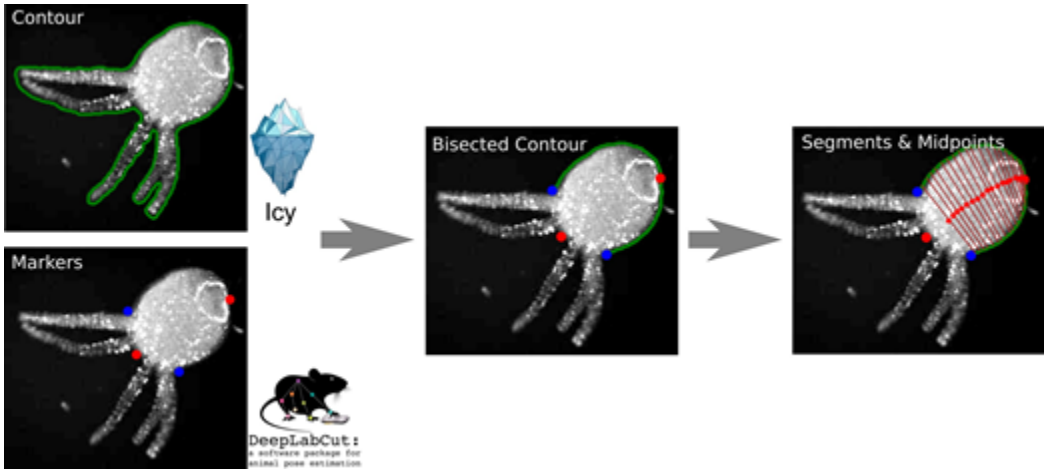

Fig. 11. Analysis Pipeline. Contours of body column are identified via ICY and Hypostome, Peduncle and tentacle/bodycollumn intersections are tracked via DEEPLABCUT, in parallel. Tentacles are removed. Hydra is segmented and midline is Identified

References

1. Daniel T (1995) Invertebrate swimming: integrating internal and external mechanics. Symposia of the Society for Experimental Biology 49:61—89.
2. Rajagopal A, et al. (2016) Full-body musculoskeletal model for muscle-driven simulation of human gait. IEEE Transactions on Biomedical Engineering 63(10):2068–2079.
3. Delp SL, Loan JP (2000) A computational framework for simulating and analyzing human and animal movement. Computing in Science Engineering 2(5):46–55.
4. Ting LH, Chiel HJ (2017) Muscle, biomechanics, and implications for neural control. Neurobiology of Motor Control: Fundamental Concepts and New Directions pp. 365–416.
5. Kim J, Santos JA, Alkema MJ, Shlizerman E (2019) Whole integration of neural connectomics, dynamics and bio-mechanics for identification of behavioral sensorimotor pathways in caenorhabditis elegans. bioRxiv p. 724328.
6. Pallasdies F, Goedeke S, Braun W, Memmesheimer RM (2019) From single neurons to behavior in the jellyfish aurelia aurita. Elife 8:e50084.
7. Kim J, Shlizerman E (2020) Deep reinforcement learning for neural control. arXiv preprint arXiv:2006.07352.
8. Dupre C, Yuste R (2017) Non-overlapping neural networks in hydra vulgaris. Current Biology 27(8):1085–1097.

9. Szymanski JR, Yuste R (2019) Mapping the whole-body muscle activity of hydra vulgaris. Current Biology 29(11):1807–1817.
10. Technau U, Steele RE (2011) Evolutionary crossroads in developmental biology: Cnidaria. Development 138(8):1447–1458.
11. Leclère L, Röttinger E (2017) Diversity of cnidarian muscles: function, anatomy, development and regeneration. Frontiers in cell and developmental biology 4:157. Kier WM (2012) The diversity of hydrostatic skeletons. Journal of Experimental Biology 215(8):1247–1257.
12. Fujisawa T, Hayakawa E (2012) Peptide signaling in hydra. International Journal of Developmental Biology 56(6-7-8):543–550.
13. Klimovich AV, Bosch TC (2018) Rethinking the role of the nervous system: lessons from the hydra holobiont. BioEssays 40(9):1800060.
14. Takaku Y, et al. (2014) Innexin gap junctions in nerve cells coordinate spontaneous contractile behavior in hydra polyps. Scientific reports 4:3573.
15. Trembley A (1744) Mémoires pour servir à l'histoire d'un genre de polypes d'eau douce, à bras en forme de cornes. (Chez Jean & Herman Verbeek) Vol. 1.
16. Rushforth NB, Burnett AL, Maynard R (1963) Behavior in hydra: contraction responses of hydra pirardi to mechanical and light stimuli. Science 139(3556):760–761.
17. Passano L, McCullough C (1964) Co-ordinating systems and behaviour in hydra: I. pacemaker system of the periodic contractions. Journal of Experimental Biology 41(3):643–664.

18. Passano L, McCullough C (1965) Co-ordinating systems and behaviour in hydra ii. the rhythmic potential system. Journal of Experimental Biology 42(2):205–231.
19. Han S, Taralova E, Dupre C, Yuste R (2018) Comprehensive machine learning analysis of hydra behavior reveals a stable basal behavioral repertoire. Elife 7:e32605.
20. Passano L, McCullough C (1962) The light response and the rhythmic potentials of hydra. Proceedings of the National Academy of Sciences of the United States of America 48(8):1376.
21. Passano L, McCullough C (1963) Pacemaker hierarchies controlling the behaviour of hydras. Nature 199(4899):1174–1175.
22. Yamamoto W, Yuste R (2019) Whole-body imaging of neural and muscle activity during behavior in hydra: bidirectional effects of osmolarity on contraction bursts. bioRxiv.
23. Tzouanas CN, Kim S, Badhiwala KN, Avants BW, Robinson J (2019) Thermal stimulation temperature is encoded as a firing rate in a hydra nerve ring. bioRxiv p. 787648.
24. Murillo-Rincon AP, et al. (2017) Spontaneous body contractions are modulated by the microbiome of hydra. Scientific reports 7(1):1–9.
25. Westfall JA (1973) Ultrastructural evidence for a granule-containing sensory-motorinterneuron in hydra littoralis. Journal of ultrastructure research 42(3-4):268–282.
26. Josephson RK (1967) Conduction and contraction in the column of hydra. Journal of Experimental Biology 47(1):179–190.

27. Josephson RK, Macklin M (1969) Electrical properties of the body wall of hydra. The Journal of General Physiology 53(5):638–665.
28. Anderson PA (1980) Epithelial conduction: its properties and functions. Progress in neurobiology 15(3):161–203.
29. Campbell R, Josephson R, Schwab W, Rushforth N (1976) Excitability of nerve-free hydra. Nature 262(5567):388–390.
30. Lepault J, McDowall A, Grimmelikhuijzen C (1980) Intercellular junctions in nerve-free hydra. Cell and tissue research 209(2):217–224.
31. Kass-Simon G (1970) Multiple excitation sites and straight-line conduction in contraction burst system of hydra in AMERICAN ZOOLOGIST. (SOC INTEGRATIVE COMPARATIVE BIOLOGY 1313 DOLLEY MADISON BLVD, NO 402, MCLEAN . . .), Vol. 10, pp. 505–+.
32. Kass-Simon G (1972) Longitudinal conduction of contraction burst pulses from hypostomal excitation loci inhydra attenuata. Journal of comparative physiology 80(1):29–49.
33. Rushforth NB (1971) Behavioral and electrophysiological studies of hydra. i. analysis of contraction pulse patterns. The Biological Bulletin 140(2):255–273.
34. Mackie G (1965) Conduction in the nerve-free epithelia of siphonophores. American Zoologist 5(3):439–453.
35. Mackie G, Passano L (1968) Epithelial conduction in hydromedusae. The Journal of general physiology 52(4):600–621.
36. Siebert S, et al. (2019) Stem cell differentiation trajectories in hydra resolved at single-cell resolution. Science 365(6451):eaav9314.

37. Koenigsberger M, Sauser R, Lamboley M, Bény JL, Meister JJ (2004) Ca2+ dynamics in a population of smooth muscle cells: modeling the recruitment and synchronization. Biophysical journal 87(1):92–104.
38. Höfer T, Venance L, Giaume C (2002) Control and plasticity of intercellular calcium waves in astrocytes: a modeling approach. Journal of Neuroscience 22(12):4850–4859.
39. Loppini A, Braun M, Filippi S, Pedersen MG (2015) Mathematical modeling of gap junction coupling and electrical activity in human β-cells. Physical biology 12(6):066002.
40. Dupont G, Falcke M, Kirk V, Sneyd J (2016) Models of calcium signalling. (Springer) Vol. 43.
41. Gründer S, Assmann M (2015) Peptide-gated ion channels and the simple nervous system of hydra. Journal of Experimental Biology 218(4):551–561.
42. Hill-Eubanks DC, Werner ME, Heppner TJ, Nelson MT (2011) Calcium signaling in smooth muscle. Cold Spring Harbor perspectives in biology 3(9):a004549.
43. Johnson CJ, Razy-Krajka F, Stolfi A (2020) Expression of smooth muscle-like effectors and core cardiomyocyte regulators in the contractile papillae of ciona. EvoDevo 11(1):1–18.
44. Balachander N, Masthan K, Anbazhagan V, , et al. (2015) Myoepithelial cells in pathology. Journal of pharmacy & bioallied sciences 7.
45. Horowitz A, Menice CB, Laporte R, Morgan KG (1996) Mechanisms of smooth muscle contraction. Physiological reviews 76(4):967–1003.

46. Berridge MJ (2008) Smooth muscle cell calcium activation mechanisms. The Journal of physiology 586(21):5047–5061.
47. Kuo IY, Ehrlich BE (2015) Signaling in muscle contraction. Cold Spring Harbor perspectives in biology 7(2):a006023.
48. Holman MA, Anderson PA (1991) Voltage-activated ionic currents in myoepithelial cells isolated from the sea anemone calliactis tricolor. Journal of experimental biology 161(1):333– 346.
49. De Young GW, Keizer J (1992) A single-pool inositol 1, 4, 5-trisphosphate-receptor-based model for agonist-stimulated oscillations in ca2+ concentration. Proceedings of the National Academy of Sciences 89(20):9895–9899.
50. Li YX, Rinzel J (1994) Equations for insp3 receptor-mediated [ca2+] i oscillations derived from a detailed kinetic model: a hodgkin-huxley like formalism. Journal of theoretical Biology 166(4):461–473.
51. Schuster S, Marhl M, Höfer T (2002) Modelling of simple and complex calcium oscillations: From single-cell responses to intercellular signalling. European Journal of Biochemistry 269(5):1333–1355.
52. Handy G, Taheri M, White JA, Borisyuk A (2017) Mathematical investigation of ip 3-dependent calcium dynamics in astrocytes. Journal of computational neuroscience 42(3):257–273.
53. Rihana S, Terrien J, Germain G, Marque C (2009) Mathematical modeling of electrical activity of uterine muscle cells. Medical & biological engineering & computing 47(6):665–675.

54. Tong WC, et al. (2011) A computational model of the ionic currents, ca2+ dynamics and action potentials underlying contraction of isolated uterine smooth muscle. PloS one 6(4).
55. Cochran AL, Gao Y (2015) A model and simulation of uterine contractions. Mathematics and Mechanics of Solids 20(5):540–564.
56. Yochum M, Laforêt J, Marque C (2016) An electro-mechanical multiscale model of uterine pregnancy contraction. Computers in biology and medicine 77:182–194.
57. Testrow CP, Holden AV, Shmygol A, Zhang H (2018) A computational model of excitation and contraction in uterine myocytes from the pregnant rat. Scientific reports 8(1):1–14.
58. Corrias A, Buist ML (2007) A quantitative model of gastric smooth muscle cellular activation. Annals of biomedical engineering 35(9):1595–1607.
59. Mahapatra C, Brain KL, Manchanda R (2018) A biophysically constrained computational model of the action potential of mouse urinary bladder smooth muscle. PloS one 13(7).
60. Fridlyand LE, Jacobson D, Kuznetsov A, Philipson LH (2009) A model of action potentials and fast ca2+ dynamics in pancreatic β-cells. Biophysical journal 96(8):3126–3139.
61. Imtiaz MS, Katnik CP, Smith DW, van Helden DF (2006) Role of voltage-dependent modulation of store ca2+ release in synchronization of ca2+ oscillations. Biophysical journal 90(1):1–23.

62. Kusters J, et al. (2005) Stabilizing role of calcium store-dependent plasma membrane calcium channels in action-potential firing and intracellular calcium oscillations. Biophysical journal 89(6):3741–3756.
63. Fletcher PA, Li YX (2009) An integrated model of electrical spiking, bursting, and calcium oscillations in gnrh neurons. Biophysical journal 96(11):4514–4524.
64. Halidi N, Boittin FX, Bény JL, Meister JJ (2011) Propagation of fast and slow intercellular ca2+ waves in primary cultured arterial smooth muscle cells. Cell calcium 50(5):459–467.
65. Hand AR, Gobel S (1972) The structural organization of the septate and gap junctions of hydra. The Journal of cell biology 52(2):397–408.
66. Wood RL, Kuda AM (1980) Formation of junctions in regeneratin hydra: Gap junctions. Journal of ultrastructure research 73(3):350–360.
67. Christ GJ, Spray DC, El-Sabban M, Moore LK, Brink PR (1996) Gap junctions in vascular tissues: evaluating the role of intercellular communication in the modulation of vasomotor tone. Circulation Research 79(4):631–646.
68. Huizinga J, Liu L, Blennerhassett M, Thuneberg L, Molleman A (1992) Intercellular communication in smooth muscle. Experientia 48(10):932–941.
69. Jafri MS, Keizer J (1994) Diffusion of inositol 1, 4, 5-trisphosphate but not ca2+ is necessary for a class of inositol 1, 4, 5-trisphosphate-induced ca2+ waves. Proceedings of the National Academy of Sciences 91(20):9485–9489.
70. Leybaert L, Sanderson MJ (2012) Intercellular ca2+ waves: mechanisms and function. Physiological reviews 92(3):1359–1392.

71. Sneyd J, Wetton B, Charles AC, Sanderson MJ (1995) Intercellular calcium waves mediated by diffusion of inositol trisphosphate: a two-dimensional model. American Journal of Physiology-Cell Physiology 268(6):C1537–C1545.
72. Dupont G, et al. (2000) Mechanism of receptor-oriented intercellular calcium wave propagation in hepatocytes. The FASEB Journal 14(2):279–289.
73. Höfer T, Politi A, Heinrich R (2001) Intercellular ca2+ wave propagation through gap-junctional ca2+ diffusion: a theoretical study. Biophysical journal 80(1):75–87. Goldberg M, De Pittà M, Volman V, Berry H, Ben-Jacob E (2010) Nonlinear gap junctions enable long-distance propagation of pulsating calcium waves in astrocyte networks. PLoS computational biology 6(8).
74. Kusters J, van Meerwijk W, Ypey DL, Theuvenet AP, Gielen C (2008) Fast calcium wave propagation mediated by electrically conducted excitation and boosted by cicr. American Journal of Physiology-Cell Physiology 294(4):C917–C930.
75. Koenigsberger M, Seppey D, Bény JL, Meister JJ (2010) Mechanisms of propagation of intercellular calcium waves in arterial smooth muscle cells. Biophysical journal 99(2):333– 343.
76. Hai CM, Murphy RA (1988) Cross-bridge phosphorylation and regulation of latch state in smooth muscle. American Journal of Physiology-Cell Physiology 254(1):C99–C106.
77. Han S, et al. (2006) Evidence for absence of latch-bridge formation in muscular saphenous arteries. American Journal of Physiology-Heart and Circulatory Physiology 291(1):H138– H146.

78. Wang I, et al. (2008) A mathematical model of airway and pulmonary arteriole smooth muscle. Biophysical journal 94(6):2053–2064.
79. Maggio CD, Jennings SR, Robichaux JL, Stapor PC, Hyman JM (2012) A modified hai–murphy model of uterine smooth muscle contraction. Bulletin of mathematical biology
80. Wadepuhl M, Beyn WJ (1989) Computer simulation of the hydrostatic skeleton. the physical equivalent, mathematics and application to worm-like forms. Journal of theoretical biology 136(4):379–402.
81. Skierczynski B, Wilson R, Kristan Jr W, Skalak R (1996) A model of the hydrostatic skeleton of the leech. Journal of theoretical biology 181(4):329–342.
82. Yekutieli Y, et al. (2005) Dynamic model of the octopus arm. i. biomechanics of the octopus reaching movement. Journal of neurophysiology 94(2):1443–1458.
83. Rivlin R (1948) Large elastic deformations of isotropic materials. i. fundamental concepts. Philosophical Transactions of the Royal Society of London. Series A, Mathematical and Physical Sciences 240(822):459–490.
84. Bower AF (2009) Applied mechanics of solids. (CRC press).
85. Gras LL, Mitton D, Viot P, Laporte S (2012) Hyper-elastic properties of the human sternocleidomastoideus muscle in tension. Journal of the mechanical behavior of biomedical materials 15:131–140.
86. Sarma P, Pidaparti R, Moulik P, Meiss R (2003) Non-linear material models for tracheal smooth muscle tissue. Bio-medical materials and engineering 13(3):235–245.

87. Chagnon G, Rebouah M, Favier D (2015) Hyperelastic energy densities for soft biological tissues: a review. Journal of Elasticity 120(2):129–160.
88. Ansari M, Lee SK, Cho CD, , et al. (2007) Hyperelastic muscle simulation in Key Engineering Materials. (Trans Tech Publ), Vol. 345, pp. 1241–1244.
89. Gras L, Mitton D, Viot P, Laporte S, , et al. (2010) Modelling of human muscle behaviour with a hyper-elastic constitutive law. Computer Methods in Biomechanics and Biomedical Engineering 13(S1):63–64.
90. Tang C, Zhang G, Tsui C (2009) A 3d skeletal muscle model coupled with active contraction of muscle fibres and hyperelastic behaviour. Journal of biomechanics 42(7):865–872.
91. Hill AV (1938) The heat of shortening and the dynamic constants of muscle. Proceedings of the Royal Society of London. Series B-Biological Sciences 126(843):136–195.
92. Martinek J, Stickler Y, Reichel M, Mayr W, Rattay F (2008) A novel approach to simulate hodgkin–huxley-like excitation with comsol multiphysics. Artificial organs 32(8):614–619.
93. Naik S, et al. (2020) Differential tissue stiffness of body column facilitates locomotion of hydra on solid substrates. bioRxiv.
94. Megill WM (2002) Ph.D. thesis (University of British Columbia).
95. Rudolf D, Mould D (2009) An interactive fluid model of jellyfish for animation in International Conference on Computer Vision, Imaging and Computer Graphics. (Springer), pp. 59–72.

96. Yum S, et al. (1998) A novel neuropeptide, hym-176, induces contraction of the ectodermal muscle in hydra. Biochemical and biophysical research communications 248(3):584–590.

97. Hansen GN, Williamson M, Grimmelikhuijzen CJ (2000) Two-color double-labeling in situ hybridization of whole-mount hydra using rna probes for five different hydra neuropeptide preprohormones: evidence for colocalization. Cell and tissue research 301(2):245–253.

98. Noro Y, et al. (2019) Regionalized nervous system in hydra and the mechanism of its development. Gene Expression Patterns 31:42–59.

99. Klimovich A, et al. (2020) Prototypical pacemaker neurons interact with the resident microbiota. Proceedings of the National Academy of Sciences 117(30):17854–17863.

100. Badhiwala KN, Primack AS, Juliano C, Robinson JT (2020) Multiple nerve rings coordinate hydra mechanosensory behavior. bioRxiv.

101. McCullough C (1965) Pacemaker interaction in hydra. American zoologist 5(3):499–504.

102. Carter JA, Hyland C, Steele RE, Collins EMS (2016) Dynamics of mouth opening in hydra. Biophysical journal 110(5):1191–1201.

103. Altschul SF, Gish W, Miller W, Myers EW, Lipman DJ (1990) Basic local alignment search tool. Journal of molecular biology 215(3):403–410.

104. Greenberg DS, et al. (2018) Accurate action potential inference from a calcium sensor protein through biophysical modeling. BioRxiv p. 479055.

105. Lagache T, Hanson A, Fairhall A, Yuste R (2020) Robust single neuron tracking of calcium imaging in behaving hydra. bioRxiv.

106. Schneider CA, Rasband WS, Eliceiri KW (2012) Nih image to imagej: 25 years of image analysis. Nature methods 9(7):671–675.

107. De Chaumont F, et al. (2012) Icy: an open bioimage informatics platform for extended reproducible research. Nature methods 9(7):690–696.

108. Mathis A, et al. (2018) Deeplabcut: markerless pose estimation of user-defined body parts with deep learning. Nature neuroscience 21(9):1281–1289.

CHAPTER 4: Molecular Properties and Phylogenetics of *Hydra Innexins*

Introduction

Gap junctions are pore forming proteins composed of two hemichannels expressed in adjacent cells that dock to connect the cytoplasm of coupled cells. These channels provide communication between cells by allowing small molecules and ions to pass through. This allows the synchronization of neural circuits (Bennett and Zukin, 2004; Choi et al., 2021) and may aid in the proper development of many tissues(Caveney, n.d.). Gap junctions are expressed in nearly every type of tissue from cardiac cells to stem cells to neurons (Bauer et al., 2005; Moreno, 2004; Söhl et al., 2005; Starich et al., 2001).

Three different protein families are known to encode gap junctions or gap junction-like proteins: innexins, connexins, and pannexins(Sahu et al., 2015; Skerrett and Williams, 2017). Connexins are found exclusively in vertebrates whereas innexins are found exclusively in invertebrates (Bao et al., 2007). Pannexins do share some sequence homology with the other families and are found in both vertebrates and invertebrates. Pannexins have been hypothesized to be the evolutionary link between the connexin and innexin gene families (Beyer and Berthoud, 2018). Functionally, innexins and connexins create very similar gap junction channels despite very little DNA/Amino acid sequence homology (Evans and Martin, 2002; Landesman, n.d.; Moreno et al., 1995) While connexins/innexins hemichannels dock to form gap junctions, Pannexins primarily form hemichannels that do not dock, instead create intracellular hemichannels (Baranova et al., 2004; Sahu et al., 2015).

Low sequence homology leads to differences in channel structure between these convergent genes, connexins and innexins. Connexins have been shown to assemble with six connexon subunits creating a hexamer hemichannel (Lee et al., 2020; Unwin and Zampighi, 1980). Pannexin channels, thought to be the evolutionary link between innexins and connexins assemble with seven subunits (Michalski et al., 2020), and innexin forms octomer hemichannels (Oshima, 2017). Cells coupled with connexins exhibit smaller spacing in the electrical synapse (20–30 Å) and the spacing between channels is also smaller (75-95 Å) when compared to Innexins(30-40 Å and 90-120 Å respectively)(Skerrett and Williams, 2017). These differences likely lead to different biophysical properties as well.

The continued advance of sequencing technologies has resulted in an increase in the number of phyla that have published genomes and transcriptomes. This in turn has led to an increase in understanding of how connexin, innexin and pannexin gene families have evolved. Few cnidarians have entire genomes or transcriptomes published compared to other phyla, however some studies are beginning to reveal the presence of predicted innexin and pannexin genes. Transcriptome availability of the corals *Millepora alciconis* and *Millepora complanata* have predicted the presence of innexins and pannexins (Ortiz-González et al., 2017). Both the full genome and single cell transcriptome of the freshwater cnidarian *Hydra vulgaris* are published and reveal the presence of 15 predicted innexin genes and their isoforms (Chapman et al., 2010; Siebert et al., 2019). In addition, 27 innexin have been predicted in the *Clytia hemisphaerica* (Leclère et al., 2019). Large numbers of innexin genes within hydrozoans leads to the hypothesis that a gene duplication event has occurred. This is contrasted with anthozoans in that the genome of

the *Nematostella vectensis* has a single pannexin and no innexin genes (Putnam et al., 2007); this is similar to other available anemone innexin sequences.

Hydra exhibits a repertoire of behaviors, which are coordinated by specific neural circuits. These circuits along with their behavior outputs have been identified via whole animal calcium imaging (Dupre and Yuste, 2017); The contractile burst circuit (CB) coordinates contraction, rhythmic potential 1 (RP1) coordinates elongation and rhythmic potential 2 (RP2) coordinates radial contraction. Hydra INX2 expression correlates with the location of the CB circuit. It is presumed that innexins are also expressed in other hydra circuits. Innexins, specifically INX2, are postulated to play an important role in the coordination of this circuitry (Takaku et al., 2014) and the availability of the single cell transcriptome has helped elucidate the cell type expression patterns of hydra innexins.

There are five innexins expressed in the nervous system of hydra, four of which are expressed in circuitry outside of INX2, postulated to be the RP1 and RP2 circuits (Chapter 1). Differential expression may lead to different biophysical characteristics and regulatory regions within hydra innexins. This study aims to highlight the phylogeny and regulatory regions of hydra innexins expressed within the nervous system of the animal. Previous work (Welzel and Schuster, 2022) has explored the diversity of innexin- and pannexin-like genes across chordates and non chordates, including hydra and other cnidaria. The focus of that study was not to highlight cnidarian innexin regulation and phylogeny. Therefore, we bring forward the diversity and contrast the molecular differences between innexins expressed in the nervous system of hydra vulgaris and other Cnidarians.

Methods

Data source

Hydra innexins sequences were acquired from either the hydra genome portal or single cell transcriptome portal. The National Center for Biotechnology Information (NCBI) provides users with a large repertoire of tools and databases for biological data. Accession numbers for hydra innexins were available in the supplement of the hydra genome paper (Chapman et al., 2010) and were used to download sequences from NCBI ("Database resources of the National Center for Biotechnology Information," 2016). Some sequences were identified by using the Basic Local Alignment Sequencing Tool (BLAST) which queries sequences, in our case innexins, against the single cell transcriptome database to identify orthologous protein sequences. All other sequences were available to download from Welzel and Shuster (2022) (Welzel and Schuster, 2022) figure1 source data which were acquired by blasting innexin sequences against multiple databases to identify Cnidarian innexin and pannexin sequences. Starting with this data we applied a stringent filter to remove sequences that had a high identity to the volume regulated anion channel subunit LRRC8A, which is a gene closely related to innexins and pannexins but out of the scope of this study. Sequences were also queried against the protein family domain database (Pfam) to identify domains that are associated with pannesin or innexin sequences (El-Gebali et al., 2019). Sequences were removed if they had non-significant pfam domain identity to innexin or pannexin domains. This resulted in 81 Cnidarian pannexin- and innexin-like sequences which were used for this study.

Sequence Alignment and Analysis

Alignments were produced within MEGAX software (Kumar et al., 2018) using the MUSCLE alignment algorithm (Edgar, 2004) with the default parameters. Full length alignments were used for molecular topology prediction, N-glycosylation and phosphorylation searches. The TOPCONS web server was used to predict molecular topology (Tsirigos et al., 2015), the NetNGlyc - 1.0 server (Grupta et al., 2002) was used with default parameters to identify potential N Glycosylation sites and the NEtPhos 3.1 Server was used to identify possible phosphorylation sites (Blom et al., 1999).

Alignments were trimmed for phylogenetic analysis by using the ClipKit software (Steenwyk et al., 2020) to preserve sites which could provide essential information to tree building algorithms. Following Clipkit some manual trimming was performed to improve tree output. Phylogenetic analysis was performed on the CIPRES Scientific Gateway (Miller et al., 2011) using RAxML (Stamatakis, 2014) with 500 rapid bootstrap replicates and the LG+G protein substitution algorithm.

Results

Phylogenetic analysis

The dataset that was used in the previous study (Welzel and Schuster, 2022) looked at large scale phylogenetics to better elucidate the evolution of innnexins and pannexins across chordates and non chordates. Our goal is to highlight the diversity of innexins within cnidaria and better understand how innexins in hydra have evolved. To do so, we acquired sequences of 19 *Hydra vulgaris* innexin genes from the single cell transcriptome and 27 *Clytia hemisphaerica* innexin genes from the marimba genome database server. Innexin

genes from *Millepora comlanata* and *Millepora alcicornis*, *Nematostella vectensis, Edwardsiella carnea, Heliopora coerulea, Craterolophus convolvulus, Eleutherobia rubra, Siderastrea siderea,* were obtained from Welzel and Shuster (2022) (Welzel and Schuster, 2022). All sequences were aligned using the MUSCLE algorithm with default parameters and submitted to the CIPRES server for phylogenetic analysis with RaXML. The resulting maximum likelihood tree exhibited four groups of clearly identifiable innexin genes represented by innexins from *Hydra vulgaris, Clytia hemisphaerica, Millepora comlanata*, and *Millepora alcicornis* (Fig. 1). Hydra innexins are distributed between these four clades with innexins expressed in the nervous system split between the groups 2 and 4 (Fig. 1, asterisks). Also present within the tree is a clade of *Clytia* specific innexins (orange) and a clade of "innexin-like" sequences (light blue) consisting of *Edwardsiella carnea, Heliopora coerulea, Craterolophus convolvulus, Eleutherobia rubra,* and *Siderastrea siderea* (Fig. 1). Lastly, known pannexin sequences from *Pocillopora damicornis, Nematostella vectensis and Actinia tenebrosa* formed a single clade and the human *PANX1* gene is visible as the outgroup.

Hydra Molecular Topology

We generated an amino acid sequence alignment of 15 *hydra* innexins plus four of their isoforms using MegaX (Kumar et al., 2018) and the default Muscle parameters (Edgar, 2004). The alignment was used with TOPCONS sequence topology server to estimate the membrane topology of all hydra innexins (Tsirigos et al., 2015). Hydra innexins have four transmembrane domains resulting in three cytoplasmic loops and two extracellular loops (Fig. 2), characteristic of all known innexin, connexin, and pannexin genes (Evans and Martin, 2002; Phelan and Starich, 2001; Skerrett and Williams, 2017). The extracellular

loops contain known conserved cysteine residues typical of all innexins,as highlighted by the black asterisks in Fig.2. Notably, all *Hydra* innexins contain two additional cysteine residues in the first extracellular loop as indicated by the red asterisks (Fig. 2). Previously identified innexins of *C. Elegans* and *D. melanogaster* contain only two of these conserved cysteine residues in both extracellular loops (Bauer et al., 2005; Skerrett and Williams, 2017). Innexins of the terrestrial slug *Limax* have been characterized to contain 3 conserved cysteine residues in the first extracellular loop (Sadamoto et al., 2021) and are known to be essential in the formation of disulphide bonds between monomers (Maeda and Tsukihara, 2011).

Membrane Topology of Cnidarian Innexins

We then analyzed all sequences by using the TOPCONS membrane topology prediction web server (Tsirigos et al., 2015). Membrane topology of all cnidarian innexin and innexin like genes was characteristic of known connexin, pannexin and connexin genes(Evans and Martin, 2002; Skerrett and Williams, 2017). All sequences contained three cytoplasmic domains, four transmembrane domains, and two extracellular loops (Fig. 2-7). As first noted in Hydra innexins, sequence alignment revealed that all Cnidarian innexins of groups 1-4 contain two additional cysteine residues in the first extracellular loop (Fig. 3-6) indicating this as a characteristic unique to cnidarian innexins. Notably, the extra conserved cysteines are absent from all the “Innexin-Like” clade and Pannexin channels (Fig. 7).

N-Glycosylation within Innexin Sequences

Glycosylation is a post-translational modification that can impact a hemichannels ability to dock with another channel to form a gap junction and/or regulate a channel's

voltage dependence (Scott and Panin, 2014; Zhang et al., 1999). We used the NetNGlyc - 1.0 server to assess potential N-glycosylation sites of all sequences in the "Innexin-Like" and "Group 1-4 Cnidarian Innexin" clades in the maximum likelihood tree.

Not all innexins contained potential glycosylation sites across clades. "Group 1 Cnidarian Innexins" contain one conserved N-glycosylation site at N318 in the consensus alignment, with 6 out of the 9 sequences containing the site (Fig. 3). Relatively few glycosylation sites are observed in group 2 cnidarian innexins. One site is conserved among three of the group 2 innexins at N252 in the consensus sequence (Fig. 4). There are three innexins expressed within the nervous system of hydra in this clade and all of them contain N-glycosylation sites whereas these sites are absent in the two non-neural hydra innexins. The only conserved site within group 3 innexins is located at N240 within the Group 3 Cnidarian Innexins, primarily among both *Millepora* species and *Hydra INX12* (Fig. 5). Glycosylation sites were only observed in the first extracellular loop of Innexins within Group 4 (Fig. 6). This included INX10, 14 which are expressed in the nervous system of hydra but absent in INX4.

Most notably all hydra innexins expressed in the nervous system all had multiple identifiable N-glycosylation sites in the extracellular loops (Fig. 2 -6, Table 1), which is, as previously noted, a feature seen primarily in pannexin orthologs.

Phosphorylation of Neural Hydra Innexins

Phosphorylation is known to affect a gap junction channel assembly, stability and regulates biophysical properties (Lampe and Lau, 2000; Moreno et al., 1994). We identified

numerous phosphorylation sites within cnidarian innexins using the NEtPhos 3.1 Server to better predict how they might be regulated (ref). Phosphorylation sites for the following kinases were identified in groups 2 and 4 hydra innexins: PKA, PKC, CKI, CKII, CDC2, PKG, p38MAPK. We only identified phosphorylation sites within groups 2 and 4 as this is where hydra innexins expressed in the nervous system of hydra are distributed.

Phosphorylation sites were generally not well conserved in either group. Despite this, in "group 2 cnidarian innexins", two PKC phosphorylation sites within the first and second cytoplasmic domains are clearly identifiable along with one in the first extracellular loop(Fig. 4). This sites are conserved in all hydra innexins except INX2. INX2 exhibits unique phosphorylation topology with more PKA and CKII phosphorylation sites than all other hydra innexins, none of which appear to be conserved across hydra or other cnidarians (Fig. 4, Table 1).

Similarly, it appears that there are a large number of phosphorylation sites within sequences of group 4 but little conservation among sites (Fig. 6). Among the hydra innexins, one conserved PKC site is apparent in the first extracellular loop and one in the second extracellular loop. The second cytoplasmic domain contains a conserved PKC site located at S188 of the consensus alignment across all innexins of group 4. Notably, Innexin four has substituted this PKC site with CKI. Lastly, the PKA site is conserved among this group in the first cytoplasmic domain, but substituted with CDK5 within hydra INX4 sequences (Fig. 6). All phosphorylation sites within "Group 2 and 4 Cnidarian Innexins" are summarized in Table 1.

Discussion

This study highlights the phylogeny of innexins among cnidarians and explores conservation of phosphorylation and N-Glycosylation sites within hydra. Similar studies have been conducted highlighting low conservation of innexins across phyla but clear homology of pannexins between invertebrates and vertebrates (Welzel and Schuster, 2022; Yen and Saier, 2007). Cnidarian innexins among the hydrozoans clearly established four clades within the tree distinct from anthozoans. The numerous innexin genes within the hydrozoans indicate a gene duplication event while gene loss occurred in anthozoans.

All sequences in this study exhibited characteristic innexin membrane topology, four transmembrane domains and two extracellular loops. Notably however, additional cysteine residues in the first extracellular loop of hydrozoan innexins further indicates a likely gene duplication event that excluded anthozoans.

N-glycosylation could affect biophysical properties of gap junctions formed by any of these innexins. Pannexins have been shown to be regulated and prevented from forming gap junctions due to N-glycosylation (Penuela et al., 2014). N-glycosylation of TRPM8 channels affects voltage dependence in response to temperature, and sialylated N-glycans have been shown to regulate voltage gated ion channels (Scott and Panin, 2014). Our study verifies the presence of predicted N-glycosylation sites within neural hydra innexins, which could play a role in regulating hydra innexins. While we have shown that hydra innexins are capable of forming gap junctions and display voltage dependent properties in mammalian N2a cells, it is likely that proper post-translational N-glycosylation did not occur. It is therefore possible that innexins do not form gap junctions within the nervous system of hydra, and instead simply form intracellular hemichannels. Another possibility is that

channels are formed, with voltage dependent properties that are regulated via N-glycosylation. Furthermore, it is possible that glycosylation is important in membrane trafficking (Penuela et al., 2014) and could guide junctional plaque formation for large electrical synapses within hydra.

Phosphorylation is another important regulatory mechanism evident in connexin based gap junctions (Lampe and Lau, 2000; Moreno et al., 1994). We observed a significant number of phosphorylation sites within hydra innexins, mos of which are not well conserved, with the exception of some sites located within the PKC specific loci. Diversity of innexin phosphorylation may be a result of further gene duplication within the hydrozoans and could result in new functions associated with expression patterns within the hydra nervous system. Gene duplication and functional changes is not uncommon within the gap junction forming gene families (Eastman et al., 2006; Fushiki et al., 2010)

Membrane topology, N-glycosylation, and phosphorylation are all important in how innexins are regulated and form gap junctions. This study identifies and highlights the diversity of cnidarian, primarily hydrozoan, innexins and potential regulatory regions. The N-glycosylation and phosphorylation regions of hydra innexins will be important to explore in future studies as they can directly impact the results of the electrophysiology experiments seen in chapter 1. It remains to be seen whether hydra innexins are capable of forming gap junctions within hydra neurons but this study aims to help form hypotheses on whether this is possible.

Figures

Figure1. Cnidarian Innexin Phylogeny

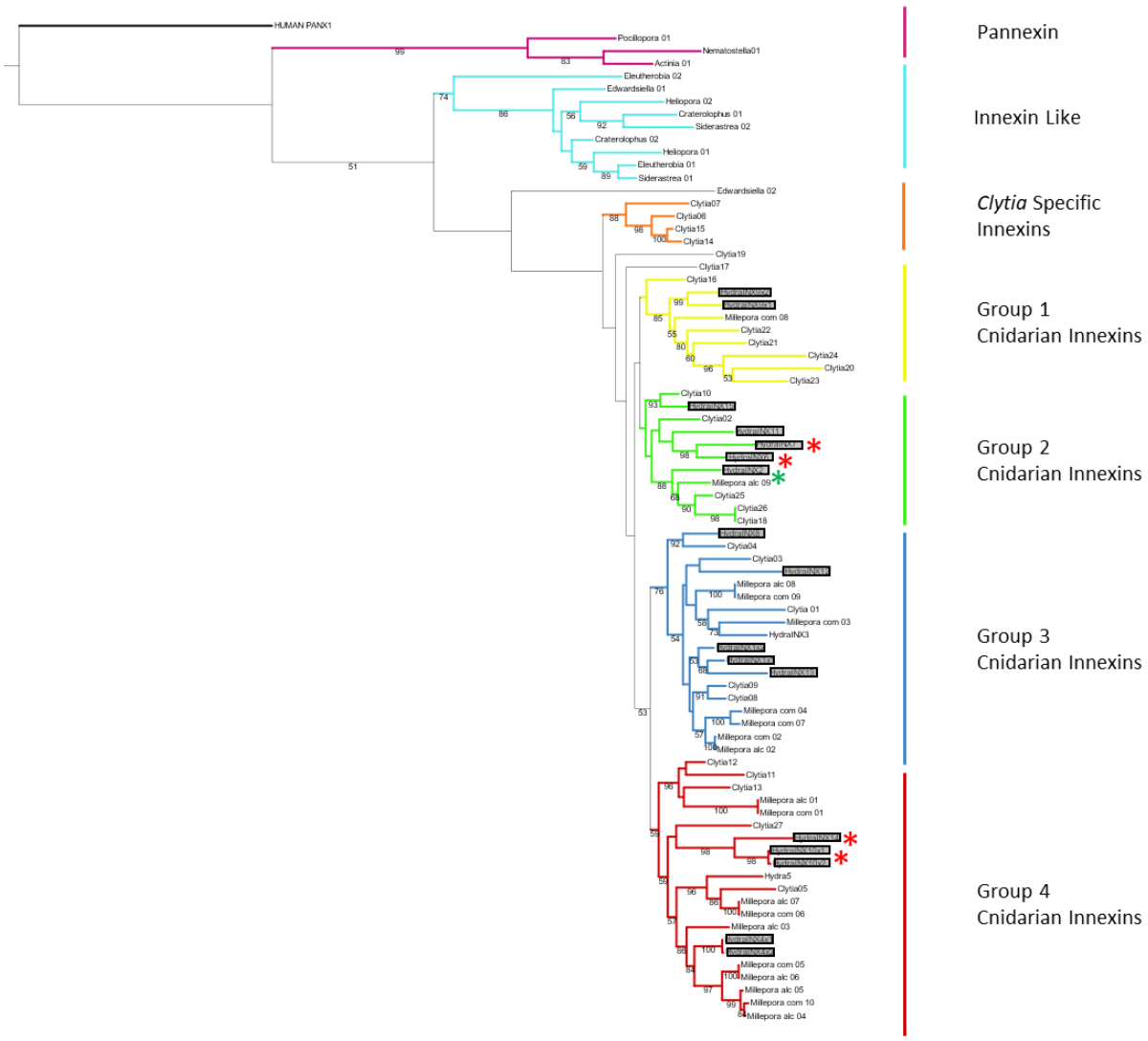

Figure 1. Cnidarian innexin phylogeny

Amino acid sequences from 11 different species of cnidarian were aligned using default MUSCLE parameters and used to create the maximum likelihood tree with 500 bootstrap replicates. Cnidarian innexins are distributed through seven identifiable clades with human PANX1 as an outgroup. Hydra innexins are highlighted in grey. Red asterisks indicate neural innexins of the EC3 cluster (single cell transcriptome) and green asterisks indicate INX2 of the EC1 cluster (single cell transcriptome).

Figure2. Hydra Innexin Membrane Topology and Sequence Structure

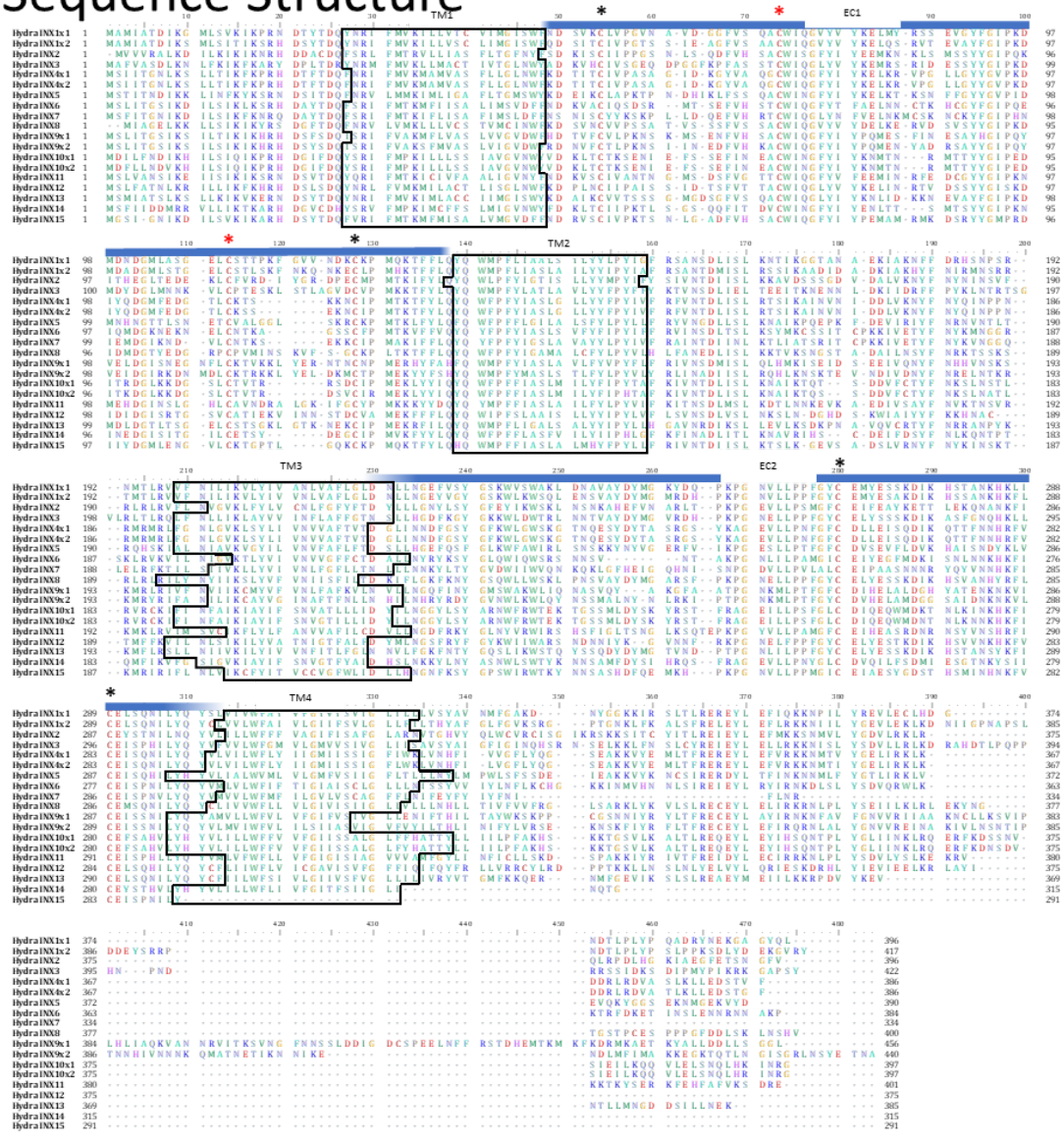

Figure 2. Hydra Innexin Membrane Topology and Sequence Structure.
Amino acid alignment of all hydra innexins. Four transmembrane domains are outlined in black. Blue bars indicate the extracellular loops. Conserved cysteine residues are identified by black asterisks; red asterisks indicate additional two cysteine residues present in hydra innexins.

Figure 3. Group 1 Cnidarian Innexins

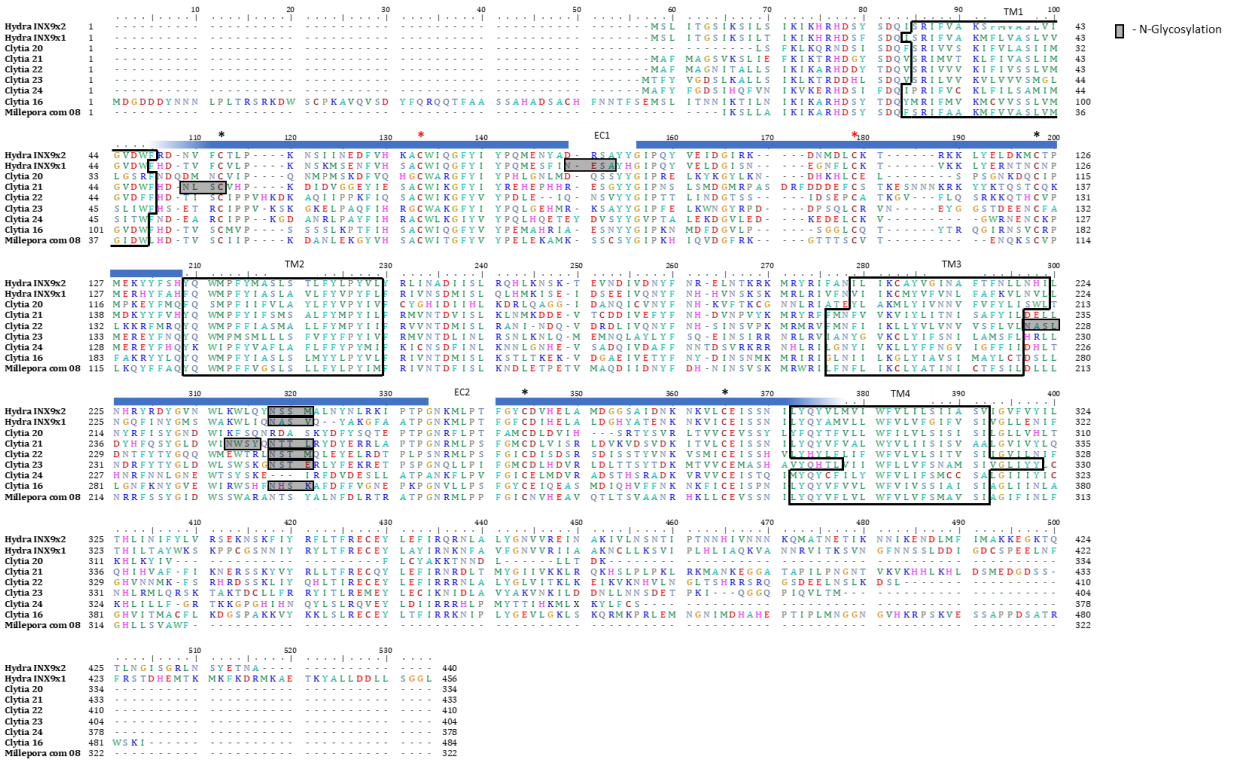

Figure 3. Group 1 cnidarian innexins.

Amino acid sequence alignment containing orthologous sequences from the clade "Group 1 Cnidarian Innexins". Four transmembrane domains are outlined in black. Blue bars indicate the extracellular loops. Conserved cysteine residues are identified by black asterisks; Red asterisks indicate additional two cysteine residues present in hydrozoan innexins. Highlighted by gray bars are N-glycosylation sites of which one site is conserved among the group at N318.

Figure 4. Group 2 Cnidarian Innexin

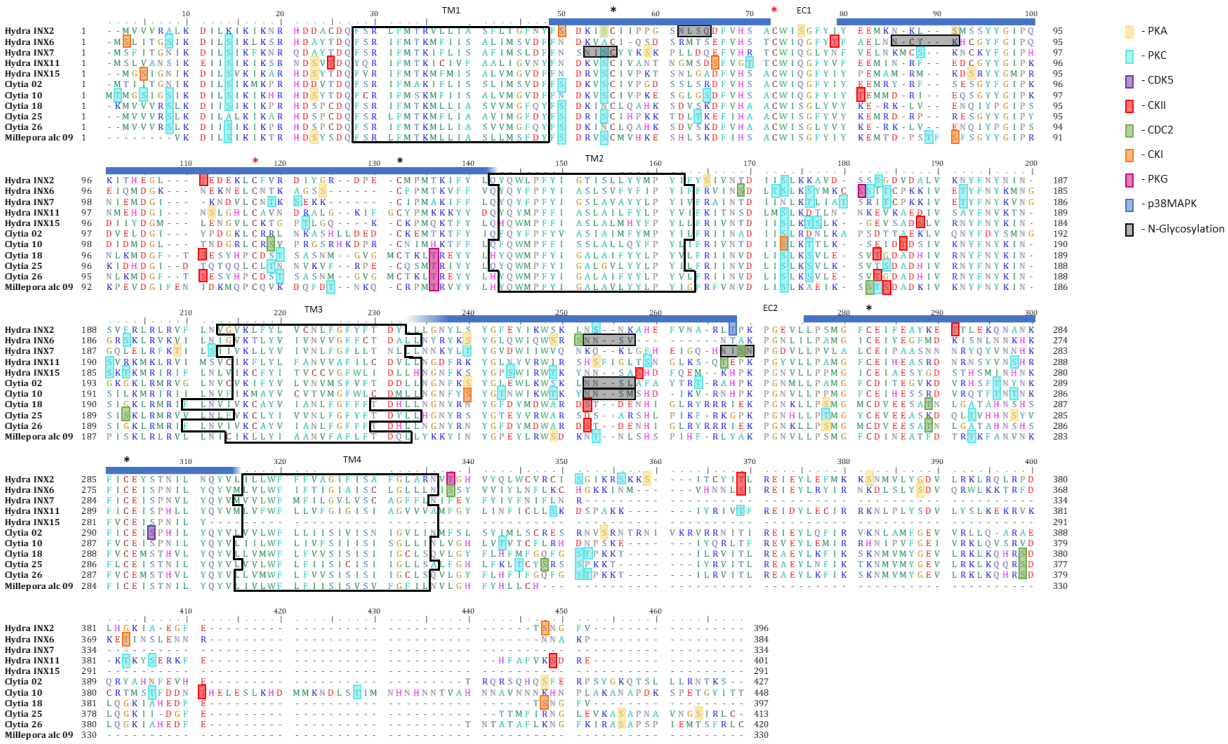

Figure 4. Group 2 cnidarian innexins.

Amino acid sequence alignment containing orthologous sequences from the clade “Group 2 Cnidarian Innexins” Three neural hydra innexins are distributed within this clade and therefore phosphorylation sites were predicted within this group. Sites are highlighted as indicated in the top right of the figure. Four transmembrane domains are outlined in black. Blue bars indicate the extracellular loops. Conserved cysteine residues are identified by black asterisks; Red asterisks indicate additional two cysteine residues present in hydrozoan innexins. Gray bars highlight dispersed N-glycosylation sites. Because this clade includes neural cluster innexins that were exogenously expressed in N2A cells, possible phosphorylation sites are also shown (see legend).

Figure 5. Group 3 Cnidarian Innexin

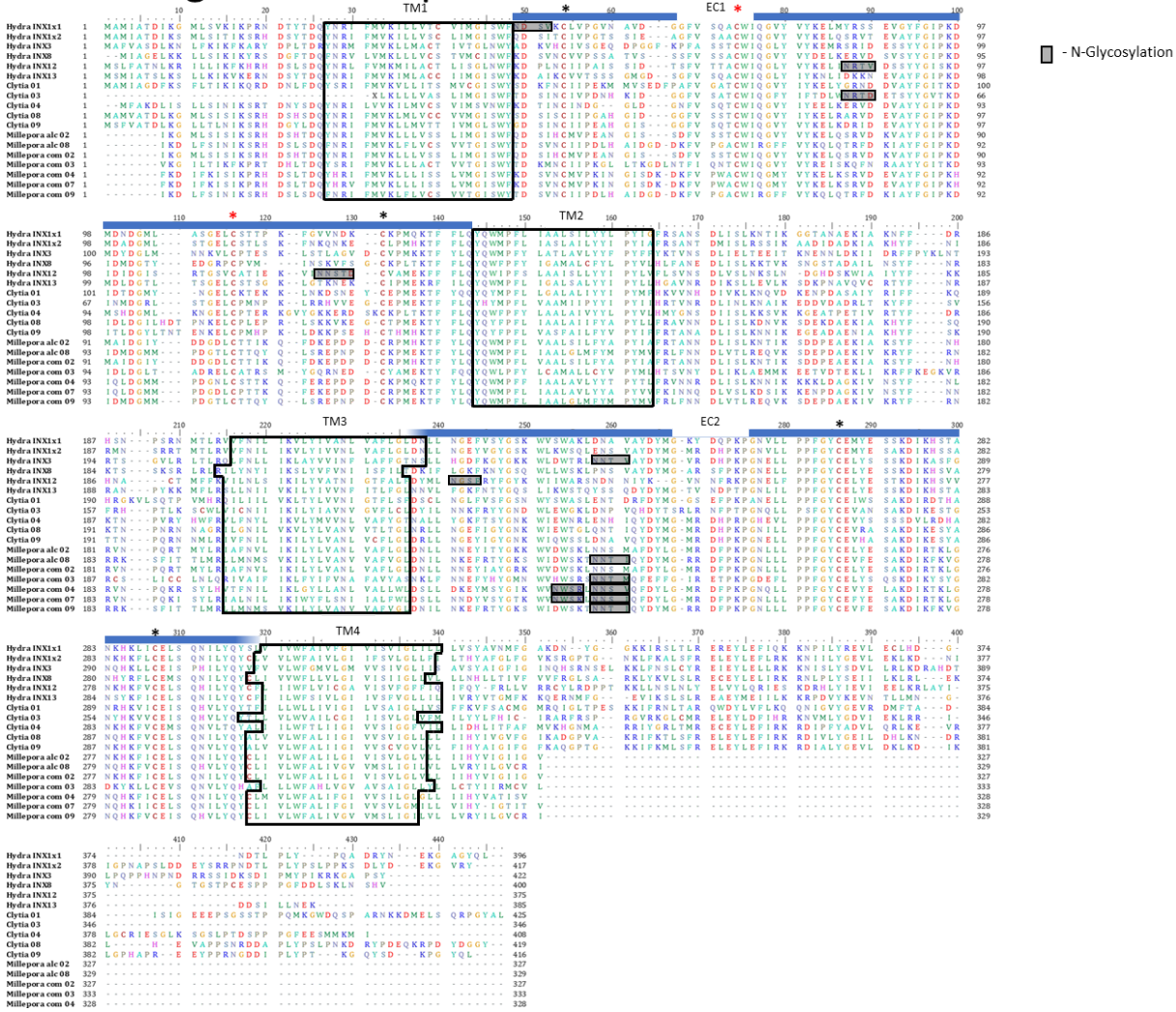

Figure 5. Group 3 cnidarian innexins.
Amino acid sequence alignment containing orthologous sequences from the clade "Group 3 Cnidarian Innexins". Four transmembrane domains are outlined in black. Blue bars indicate the extracellular loops. Conserved cysteine residues are identified by black asterisks; Red asterisks indicate additional two cysteine residues present in hydrozoan innexins. Highlighted by gray bars are N-glycosylation sites of which one site is conserved among a subgroup of orthologs at N258.

Figure 6. Group 4 Cnidarian Innexin

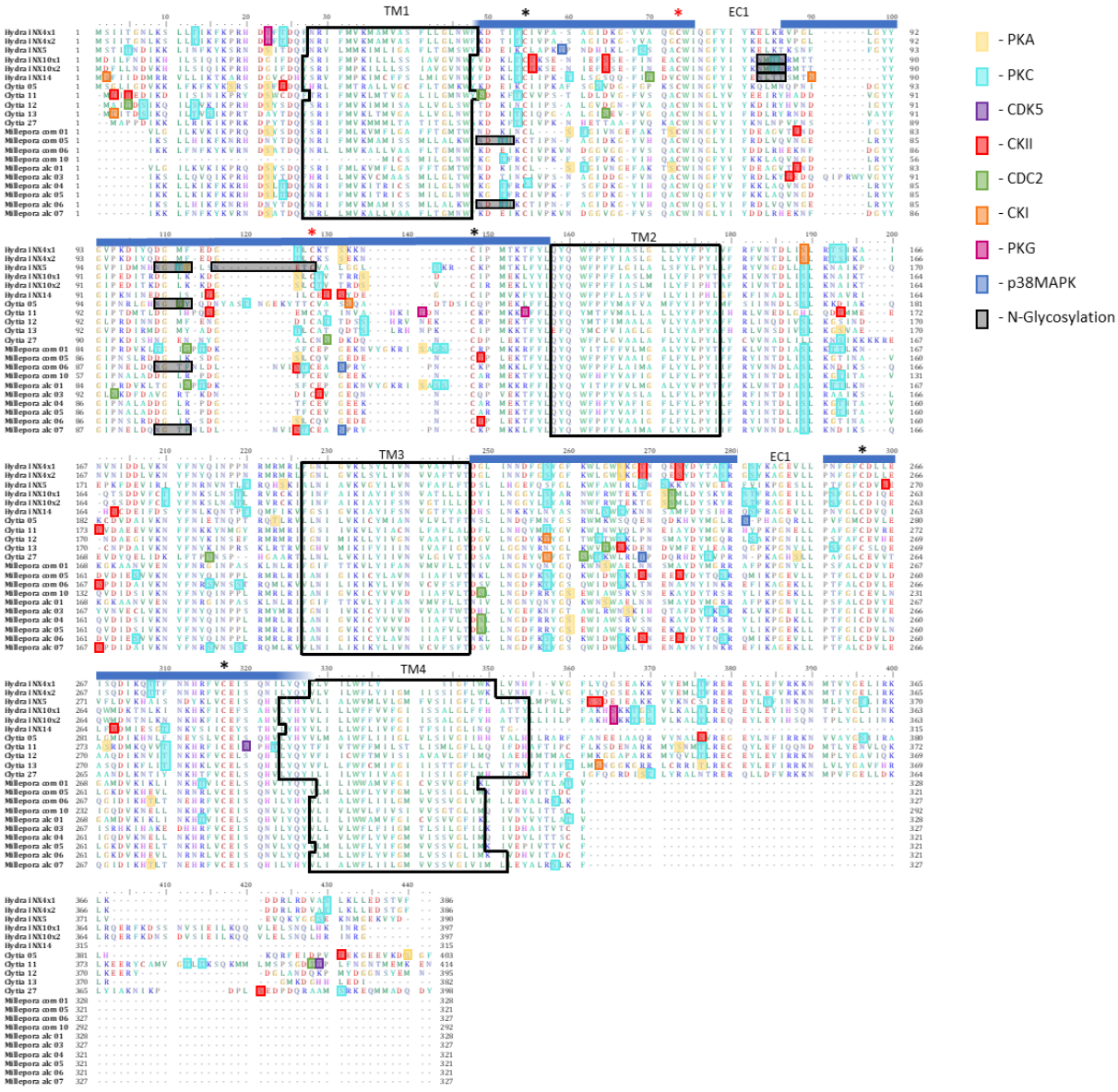

Figure 6. Group 4 cnidarian innexins.
Amino acid sequence alignment containing orthologous sequences from the clade "Group 4 Cnidarian Innexins" Two neural hydra innexins are distributed within this clade and therefore phosphorylation sites were predicted within this group. Sites are highlighted as indicated in the top right of the figure. Four transmembrane domains are outlined in black. Blue bars indicate the extracellular loops. Conserved cysteine residues are identified by black asterisks; Red asterisks indicate additional two cysteine residues present in hydrozoan innexins. Gray bars highlight dispersed N-glycosylation sites with minor conservation among some sequences in the alignment notably N83 among hydra neural

innexins. Because this clade includes neural cluster innexins that were exogenously expressed in N2A cells, possible phosphorylation sites are also shown (see legend).

Figure 7. Cnidarian Innexin-Like Sequences

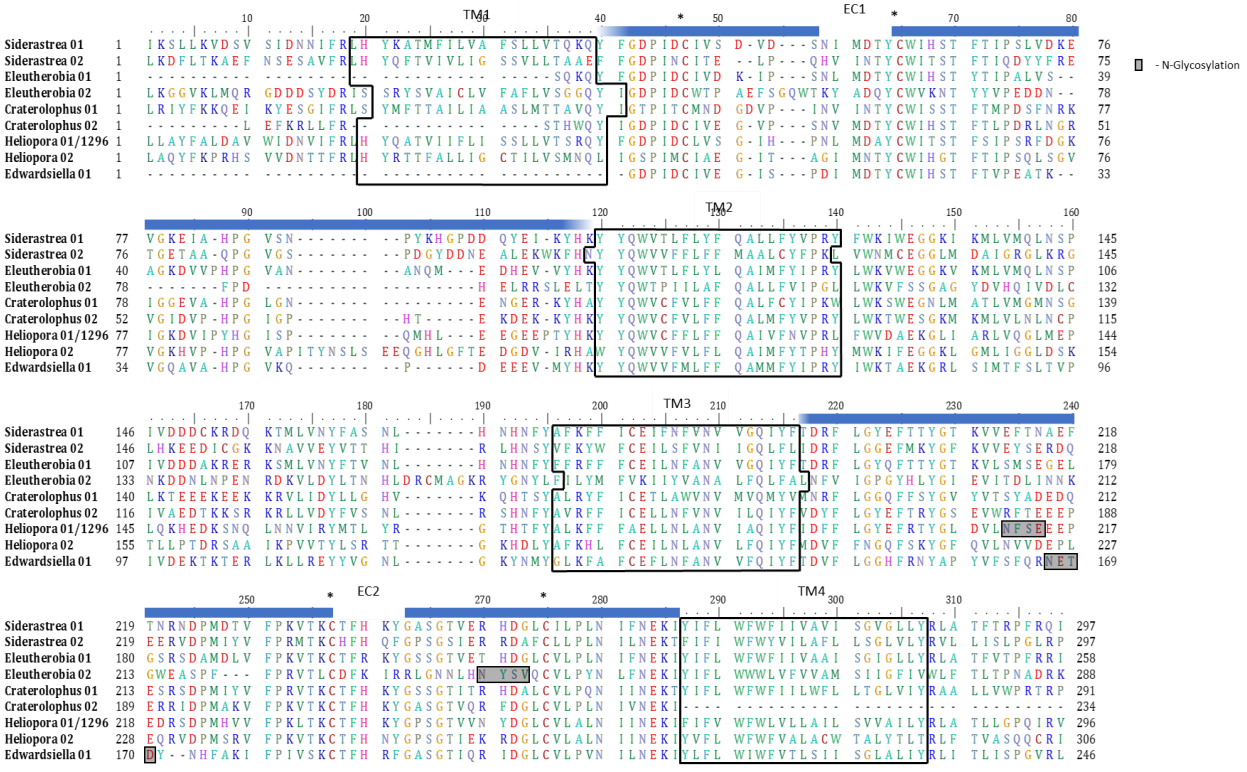

Figure 7. Cnidarian innexin-like sequences.
Amino acid sequence alignment containing orthologous sequences from the clade "Cnidarian innexin-like sequences". Four transmembrane domains are outlined in black. Blue bars indicate the extracellular loops. Conserved cysteine residues are identified by black asterisks; notably this group lacks the two additional conserved cysteines, typical of traditional innexins and pannexin sequences. Highlighted by gray bars are N-glycosylation sites, which is limited to three sites in this clade indicating more traditional or canonical innexin sequences.

Table 1. Phosphorylation and N-Glycosylation of Groups 2 and 4 Hydra Innexins

	Innexin	PKA	PKC	CKI	CKII	CDC2	PKG	P38mapk	N-glycosylation
Group 1 Cnidarian Innexins	*Hydra INX2*	S52, S73, S86, S154, S343, S 362	S162, S240, S335, S340	S48, S392	T103, S171, T275, T349,		T322	T252	N60, N320
	Hydra INX6	S116, S225, S234, S353	S7, S13, T157, T158, S161, 167, T169, T177, S188	S2, ST371	T77, S337	S154, S236, S313	S166		N83, N237, N310, N335
	Hydra INX7	S58, T195	S13, S87, T112, S114, T162, T166, T170, T178, S198, T226			S252			N51, N250
	Hydra INX11	S22, S105, S242	S13, T69, S164, S190, S248, S286, S337, T350, S 374, T383, S 386	S65	T24, S398	T255			N20
	Hydra INX15	S21, S88	S12, S52, T114, S 160, T163, S164, S185, T187, S228, T233	S3	S240	S173			
Group 4 Cnidarian Innexins	*Hydra INX4x1*	S113, S232	T13, T24, T108, T161, S162, S223, S245, S248, T274, T341, T376	S158,	T235, S239		T22		
	Hydra INX4x2	S113, S232	T13, T24, T108, T161, S162, S223, S245, S248, T274, T341, T376	S158,	T235, S239		T22		
	Hydra INX5	S22, T105, S194,	T5, S68, T104, S118, S162, T190, S239, S241, T354, T366, S380	S313	S269, S332, S333			T59	N20, N102, N108, N344
	Hydra INX10x1	S106, S114, S234, S305, T315,	T53, T83, T109, S157, T173, T182, S244, T245, T331, S333, T339	S63	T55,S64	S235	S328		N81, N176, N180, N374
	Hydra INX10x2	S106, S114, S234, S305, T315,	T53, T83, T109, S157, T173, T182, S244, T245, T331, S333, T339	S63	T55,S64	S235	S328		N81, N176, N180
	Hydra INX14		T53, T59, T157, T183, S227, T229, S245, T273	S2, S88	T104. T110, S111, S166, S266	T68			N81, N232, N312

Table 1. Phosphorylation and N-Glycosylation of Groups 2 and 4 Hydra Innexins
Light green row indicates INX2 of the EC1 cluster; pink cells represent innexins expressed in EC3 neural cluster of hydra single cell transcriptome. Grey cells indicate non neural innexins.

References

Bao L, Samuels S, Locovei S, Macagno ER, Muller KJ, Dahl G. 2007. Innexins form two types of channels. *FEBS Lett* **581**:5703–5708. doi:10.1016/j.febslet.2007.11.030

Baranova A, Ivanov D, Petrash N, Pestova A, Skoblov M, Kelmanson I, Shagin D, Nazarenko S, Geraymovych E, Litvin O, Tiunova A, Born TL, Usman N, Staroverov D, Lukyanov S, Panchin Y. 2004. The mammalian pannexin family is homologous to the invertebrate innexin gap junction proteins. *Genomics* **83**:706–716. doi:10.1016/j.ygeno.2003.09.025

Bauer R, Löer B, Ostrowski K, Martini J, Weimbs A, Lechner H, Hoch M. 2005. Intercellular Communication: the Drosophila Innexin Multiprotein Family of Gap Junction Proteins. *Chem Biol* **12**:515–526. doi:10.1016/j.chembiol.2005.02.013

Bennett MVL, Zukin RS. 2004. Electrical Coupling and Neuronal Synchronization in the Mammalian Brain. *Neuron* **41**:495–511. doi:10.1016/S0896-6273(04)00043-1

Beyer EC, Berthoud VM. 2018. Gap junction gene and protein families: Connexins, innexins, and pannexins. *Biochim Biophys Acta BBA - Biomembr* **1860**:5–8. doi:10.1016/j.bbamem.2017.05.016

Blom N, Gammeltoft S, Brunak S. 1999. Sequence and structure-based prediction of eukaryotic protein phosphorylation sites. *J Mol Biol* **294**:1351–1362. doi:10.1006/jmbi.1999.3310

Caveney S. n.d. The Role of Gap Junctions in Development 17.

Chapman JA, Kirkness EF, Simakov O, Hampson SE, Mitros T, Weinmaier T, Rattei T, Balasubramanian PG, Borman J, Busam D, Disbennett K, Pfannkoch C, Sumin N, Sutton GG, Viswanathan LD, Walenz B, Goodstein DM, Hellsten U, Kawashima T, Prochnik SE, Putnam NH, Shu S, Blumberg B, Dana CE, Gee L, Kibler DF, Law L, Lindgens D, Martinez DE, Peng J, Wigge PA, Bertulat B, Guder C, Nakamura Y, Ozbek S, Watanabe H, Khalturin K, Hemmrich G, Franke A, Augustin R, Fraune S, Hayakawa E, Hayakawa S, Hirose M, Hwang JS, Ikeo K, Nishimiya-Fujisawa C, Ogura A, Takahashi T, Steinmetz PRH, Zhang X, Aufschnaiter R, Eder M-K, Gorny A-K, Salvenmoser W, Heimberg AM, Wheeler BM, Peterson KJ, Böttger A, Tischler P, Wolf A, Gojobori T, Remington KA, Strausberg RL, Venter JC, Technau U, Hobmayer B, Bosch TCG, Holstein TW, Fujisawa T, Bode HR, David CN, Rokhsar DS, Steele RE. 2010. The dynamic genome of Hydra. *Nature* **464**:592–596. doi:10.1038/nature08830

Choi U, Wang H, Hu M, Kim S, Sieburth D. 2021. Presynaptic coupling by electrical synapses coordinates a rhythmic behavior by synchronizing the activities of a neuron pair. *Proc Natl Acad Sci* **118**:e2022599118. doi:10.1073/pnas.2022599118

Database resources of the National Center for Biotechnology Information. 2016. . *Nucleic Acids Res* **44**:D7–D19. doi:10.1093/nar/gkv1290

Dupre C, Yuste R. 2017. Non-overlapping Neural Networks in Hydra vulgaris. *Curr Biol* **27**:1085–1097. doi:10.1016/j.cub.2017.02.049

Eastman SD, Chen TH-P, Falk MM, Mendelson TC, Iovine MK. 2006. Phylogenetic analysis of three complete gap junction gene families reveals lineage-specific duplications and highly supported gene classes. *Genomics* **87**:265–274. doi:10.1016/j.ygeno.2005.10.005

Edgar RC. 2004. MUSCLE: multiple sequence alignment with high accuracy and high throughput. *Nucleic Acids Res* **32**:1792–1797. doi:10.1093/nar/gkh340

El-Gebali S, Mistry J, Bateman A, Eddy SR, Luciani A, Potter SC, Qureshi M, Richardson LJ, Salazar GA, Smart A, Sonnhammer ELL, Hirsh L, Paladin L, Piovesan D, Tosatto SCE, Finn RD. 2019. The Pfam protein families database in 2019. *Nucleic Acids Res* **47**:D427–D432. doi:10.1093/nar/gky995

Evans WH, Martin PEM. 2002. Gap junctions: structure and function (Review). *Mol Membr Biol* **19**:121–136. doi:10.1080/09687680210139839

Fushiki D, Hamada Y, Yoshimura R, Endo Y. 2010. Phylogenetic and bioinformatic analysis of gap junction-related proteins, innexins, pannexins and connexins. *Biomed Res* **31**:133–142. doi:10.2220/biomedres.31.133

Gupta R, Brunak S. 2002.Prediction of glycosylation across the human proteome and the correlation to protein function. Pac Symp Biocomput. 2002;:310-22. PMID: 11928486

Kumar S, Stecher G, Li M, Knyaz C, Tamura K. 2018. MEGA X: Molecular Evolutionary Genetics Analysis across Computing Platforms. *Mol Biol Evol* **35**:1547–1549.

doi:10.1093/molbev/msy096

Lampe PD, Lau AF. 2000. Regulation of Gap Junctions by Phosphorylation of Connexins. *Arch Biochem Biophys* **384**:205–215. doi:10.1006/abbi.2000.2131

Landesman Y. n.d. Innexin-3 forms connexin-like intercellular channels 6.

Leclère L, Horin C, Chevalier S, Lapébie P, Dru P, Peron S, Jager M, Condamine T, Pottin K, Romano S, Steger J, Sinigaglia C, Barreau C, Quiroga Artigas G, Ruggiero A, Fourrage C, Kraus JEM, Poulain J, Aury J-M, Wincker P, Quéinnec E, Technau U, Manuel M, Momose T, Houliston E, Copley RR. 2019. The genome of the jellyfish Clytia hemisphaerica and the evolution of the cnidarian life-cycle. *Nat Ecol Evol* **3**:801–810. doi:10.1038/s41559-019-0833-2

Lee H-J, Jeong H, Hyun J, Ryu B, Park K, Lim H-H, Yoo J, Woo J-S. 2020. Cryo-EM structure of human Cx31.3/GJC3 connexin hemichannel. *Sci Adv* **6**:eaba4996. doi:10.1126/sciadv.aba4996

Maeda S, Tsukihara T. 2011. Structure of the gap junction channel and its implications for its biological functions. *Cell Mol Life Sci* **68**:1115–1129. doi:10.1007/s00018-010-0551-z

Michalski K, Syrjanen JL, Henze E, Kumpf J, Furukawa H, Kawate T. 2020. The Cryo-EM structure of pannexin 1 reveals unique motifs for ion selection and inhibition. *eLife* **9**:e54670. doi:10.7554/eLife.54670

Miller MA, Pfeiffer W, Schwartz T. 2011. The CIPRES science gateway: a community resource for phylogenetic analysesProceedings of the 2011 TeraGrid Conference on Extreme Digital Discovery - TG '11. Presented at the the 2011 TeraGrid Conference. Salt Lake City, Utah: ACM Press. p. 1. doi:10.1145/2016741.2016785

Moreno A. 2004. Biophysical properties of homomeric and heteromultimeric channels formed by cardiac connexins. *Cardiovasc Res* **62**:276–286. doi:10.1016/j.cardiores.2004.03.003

Moreno AP, Laing JG, Beyer EC, Spray DC. 1995. Properties of gap junction channels formed of connexin 45 endogenously expressed in human hepatoma (SKHep1) cells. *Am J Physiol-Cell Physiol* **268**:C356–C365. doi:10.1152/ajpcell.1995.268.2.C356

Moreno AP, Sáez JC, Fishman GI, Spray DC. 1994. Human connexin43 gap junction channels. Regulation of unitary conductances by phosphorylation. *Circ Res* **74**:1050–1057. doi:10.1161/01.RES.74.6.1050

Ortiz-González IC, Rivera-Vicéns RE, Schizas NV. 2017. De novo transcriptome assembly of the hydrocoral Millepora alcicornis (branching fire coral) from the Caribbean. *Mar Genomics* **32**:27–30. doi:10.1016/j.margen.2016.11.005

Oshima A. 2017. Structure of an innexin gap junction channel and cryo-EM sample preparation. *Microscopy* **66**:371–379. doi:10.1093/jmicro/dfx035

Penuela S, Simek J, Thompson RJ. 2014. Regulation of pannexin channels by post-translational modifications. *FEBS Lett* **588**:1411–1415.

doi:10.1016/j.febslet.2014.01.028

Phelan P, Starich TA. 2001. Innexins get into the gap. *BioEssays* **23**:388–396. doi:10.1002/bies.1057

Putnam NH, Srivastava M, Hellsten U, Dirks B, Chapman J, Salamov A, Terry A, Shapiro H, Lindquist E, Kapitonov VV, Jurka J, Genikhovich G, Grigoriev IV, Lucas SM, Steele RE, Finnerty JR, Technau U, Martindale MQ, Rokhsar DS. 2007. Sea Anemone Genome Reveals Ancestral Eumetazoan Gene Repertoire and Genomic Organization. *Science* **317**:86–94. doi:10.1126/science.1139158

Sadamoto H, Takahashi H, Kobayashi S, Kondoh H, Tokumaru H. 2021. Identification and classification of innexin gene transcripts in the central nervous system of the terrestrial slug Limax valentianus. *PLOS ONE* **16**:e0244902. doi:10.1371/journal.pone.0244902

Sahu G, Sukumaran S, Bera AK. 2015. Pannexins form gap junctions with electrophysiological and pharmacological properties distinct from connexins. *Sci Rep* **4**:4955. doi:10.1038/srep04955

Scott H, Panin VM. 2014. The role of protein N-glycosylation in neural transmission. *Glycobiology* **24**:407–417. doi:10.1093/glycob/cwu015

Siebert S, Farrell JA, Cazet JF, Abeykoon Y, Primack AS, Schnitzler CE, Juliano CE. 2019. Stem cell differentiation trajectories in *Hydra* resolved at single-cell resolution. *Science* **365**:eaav9314. doi:10.1126/science.aav9314

Skerrett IM, Williams JB. 2017. A structural and functional comparison of gap junction channels composed of connexins and innexins: Structural and Functional Comparison of Gap Junction Channels. *Dev Neurobiol* **77**:522–547. doi:10.1002/dneu.22447

Söhl G, Maxeiner S, Willecke K. 2005. Expression and functions of neuronal gap junctions. *Nat Rev Neurosci* **6**:191–200. doi:10.1038/nrn1627

Stamatakis A. 2014. RAxML version 8: a tool for phylogenetic analysis and post-analysis of large phylogenies. *Bioinformatics* **30**:1312–1313. doi:10.1093/bioinformatics/btu033

Starich T, Sheehan M, Jadrich J, Shaw J. 2001. Innexins in C. elegans. *Cell Commun Adhes* **8**:311–314. doi:10.3109/15419060109080744

Steenwyk JL, Buida TJ, Li Y, Shen X-X, Rokas A. 2020. ClipKIT: A multiple sequence alignment trimming software for accurate phylogenomic inference. *PLOS Biol* **18**:e3001007. doi:10.1371/journal.pbio.3001007

Takaku Y, Hwang JS, Wolf A, Böttger A, Shimizu H, David CN, Gojobori T. 2014. Innexin gap junctions in nerve cells coordinate spontaneous contractile behavior in Hydra polyps. *Sci Rep* **4**:3573. doi:10.1038/srep03573

Tsirigos KD, Peters C, Shu N, Käll L, Elofsson A. 2015. The TOPCONS web server for consensus prediction of membrane protein topology and signal peptides. *Nucleic Acids Res* **43**:W401–W407. doi:10.1093/nar/gkv485

Unwin PNT, Zampighi G. 1980. Structure of the junction between communicating cells. *Nature* **283**:545–549. doi:10.1038/283545a0

Welzel G, Schuster S. 2022. Connexins evolved after early chordates lost innexin diversity. *eLife* **11**:e74422. doi:10.7554/eLife.74422

Yen MR, Saier MH. 2007. Gap junctional proteins of animals: The innexin/pannexin superfamily. *Prog Biophys Mol Biol* **94**:5–14. doi:10.1016/j.pbiomolbio.2007.03.006

Zhang Y, Hartmann HA, Satin J. 1999. Glycosylation Influences Voltage-Dependent Gating of Cardiac and Skeletal Muscle Sodium Channels. *J Membr Biol* **171**:195–207. doi:10.1007/s002329900571

Chapter 5: Regenerating circuits in Hydra vulgaris

Introduction

The central problem of neuroscience is to understand how neural circuitry produces behaviors. While this is an extremely complex problem in the vertebrate CNS, the brains of invertebrates, particularly cnidarians, offer an opportunity to discover fundamental computational principles through the study of their simpler nervous systems. Cnidarians, which are sister to bilaterians, possess a nerve net as opposed to a centralized nervous system. Advances in transgenic technologies have allowed the development of a transgenic freshwater cnidarian, *Hydra vulgaris*, which expresses GCaMP6 specifically in the neurons of the animal. Activation of the nerve net, in turn, induces real time fluorescent signals, via GCaMP6 (Dupre and Yuste, 2017). This allows neural activity and behavior to be observed simultaneously in a moving animal. Given its relatively simple anatomical structure and a recently completed genetic screen of its neuron types (Siebert et al., 2019), Hydra is an ideal model system in which to understand the activity patterns of a complete neural circuit, the structural and biophysical mechanisms underlying that activity, and the behavior it elicits.

Behavior in *Hydra* has been explored for two centuries, and comprises stimulated and spontaneous behaviors (Han et al., 2018). The development of a *Hydra* line with GCaMP in all neurons, showing $[Ca]_i$ increases during firing, allows us to observe activity in all neurons simultaneously, elucidating circuit-based behaviors. Light stimulation causes

activation of the ectodermal RP1 (rhythmic potential) circuit, in which dark-adapted *Hydra* elongate the body towards light, while engagement of the sub tentacle network causes "nodding", in which the animals turn their tentacles towards the light source (Passano and Mccullough, 1963). Endodermal contractions move the food bolus for digestion and control de-glutination, much like the vertebrate gut, *via* radial contractions elicited by the endodermal RP2 circuit (Shimizu et al., 2004). The mouth opens via induction from RP2 and the body column undergoes radial contraction to expel waste (Carter et al., 2016). Spontaneous behaviors include periodic longitudinal contractions of the body column, mediated by the contraction burst circuit (CB), an ectodermal nerve net independent of the RP1 circuit (Dupre and Yuste, 2017). Thus, the behaviors of this simple organism can be characterized by discrete functional units, some of which overlap (Zacharias et al., 2004; Chapman et al. 2010; Han et al. 2018)(ref downloads).

Large numbers of interstitial stem cells exist in the body column of the animal allowing for remarkable regenerative capabilities (Heimfeld and Bode, 1985). Regeneration within hydra has been well documented. The animal can regenerate a completely new hypostome and/or peduncle within four days post bisection (Vogg et al., 2019). Furthermore the animal can undergo dissociation and completely regenerate, synchronizing its nervous system and re coordinating its behaviors (Lovas and Yuste, 2021). This ability raises the question as to how a circuit regenerates after bisection. In this study we use *Hydra* as a platform to understand how circuit behaviors regenerate after bisection, due to our ability to image every neuron simultaneously, the simple structure of its nervous system, and the incredible regenerative properties of the animal.

Methods

Hydra cultures and imaging.

All Hydra lines were maintained at 18℃ and fed newly hatched *Artemia nauplii* two to three times per week. Hydra expressing the calcium indicator GCaMP6 in the nervous system of the animal were used for imaging experiments. We used a modified imaging preparation from (Dupre and Yuste, 2017). All imaging took place under a ZEISS Axio Zoom.V16 equipped with Zeiss AxioCam 506 monochrome camera for fluorescent imaging, PlanNeoFluar Z 2.3X objective lens and a GFP fluorescent filter set. The imaging arena consisted of a microscope slide, 50 to 100 μm spacer and a cover slip. The use of the spacer allowed us to keep the animals in focus by preventing motion in the z direction while still allowing free motion in the x and y directions. Animals were recorded in the arena for 30-60 minutes at a sampling rate of 4 to 10 frames per second. After control imaging the animal was bisected as symmetrically as possible separating the hypostome from the peduncle. Each half was imaged separately one after the other for 30- 60 minutes every 24 hours. The Imaging pipeline can be seen in Figure 1.

Video analysis.

Analysis was adapted from chapter 2. Here we use image analysis to estimate integrated fluorescence in the neuronal GCAMP lines as well as characterize Hydra's body configuration. Acquired movies were processed using a combination of ImageJ (Schneider et al., 2012), the Icy Imaging software suite (de Chaumont et al., 2012), DeepLabCut (Mathis et al., 2018) and custom scripts. ImageJ was used to adjust the contrast from background noise which is essential to accurately extract contours of the Hydra. Noise was reduced using median filtering (despeckle plugin). Icy Imaging was then used to extract the

contours of individual frames using the Active Contours plugin. We can then integrate fluorescence signals within the contour. We used DeepLabCut to track four well-identified body locations: the center of the hypostome, the center of the peduncle, and the points of intersection of the left- and rightmost tentacles with the body column (the “armpits”). The tracked “armpits” from DeepLabCut were used to exclude the tentacles from data acquired with Icy active contours. The peduncle was then used to segment contours. Lastly, connecting the midpoints of segmentation allowed us to extract the curved midline of the Hydra body in each frame.

Event analysis from fluorescent intensity

Due to bleaching from over-exposure, fluorescence intensity linearly decreases over time. This effect does not reflect a meaningful change in Hydra’s neural activity. We remove it by subtracting from the data the 1-D polynomial that minimizes least squared error in the overall body fluorescence. In frames in which non-hydra material appears, ImageJ was used to create a Z-Projection for the entire video based on maximum pixel intensity. A polygon was drawn to contour the hydra, excluding any foreign bodies, and fluorescent integration was used only within the polygon for each frame. Occasionally, the camera perspective shifts part-way through the video inducing a fluorescent artifact, a non-neural associated spike in fluorescent intensity. To correct for this we:

(a) x_b.

(b) Calculate the difference in fluorescence between frames x_b and x_a -1. Subtract this difference from every frame i > x_b.

(c) For every frame i between x_a and x_b, calculate the difference in fluorescence between i and x_a, and subtract it from frame i.

Finally, the midline length and fluorescence is smoothed using a Savinsky-Golay filter and used for peak detection to identify CB vs RP activations via custom python script.

Results

Healthy, non-budding, animals were selected for bisection experiments in an effort to understand how circuits and behavior are disrupted and repaired in *Hydra.* Prior to bisection, animals were imaged for 30 minutes to one hour to gather baseline circuit activity and behavior.

Prebisect

We first analyzed movies to integrate fluorescent intensity and determine the length of the animal. This data revealed regular intervals of spontaneous contractions and elongations (Fig. 2A) Large fluorescent spikes marked by red x's in Figure 2A are associated with a rapid decrease in the length of the animal while smaller peaks marked by black x's in Figure 2A correlate with an initial rapid rebound lengthening then slower passive elongation. The spontaneous activity of both the CB and RP circuits occurs in a semi-regular, and orderly fashion.

During contraction events the CB circuit rapidly activates in quick succession which keeps the animal in a contracted state. We calculated the number of events within a contraction event to better understand how the CB circuit was specifically affected after bisection and during regeneration. Baseline results revealed that intact animals average ~8 CB events per contraction, with a minimum of two events and a maximum of 15 events within a contraction (Fig. 3A)

RP events were also analyzed in similar fashion with an average of 7 RP's between contraction events. Most elongation periods contained 2.5 RP events to 10 RP events. A single period contains 16 events (Fig. 4A).

0 hour

After baseline movies were acquired, the animal was bisected to separate the hypostomal and peduncular halves, attempting to keep each half the same length. Hypostomal halves were imaged independently and successively for 30 minutes to one hour.

Peduncle.

Dramatic changes in circuit activity and behavior were immediately seen in the peduncular halves. Correlation of integrated fluorescence and length of the animal revealed a number of contraction events seen near the beginning of imaging and then a long elongation event with many frequent RP events (Fig. 2C). CB circuit activity is also dramatically reduced. An average of 2.5 events per contraction occurred in the peduncular half compared to 8 in the baseline intact animal. CB events ranged from one event per contraction to 5 events per contraction, though only one contraction contained 5 events (Fig. 3C). Fewer contractions resulted in longer elongation periods which in turn results in more RP events. About 10 events were seen in the periods between contractions near the beginning of the video and nearly 100 were recorded during the long elongation period (Fig. 4C)

Hypostome

Little change is seen in the hypostomal half after bisection. The integrated fluorescence/length graph displays regular periodic contraction and elongation events similar to those seen in the intact animal (Fig. 2B). Occasionally the length appears to be maximized, likely due to an artifact in the imaging or bisection technique. The hypostomal

animal could have flipped to a vertical position preventing elongation or encountered an edge in the arena. CB and RP activity analysis also reveals nearly identical circuit behavior (Fig. 3 B, Fig. B). Frequency of CB events per contraction and frequency of RP events during elongation were the same as the pre-bisected intact animal. The range of the number of events observed was reduced in the 0 hour hypostomal animal compared to the intact animal (Fig. 3B, Fig. B) which could indicate that the peduncle has some role in modulating pacemaker activity which, based on 0hour, data would appear to be located in the hypostome.

48 hours

A substantial change in circuit activity and behavior was not observed until 48 hours after bisection. Prior to 48 hours and beyond, the hypostomal behavior did not change and only the peduncular ring of neurons became visible via calcium imaging.

Peduncle

At 48 hours after bisection we began to observe more frequent contractions and a decrease in the duration of elongation periods. The fluorescence/length correlation displays 8 contraction events with multiple CB's (Fig. 2E). The average number of CB events per contraction increases to what we observed in the intact animal with ~10 events per contraction. This ranged from 5 events to 12 events with contractions containing 17 CB events, indicating that circuit rewiring and regeneration is occurring (Fig. 3E). The rate of RP events also began to return to that in the control animal. The average number of RP events per elongation period decreased to ~15 from 20 at 0 hour (Fig. 4E). This number (15) of events was still greater than in the intact animal which exhibited ~7 events per

elongation event. This could be due to either longer elongation periods or more rapid RPs during those elongation periods.

Hypostome

At 48 hours post bisection the hypostomal half resumed normal periodic contraction/elongation events that appeared to decrease in frequency over the hour-long imaging time (Fig. 2D). While this differs from the baseline, we have observed this behavior in intact animals before and do not expect this to be a result of bisection and regeneration. CB circuit activity undergoes a slight change with ~11 CB events per contraction, but the range of CB events per contraction was broad as in the baseline experiment (Fig. 3 A,D). We observed very little change in the number of RP events during elongation compared to intact and 0 hour checkpoints (Fig. 4D)

72 hours

Peduncle

At 72 hours post bisection integrated fluorescence/length graph displays a return to nearly normal behavior in the peduncular half hydra. Many more frequent contractions are observed with semi-regular elongation periods between contractions (Fig. 2G) CB activity returns to nearly identical levels seen in the intact animal with ~7 CB events per contraction, with the range of events per contraction reduced only slightly. 2-10 CB events per contraction vs 2 - 15 in the intact animal (Fig. 3 A,G). The number of RP events per elongation event at this point is very similar to the intact animal with ~7RPs per elongation. However the range is slightly different with a number of elongations containing 20 to 25 RP's (Fig. 4G)

Hypostome

At this 72 hour checkpoint the Hypostome is nearly identical to the 48 hour checkpoint with semi-regular contractions and elongations. Frequent contractions are seen near the beginning of the experiment and become more sparse as imaging progresses (Fig. 2 D,F). Both the average number and range of CB events per contraction are identical to the intact animal, further indicating that bisection has little effect on contractions and CB circuit activity (Fig. 3A,F). RP events are also once again very similar to what was observed in the intact animal and at other checkpoints (Fig. 4F)

Discussion

The results presented in this study raise interesting questions that require more thorough study, and represent a starting point to build upon. A single representative experiment is presented in figures 2 and 3 which aligns with what we have seen in other experiments summarized in figure 5. Bisected animals exhibit substantial differences between the intact/hypostomal and peduncular halves. Hypostome and intact animals behavior is nearly identical and it would appear that the removal of the peduncular ring does not prevent the animal from undergoing semi-regular contraction events. It is possible that there is a significant reduction in the range of CB events immediately after bisection. All contractions have CB event numbers that are more closely centered around the average, 8, CB events per contraction. This may indicate that the peduncle does have a role in modulating or regulating CB activity but is not the pacemaker..

It is evident that after the peduncle is separated from the hypostome, the peduncular half loses a signaling mechanism to initiate contractions since the frequency of

spontaneous contractions is reduced (Fig. 4). When the peduncle does contract, the CB circuit activation is infrequent, preventing full contraction events that contain multiple CB records (Fig. 3C). Hydra's ability to contract without pacemaking input could be the result of a sensory stimulus inducing a contraction similar to those seen in nerve free hydra (Campbell et al., 1976). Furthermore, hydra exposed to an antibody block of INX2, which may form electrical synapses in the CB circuit, were still able to contract from stimulus, but the number of CB events per contraction was reduced (Takaku et al., 2014).

We are clearly able to show that a disruption of the CB circuit occurs when the hypostome is removed and that the circuit is able to rebuild behavior within 48 hours. It has been noted in extracellular ectodermal recordings that electrical signals travel from the hypostome to the peduncle (Kass-Simon and Passano, 1978) which the results of our experiments support. However this study does not investigate how the circuit rebuilds itself. Further investigation should use antibody staining or the nGreen Hydra line which expresses GFP specifically in the neurons to track changes in network morphology (Rob Steele). The next step in this study could be to ask: How does the number of neurons present near the cut surface of the peduncular half change? Are there regions of asynchronicity during regeneration as seen in regenerating dissociated animals (Lovas and Yuste, 2021)? And how does gene expression change near the cut surface during regeneration?

Lastly, there is significantly more data that could be extracted from the existing movies that are available. An immediate analysis that could be done is looking at how the interval between RP's changes with bisection. The number of RP events is directly dependent on the length of an elongation event. However it is possible that there is a

difference in the interval between the RP's changes. Figure 2, for example, shows a rapid increase in frequency of RPs from the intact animal to the bisected peduncle.

Figures

Figure 1. Imaging Pipeline

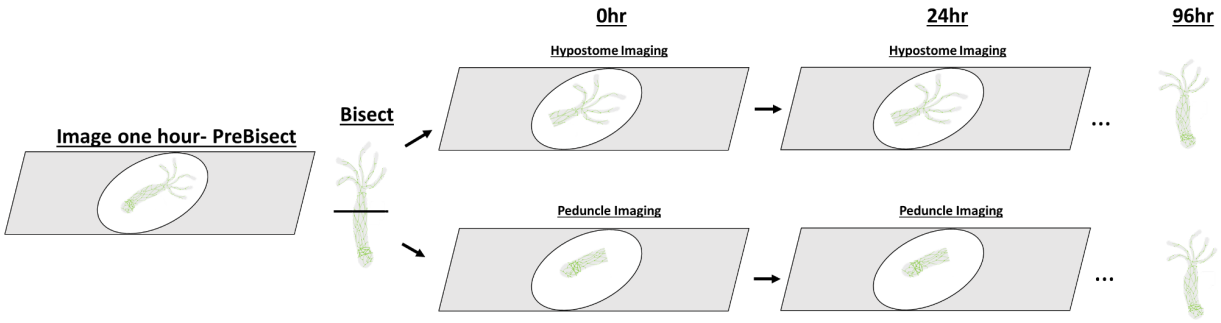

Figure 1. Imaging Pipeline

Hydra is imaged for 1 hour prior to bisection. After bisection, the peduncle and hypostome are imaged independently for 30mins – 1 hour every 24hours up to 96 hours during regeneration.

Figure 2. Integrated fluorescence and behavior

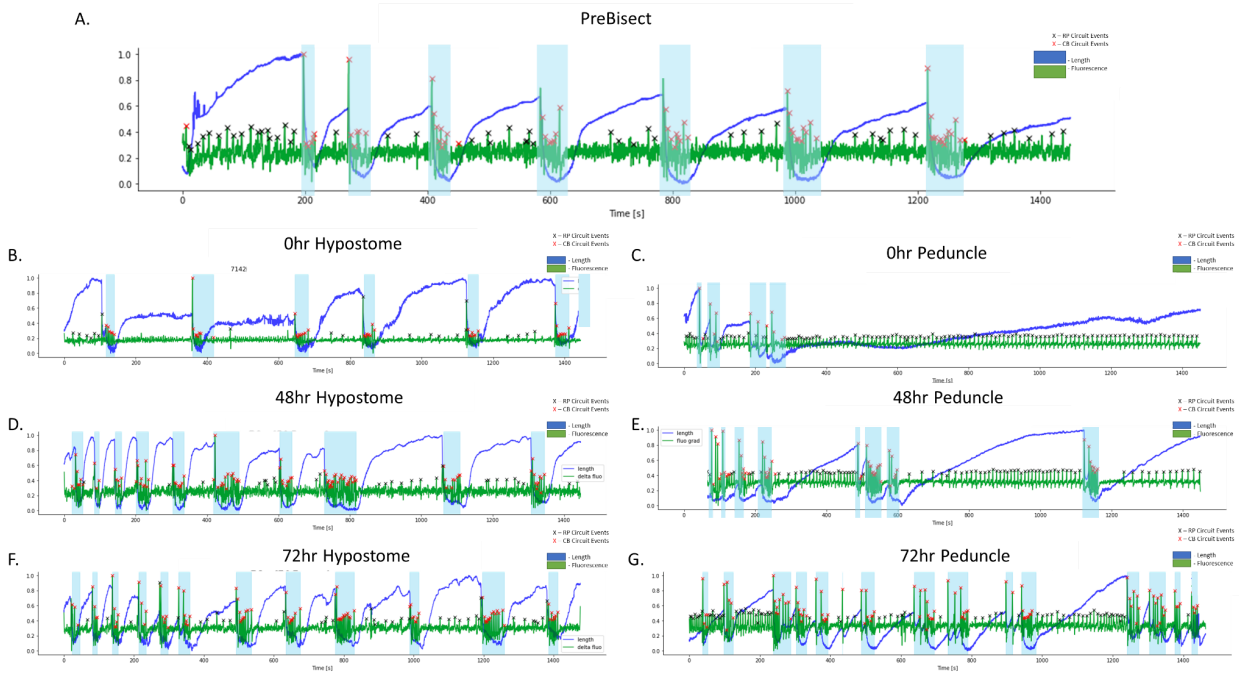

Figure 2. Integrated fluorescence and behavior during regeneration

A. Prebisect baseline data. Fluorescent intensity and length of the animal were calculated and plotted over time (frames). Black X's indicate RP events which have smaller, more frequent, peaks than CB events indicated by red X's. B)-C) Fluorescent intensity and animal length calculated immediately after bisection for peduncle and hypostome respectively. D)-E) 48hours recovery Fluorescent intensity and length of the animal were calculated and plotted over time (frames). Notable behavior and circuit activity are present in the 48 hour peduncle.

Figure 3. CB circuit activity in regenerating hydra

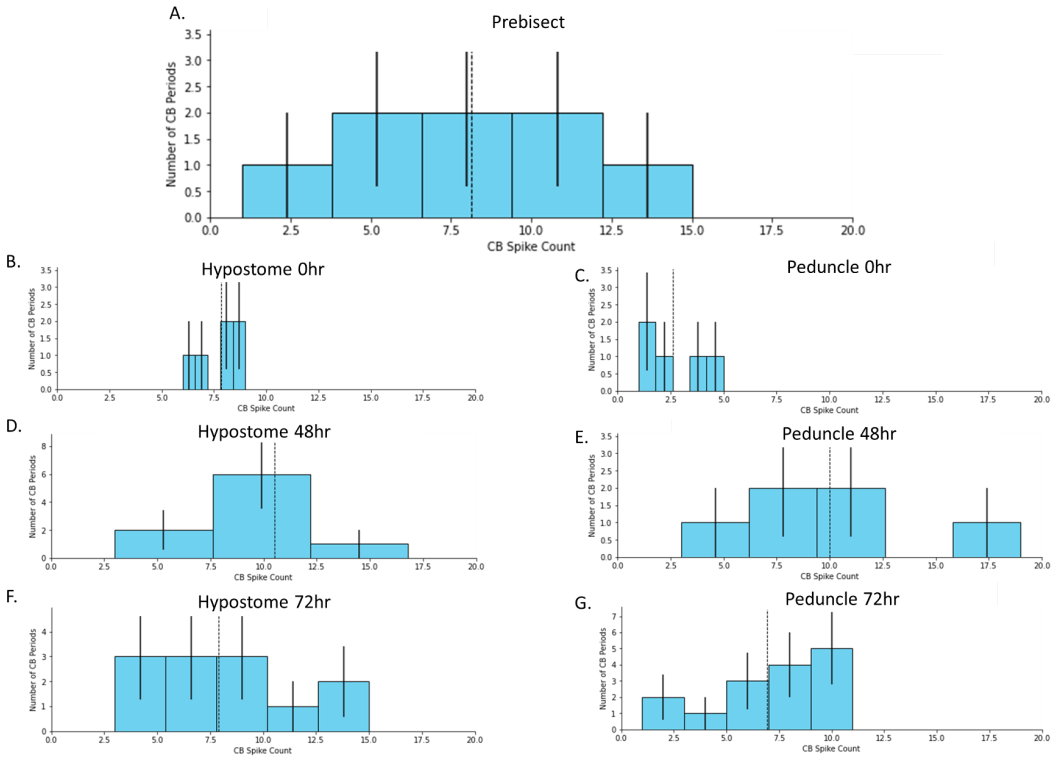

Figure 3. Circuit activity in regenerating hydra halves

A) Baseline CB activity prior to bisection. Dashed line is the average number of events per behavioral event. B)-C) CB activity in the hypostome and peduncle after bisection at the 0-hour checkpoint. Dashed line is the average number of events per behavioral event. D)-E) CB activity in the hypostome and peduncle 48hours after bisection. Dashed line is the average number of events per behavioral event. F)-G) CB activity in the hypostome and peduncle 72 hours after bisection. Dashed line is the average number of events per behavioral event.

Figure 4. RP circuit activity in regenerating hydra

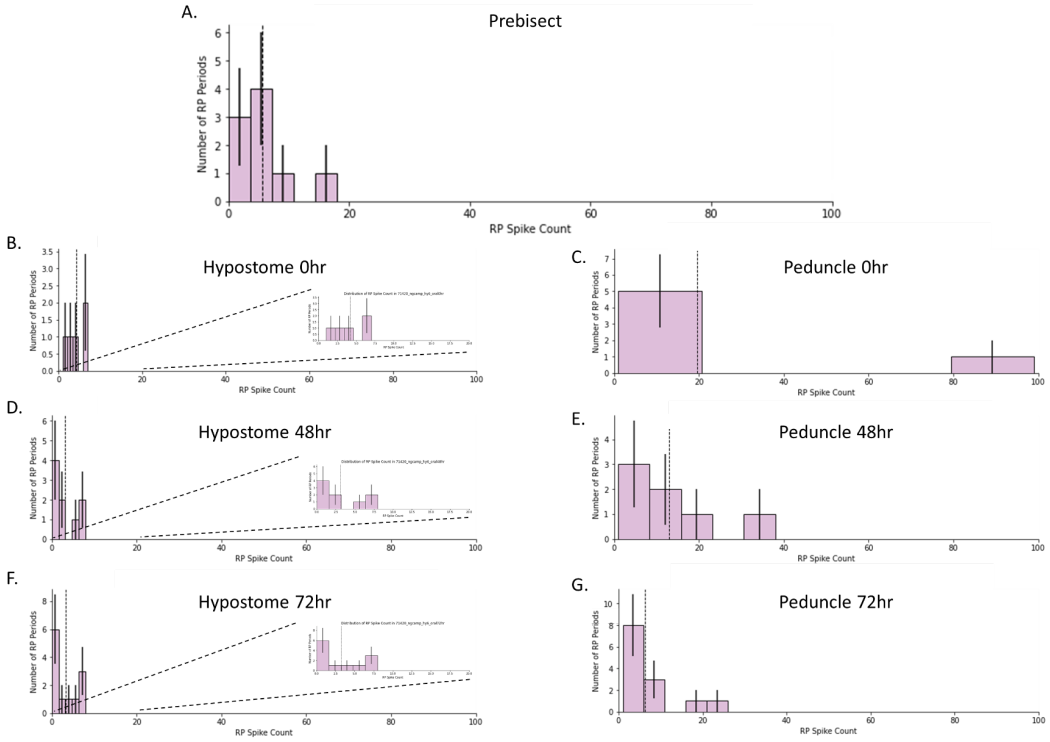

Figure 4. RP circuit activity in regenerating hydra.

A) Baseline RP activity prior to bisection. Dashed line is the average number of events per behavioral event. B)-C) RP activity in the hypostome and peduncle at the 0-hour checkpoint. Inset graphs are magnifications of the x-axis D)-E) RP activity in the hypostome 48 hours after bisection. Inset graphs are magnifications of the x-axis F)-G) RP activity in the peduncle 72 hours after bisection. Inset graphs are magnifications of the x-axis

Figure 5. Contraction Frequencies in Bisected Hydra

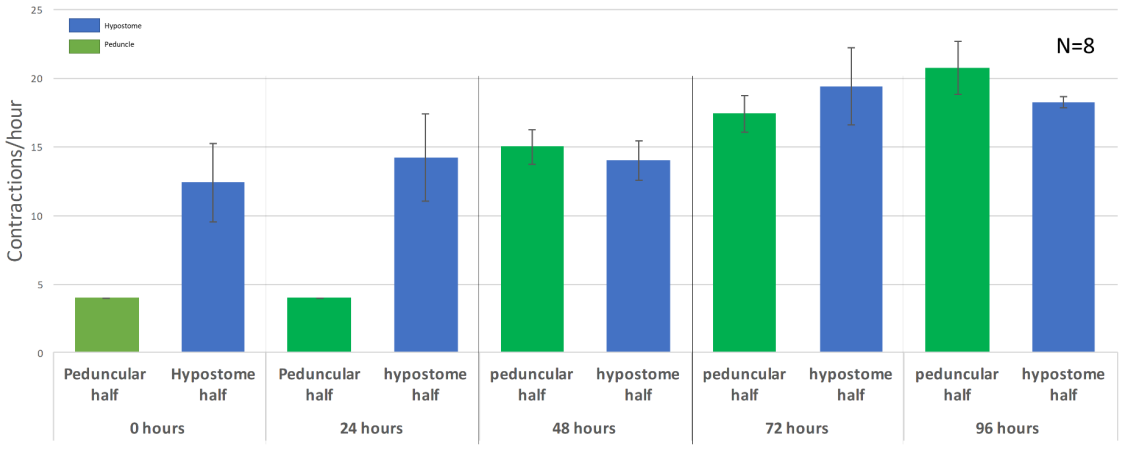

Figure 5. Contraction frequencies in Bisected Hydra

Green is peduncle half of hydra. Blue is hypostomal half. The first 24 hours of regeneration show that contraction frequencies are reduced in the peduncular half but recovers by 48 hours

References

Carter JA, Hyland C, Steele RE, Collins E-MS. 2016. Dynamics of Mouth Opening in Hydra. *Biophys J* **110**:1191–1201. doi:10.1016/j.bpj.2016.01.008

de Chaumont F, Dallongeville S, Chenouard N, Hervé N, Pop S, Provoost T, Meas-Yedid V, Pankajakshan P, Lecomte T, Le Montagner Y, Lagache T, Dufour A, Olivo-Marin J-C. 2012. Icy: an open bioimage informatics platform for extended reproducible research. *Nat Methods* 9:690–696. doi:10.1038/nmeth.2075

Dupre C, Yuste R. 2017. Non-overlapping Neural Networks in Hydra vulgaris. *Curr Biol* **27**:1085–1097. doi:10.1016/j.cub.2017.02.049

Han S, Taralova E, Dupre C, Yuste R. 2018. Comprehensive machine learning analysis of Hydra behavior reveals a stable basal behavioral repertoire. *eLife* **7**:e32605. doi:10.7554/eLife.32605

Heimfeld S, Bode HR. 1985. Growth regulation of the interstitial cell population in hydra: I. Evidence for global control by nerve cells in the head. *Dev Biol* **110**:297–307. doi:10.1016/0012-1606(85)90089-2

Kass-Simon G, Passano LM. 1978. A neuropharmacological analysis of the pacemakers and conducting tissues ofHydra attenuata. *J Comp Physiol* **128**:71–79. doi:10.1007/BF00668375

Lovas JR, Yuste R. 2021. Ensemble synchronization in the reassembly of Hydra's nervous system. *Curr Biol* **31**:3784-3796.e3. doi:10.1016/j.cub.2021.06.047

Mathis A, Mamidanna P, Cury KM, Abe T, Murthy VN, Mathis MW, Bethge M. 2018. DeepLabCut: markerless pose estimation of user-defined body parts with deep learning. *Nat Neurosci* **21**:1281–1289. doi:10.1038/s41593-018-0209-y

Passano LM, Mccullough CB. 1963. Pacemaker Hierarchies Controlling the Behaviour of Hydras. *Nature* **199**:1174–1175. doi:10.1038/1991174a0

Schneider CA, Rasband WS, Eliceiri KW. 2012. NIH Image to ImageJ: 25 years of image analysis. *Nat Methods* **9**:671–675. doi:10.1038/nmeth.2089

Shimizu H, Koizumi O, Fujisawa T. 2004. Three digestive movements in Hydra regulated by the diffuse nerve net in the body column. *J Comp Physiol A* **190**. doi:10.1007/s00359-004-0518-3

Siebert S, Farrell JA, Cazet JF, Abeykoon Y, Primack AS, Schnitzler CE, Juliano CE. 2019. Stem cell differentiation trajectories in *Hydra* resolved at single-cell resolution. *Science* **365**:eaav9314. doi:10.1126/science.aav9314

Takaku Y, Hwang JS, Wolf A, Böttger A, Shimizu H, David CN, Gojobori T. 2014. Innexin gap junctions in nerve cells coordinate spontaneous contractile behavior in Hydra polyps. *Sci Rep* **4**:3573. doi:10.1038/srep03573

Vogg MC, Galliot B, Tsiairis CD. 2019. Model systems for regeneration: *Hydra*. *Development* **146**:dev177212. doi:10.1242/dev.177212

Conclusions and Future Directions

Summary of Findings

In this project I explored a number of different aspects of the hydra nervous system including, regeneration, circuits/behavior relationship, connectivity via gap junctions, and innexin phylogenetics. By expressing hydra innexins in mouse N2a cells I was able to determine that these predicted genes were capable of making functional gap junction proteins. Analysis of dual whole cell voltage clamp current recordings determined that hydra innexin gap junctions are voltage dependent and undergo inactivation. Single channel recordings reflected inactivation as greater voltage steps reduced conductance. Phylogenetics and membrane topology revealed that hydra innexins resemble those expressed within other hydrozoans. Along with many cnidarians, hydrozoan innexins have a wide variety of possible phosphorylation and N-glycosylation sites that may regulate innexin channel docking and conductance(Welzel and Schuster, 2022). I also identified through sequence alignment that there are two additional cysteine residues located on the first extracellular loop of hydrozoan innexins. Bisection and regeneration of hydra peduncular and hypostomal halves revealed the presence of CB pacemakers near the hypostome. These pacemakers may be regulated by the peduncle or a sort of feedback loop is present which regulates contraction and elongations within the CB circuit. Lastly, in collaboration with Hengji Wang in the Fairhall lab, I provided calcium imaging videos of the ectoderm, endoderm, and nerve net, along with analysis so that Hengji could better model the biomechanics of hydra behaviors.

Future Directions

In this dissertation I present a characterization of hydra innexins with electrophysiological and molecular data independent of one another. The results provide future researchers a stepping stone to identify the relationship between molecular topology and electrophysiology. Confirmation of predicted phosphorylation sites on hydra innexins could be done by induced phosphorylation or removal via mutation along with dual whole cell voltage clamp. N-glycosylation has been shown to prevent docking with pannexin channels, but within the mammalian N2a system hydra innexins are still able to form gap junctions. It may be necessary to establish a new cellular model which would allow for proper glycosylation and other post translational modifications to occur on hydra innexins to better characterize their biophysical properties. Furthermore, the biophysical properties of hydra innexins presented in this thesis also provide computational biologists with parameters to begin building a model of the hydra nerve net which appears to have extensive gap junctional coupling.

Bisection and regeneration of hydra circuits remains an intriguing phenomenon in hydra. It is clear that CB pacemakers are localized in the hypostome of hydra but many questions remain such as: How many pacemakers are there? How are they organized? And how are they synchronized? This thesis presents a foundation to facilitate answering these questions. The presence of nerve rings found in both the hypostome and peduncle may play a significant role in CB and RP regulation (Hufnagel and Kass-Simon, 2016). Future experiments involving specific cell ablation techniques may help elucidate these questions. Precisely removing neurons within the hypostomal ring and the peduncular ring would address the role each plays. By sequentially removing neurons from the hypostomal ring it

could be identified how many neurons are required in the pacemaker system. These questions should be answered to build a better model for the hydra nervous system.

References

Hufnagel LA, Kass-Simon G. 2016. The two nerve rings of the hypostomal nervous system of Hydra vulgaris—an immunohistochemical analysis. *Cell and Tissue Research* **366**:255–269. doi:10.1007/s00441-016-2447-1

Welzel G, Schuster S. 2022. Connexins evolved after early chordates lost innexin diversity. *eLife* **11**:e74422. doi:10.7554/eLife.74422